# BISTATIC/MONOSTATIC SYNTHETIC APERTURE RADAR FOR ICE SHEET MEASUREMENTS

BY


## JOHN PADEN

## B. SC. COMPUTER ENGINEERING

## THE UNIVERSITY OF KANSAS, 1999


Submitted to the Department of Electrical Engineering and Computer Science and the Faculty of the Graduate School of the University of Kansas in partial fulfillment of the requirements for the degree of Master of Science.

Thesis Committee:

_____
Chairperson

_____

_____

Date of Defense: April 18, 2003

# ABSTRACT

A ground-based monostatic/bistatic, broadband VHF synthetic aperture radar is being developed for the two-dimensional mapping of the basal conditions of polar ice sheets. The goal is to obtain knowledge of the morphology or 'roughness' of the bed, the distribution of the subglacial water film, and the amount of rock debris and silt in the basal ice. Since ice sheet basal conditions represent one of the boundary conditions of glacier flow, they are a fundamental component in ice flow models. The ability to establish basal conditions with a high degree of accuracy will fill an important gap in the knowledge base used to predict the origin and migration of ice streams, which drain the majority of the polar ice sheets. An improved understanding of ice sheet dynamics can be used to predict future sea level rise that threatens coastal regions throughout the world.

A measurement model for the radar system is described. SAR processing algorithms based on this measurement model using a matched filter and maximum likelihood filter are then derived. The model and algorithms are used throughout the thesis to simulate various scenarios needed to identify certain constraints. The model and algorithms are also tested in the sandbox laboratory to assess their utility.

Two methods are considered to accelerate the time taken to map a region. The first method found a sensor geometry that minimized measurement time as a function of frequency, backscatter characteristics, and ice thickness. The optimal position was very sensitive to the backscatter characteristics, but in general the transmitter may be placed further out than the optimal position without a significant increase in measurement time. This means that, while different basal characteristics may have different optimal sensor geometries, a compromise can be made between these geometries. Another method for improving traverse time uses an along-track array towed behind the transmitter vehicle. The maximum length of the array versus required bedrock resolution was found and several ideas for circumventing this maximum length limitation are proposed.

A number of errors involved in SAR processing were analyzed using simulations. The matched filter is a fairly scalable algorithm, but it does not consider interference and its inability to estimate the reflectivity of a target that is adjacent to other targets is demonstrated along with a comparison to the maximum likelihood filter that does consider interference. The sensitivity of these filters to position errors is simulated. It was found that one tenth of a wavelength accuracy is needed to effectively SAR process targets. The sensitivity of the SAR processor to dielectric errors is illustrated. It was found that the image stayed focused even with fairly significant dielectric errors, but the target positioning accuracy was directly affected (as was expected). The effectiveness of the SAR processing algorithm for focusing smooth bedrock surfaces is considered as well.

The sandbox laboratory was used to test a scaled model of the system. Several calibration measurements were taken to supply the system model with the parameters necessary to predict the response from targets buried in the sand. The SAR processor was able to accurately resolve each of the targets imaged to within a few centimeters. The results also showed that the reflectivities for identical targets were the same to within a 4 dB spread.

# TABLE OF CONTENTS

# LIST OF FIGURES

# LIST OF TABLES

# CHAPTER 1: INTRODUCTION

## 1.1 SCIENCE MOTIVATION

The mean sea level, which appears to have been steady for the last 3-4000 years, has been rising between 1 to 2.6 mm per year over the past century with 2 mm per year being the most accepted value [1, 2, 3]. This rise in sea level has had a number of costs: abandoned islands, lost coastline and agricultural land, costly replacement of sand to eroded beachfronts, loss of marshland habitats, increased vulnerability to severe storms, and threatened aquifers [1, 4]. Since nearly 100 million people live within 1 meter of the current mean sea level [1, 2] and 37% of the world's population lives in coastal regions [1] (defined as being within 100 km of the coast), understanding possible contributions to sea level rise is of considerable practical importance. The rise in sea level has also been coupled with an ever-increasing population in the coastal regions. If these trends continue, the social and economic consequences will be severe, especially to developing countries with little resources [1].

While the precise causes of the rise in sea level are still in debate, there are three causes that seem most likely. The first is the thermal expansion of the ocean due to the concurrent rise in the mean global temperature of 0.6° C over the last century. The second is the melting of mid-latitude temperate glaciers. The third, and most controversial because of the lack of a complete set of data, is the melting of the Antarctica and Greenland ice sheets [2]. To determine the contribution of melted ice to sea level rise, the mass balance of the ice sheet must be measured. The mass balance is the flux in ice mass. In other words, when the mass balance is positive, the net mass of the ice sheet is increasing and when the mass balance is negative, ice is being lost. If the mass balance of the ice sheet is known, its contribution to global sea level can be determined. Several methods for determining mass balance and a compilation of mass balance measurements for the polar ice sheets are given in [5].

Despite these data, the combined uncertainty in the mass balance of the Greenland and Antarctic ice sheets is larger than all other causes [2][1]. Regardless of whether or not the mean sea level has been affected significantly in the last century by melting ice sheets, it is certain that global climate changes could induce such behavior (e.g. mean sea level has risen as much as 120 meters since the last glacial maximum 21,000 years ago) [1, 2, 5, 6].

The Greenland and Antarctic ice sheets act as large reservoirs of water, holding nearly 80% of the fresh water in the world [7, 8, 1]. This water mass is equivalent to 2% of the ocean water mass [9,1] and complete melting of the polar ice sheets would raise the global sea level by 70 meters [7, 8, 10]. A small decrease in the volume of the ice sheets (1.5%) would increase the global sea level by 1 meter. Since the polar ice sheets have the capacity to release this water under certain climatic conditions, an understanding of the process is worth pursuing. Aside from sea level issues and scientific curiosity, understanding the dynamics of ice sheets helps provide a general understanding of how the cryosphere affects and is effected by the climate of the earth system [7, 10].

Our goal is to provide data to the scientific community that will improve the understanding of ice sheet dynamics and the ability to create ice sheet models. Models are important because even with a complete dataset of the current mass balance, the time over which measurements are taken is small compared to the time constants of the ice sheet dynamics. The models provide the ability to decipher between short and long-term trends and identify feedback mechanisms. The models can thereby *predict future mass balance changes*.

There are several primary forcing functions that act upon the ice sheets. These are accumulation and ablation from the glacial surface, gravity acting on the ice sheet that depends on the amount of ice and its general structure, and finally basal

[1] The Ice Cloud and land Elevation Satellite (ICESat) was launched in early January 2003. The Geoscience Laser Altimetry System (GLAS) onboard the satellite will provide the ability to map the entire Greenland ice sheet and most of the Antarctica ice sheet to a precision of 10 cm (from the University of Texas Center for Space Research website). The European Cryosat (2004 anticipated launch) radar altimeter will extend the mapping range beyond GLAS in Antarctica to 88° S.

conditions at the glacial sole [10]. Significant effort has been put into the remote sensing of accumulation rates, surface topography and velocities, ice thicknesses and internal layering. While more complete data sets need to be taken, the ability to collect these parameters via remote sensing has been confirmed [11, 12, 13, 14, 15]. On the other hand, there exists no radio-glaciological technology that is able to unambiguously determine whether the bed is wet or frozen. The primary goal of this radar system is to measure the basal conditions, including roughness and distribution of liquid water.

Ice sheets exhibit laminar (or lamellar) flow properties when enough stress is applied. Essentially, when enough ice mass is accumulated in one area, the force of gravity acting on the ice tends to deform or flatten it. This plastic deformation tends to be slow (Byrd glacier in Antarctica is thought to be an exception) [10] and the majority of the ice sheets move under this flow regime. On the other hand, ice streams, as defined by Van der Veen in [10], are fast moving glaciers that are thought to move primarily through sliding rather than deformation. In this case, the glacial sole is lubricated with water, which effectively lowers the basal resistance (friction) to the point that the ice can slide across the bottom. The average basal resistance acts with lateral drag and gradients in longitudinal stress to counteract the driving stress of gravity. Ice stream flow is distinguished from lamellar flow by the varying apportionments between these terms. Because basal stress is not allowed to build up in an ice stream, this largely precludes flow by deformation, which is assumed to have zero-velocity at the base [3].

This work is specifically aimed at determining the origin and migration of ice streams. Since the ice streams drain the majority of the inland ice sheets, their understanding is crucial to understanding past mass balance changes and thereby predicting future mass balance changes. Through satellite SAR images of the glacial surface it was found that ice streams reach hundreds of kilometers into the inland ice sheets and are laterally bounded by slow moving ice [16]. As mentioned above, the primary difference between the two flow regimes relies on an understanding of the basal conditions. Knowledge of the morphology or 'roughness' of the bed, the

thickness of the subglacial water film, and the amount of rock debris and silt in the basal ice are needed to determine the average basal resistance [10]. The science models require wide-area coverage and the ability to resolve these physical characteristics to within 100 m [17]. Also, the primary regions of interest have an ice thickness between 1000 and 5000 m.

There are several methods that can be used to observe the basal conditions of an ice sheet. A brute-force method involves drilling a borehole to the bottom of the ice sheet and passing measurement equipment down into the borehole. Many boreholes to the base of the ice sheet have been drilled [18], but wide area coverage with 100 m resolution is infeasible because the resources and time consumed for each borehole are tremendous. Radar, on the other hand, provides the ability to remotely sense the basal conditions over a large area in a comparatively short period. The physical features can be distinguished from one another by the use of a wideband radar. The radar also does not require modifying the environment that is being measured. The boreholes are still necessary for radar, however, because of the need for calibration and testing. Finally, to measure a wide area, the radar should measure a swath of bedrock for each pass rather than a single point on the bedrock as shown in Figure 1-1.

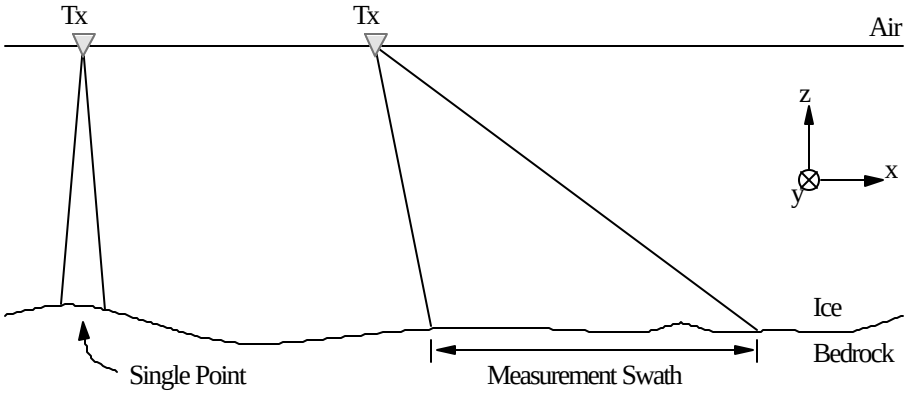


*Figure 1-1: By measuring a swath rather than a single point, more bedrock can be mapped in the same amount of time.*

## 1.2 BACKGROUND

Scattering of the radar signal off the bedrock depends on the nature of the surface. When an electromagnetic wave, launched by a transmitter, strikes a rough surface, energy will be scattered in all directions as shown in Figure 1-2. The measure of energy scattered back toward the transmitter is called the backscatter (since it is going "back" toward the source of the wave). The energy scattered away from the transmitter is called forward-scatter. For most surfaces the forward-scatter is significantly stronger than the backscatter.

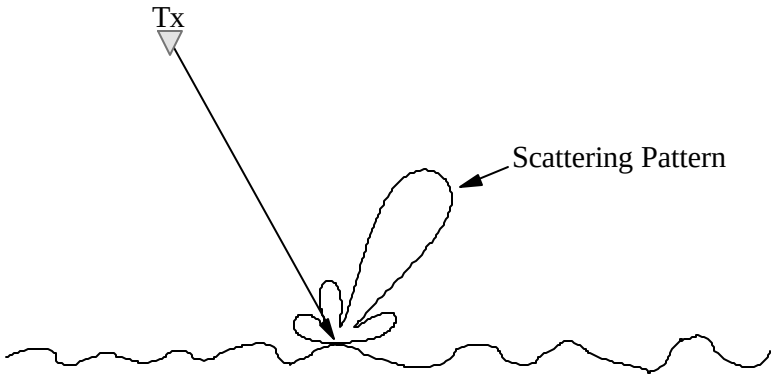


*Figure 1-2: Example of scattering from a rough surface.*

As one might expect, the rougher a surface is the more backscatter energy there will be. Figure 1-3 shows the scattering from a perfectly rough surface. In this case, the incident energy is scattered equally in all directions. This type of scattering is called diffuse scattering. With diffuse scattering, the placement of the receiver is not restrained by the scattering since the energy will be scattered in all directions.

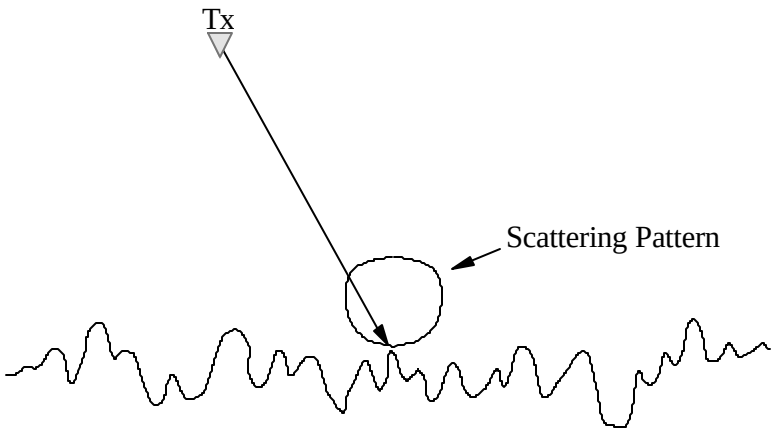


*Figure 1-3: Example of scattering from a perfectly rough surface.*

The other extreme is a perfectly flat or *specular* surface. In this case there would be no backscatter energy. Figure 1-4 shows the scattering from a specular surface. This type of scattered energy is generally referred to as reflected energy rather than scattered energy since it obeys certain properties. All of the scattered energy is forward-scatter energy.

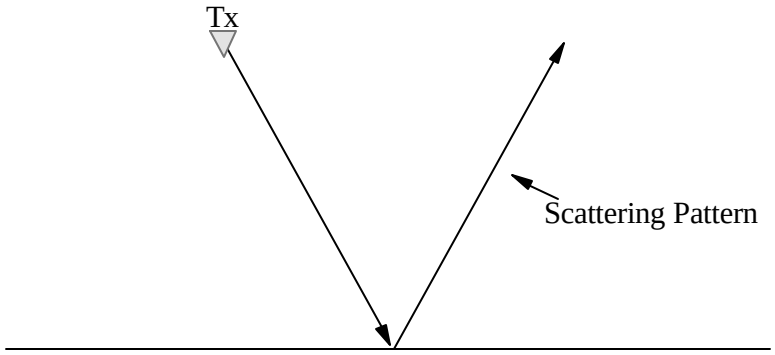


*Figure 1-4: Example of scattering from a perfectly flat surface.*

A specular surface is analogous to a mirror in optics. When an optical wave is launched at a mirror (e.g. flashlight), all of the energy is reflected forward. If an observer stands where the flashlight is and looks at the mirror, they will not see any energy unless the flashlight is pointed normal to the surface of the mirror (see Figure 1-5 for illustration). This illustration implies that the placement of the receiver is *very* important. If the receiver is placed outside of the forward scatter wave, then no energy can be captured and used to determine the nature of the surface.

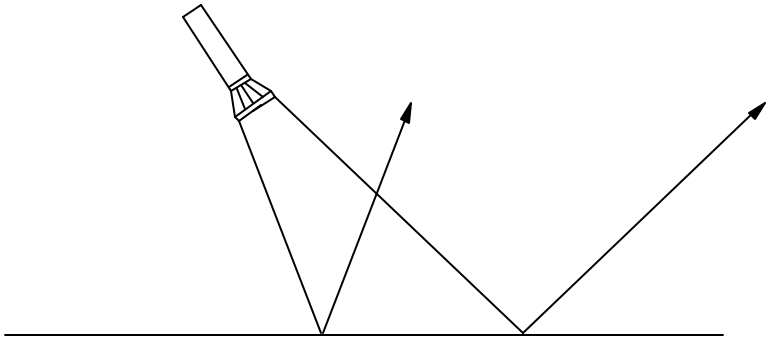

*Figure 1-5: Example of a flashlight reflection off of a mirror.*

The bedrock of the ice is a mixture of these two extremes, having both diffuse and specular scattering (see Figure 1-2 for an example). Based on previous radar depth sounder measurements the backscatter from bedrock was modeled using geometric optics [19]. The geometric optics model has strong forward scattering with weak diffuse scattering. Because of this the forward scatter tends to be significantly larger than the backscatter since the surface is fairly smooth or *quasi-specular*. In this case, the placement of the receiver is restricted. We are not as free to place the receiver where we choose as with a perfectly rough surface, but neither are we as constained as in the specular case.

The geometric optics model gives us a method for determining the amount of energy scattered in a particular direction. If the transmitter and receiver are collocated (monostatic), the direction of the expected scattering energy is usually measured in reference to a backscatter angle. The backscatter angle, $r$, is measured with respect to the surface normal as shown on the left side of Figure 1-6. If the transmitter and receiver are separated (bistatic), for the purposes of this thesis, the direction of the expected scattered energy will be measured from the specular ray and this angle will be called the forward-scatter angle, $b$. A comparison of the forward-scatter angle and the backscatter angle is given in Figure 1-6.

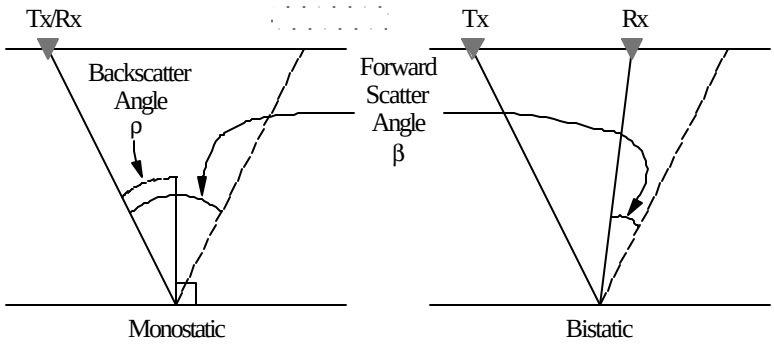


*Figure 1-6: The backscatter angle for the monostatic case is given in the left-hand image. The forward-scatter angle for both cases is shown for a comparison to the backscatter angle. The rays from the transmitter to the target and from the target to the receiver are solid. The specular ray is dashed.*

## 1.3 PRINCIPLES OF OPERATION

The history of glacial radar echo sounding (RES) is documented in Gogineni et al. [20]. Nearly all radar echo sounders to date, whether ground-based or air-borne, have produced one-dimensional profiles of the bedrock. Whenever a two-dimensional map was needed, a grid constructed of many one-dimensional profiles was created (e.g [21, 22]). One exception to this rule was the use of monostatic side-looking radar to image the Bach Ice Shelf in the Antarctic Peninsula [23]. The problem with relying solely on the monostatic approach is that the bedrock tends to exhibit quasi-specular characteristics because of its smooth surface [19, 24]. The scattering, at typical depth sounder frequencies, follows a geometric optics model and consists of a strong specular reflection and a weak diffuse scattering [25]. This means that the bedrock acts like an imperfect mirror and a monostatic radar can only see the spot directly underneath it and a little bit to each side (the measurable swath shrinks to a small point on the bedrock).

Since the measurable swath shrinks to a small point on the bedrock directly beneath the radar, side-looking monostatic radar will not work due to weak backscattering (refer to flash-light analogy illustrated in Figure 1-5). The desire for operating in side-looking mode is that a large swath can be measured rather than a

single point. To circumvent the weak backscattering, the radar system will provide monostatic *and bistatic* modes of operation. The monostatic mode can be used when there is sufficient backscatter energy from the targets of interest. If there is insufficient backscatter energy, then the radar will switch to bistatic mode so that the receiver can be placed in the strong forward-scatter region. Figure 1-7 and Figure 1-8 below depict these two situations. In these two figures the along-track direction is normal to the profile shown and the cross-track direction is aligned with the x-axis.

The resolution of the radar refers to the ability to resolve the reflectivity at one point on the bedrock from another point on the bedrock. In both monostatic and bistatic modes, the along-track or y-dimension resolution will be improved using traditional SAR techniques. The technique for improving cross-track or x-dimension resolution differs for the two operating modes. In monostatic mode, range resolution will be used to determine cross-track resolution as shown in Figure 1-7 – each position on the bedrock is at a different range from the Tx/Rx pair. Because range resolution operates in the time domain, all samples can be taken from one spatial position.

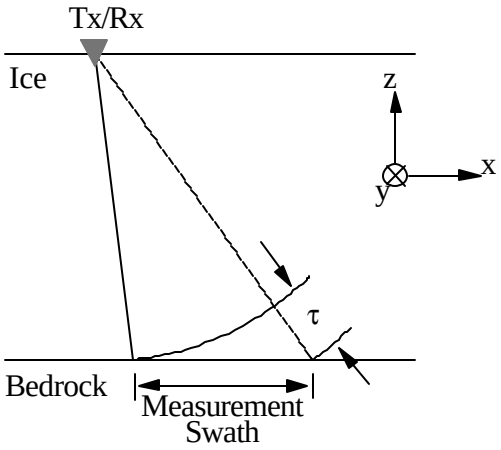


*Figure 1-7: Monostatic radar. Each ray has a different length or range.*

In bistatic mode, we will be operating at the specular point to increase the received signal power. This has a disadvantage in that the range resolution disappears at the specular point as shown in Figure 1-8. The range is the sum of the distance

from the transmitter to the target and from the target to the receiver. Every position on an ellipse, which has its foci at the transmitter and receiver positions, is at equal range. Since the ellipse drawn in Figure 1-8 almost coincides perfectly with the bedrock surface, most if not all targets in the cross-track direction will fall into the same range bin. Therefore, another method besides range resolution must be used to resolve targets in the cross-track direction.

We have chosen to use digital beam-forming by spatially sampling with the receiver in the cross-track direction. This is similar to SAR in the sense that we will be synthesizing a larger aperture with a smaller physical aperture and the processing involved is identical in many respects to the along-track processing. Figure 1-9 shows how the receiver will take multiple samples in the cross-track direction. After the receiver completes its movements in the cross-track direction, the receiver and transmitter move forward together in the along-track direction and repeat the process.

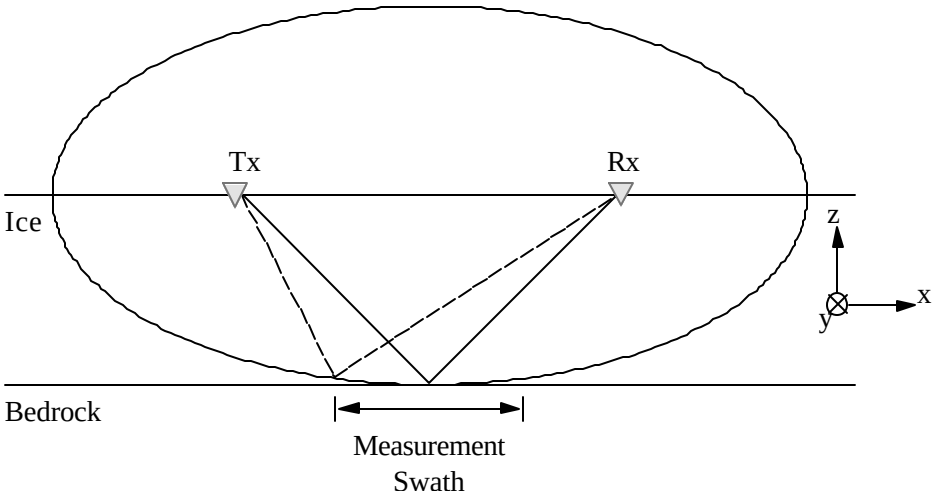


*Figure 1-8: Bistatic radar and equal-range ellipse. Both rays from the transmitter to the receiver are the same length.*

Since the bistatic mode of operation requires spatial sampling to achieve cross-track resolution rather than just time sampling, it takes much longer to cover the same amount of terrain. Therefore monostatic mode is the preferred mode of operation, however the bedrock must be rough enough to provide detectable backscatter at off-nadir angles.

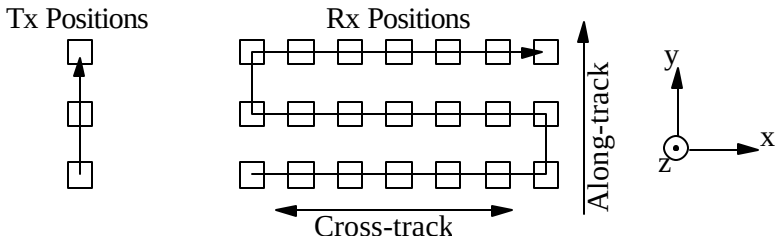


*Figure 1-9: Transmitter and receiver movements in bistatic mode.*

The direct output of either system is a two-dimensional reflectivity map of the bed. Once the two-dimensional reflectivity map has been produced, the geophysical and electromagnetic (EM) models will help provide interpretations of the radar measurements. There are several parameters that affect the reflectivity. These are spatial contrast in the medium's dielectric, local slope, and, finally, surface roughness.

Because of this, the radar will operate at three different frequencies to facilitate the differentiation of various geophysical phenomena. This will provide three independent measurements of the reflectivity so that frequency sensitive parameters (such as roughness) can be isolated. With only one frequency, the system would be underdetermined and we would not be able to unambiguously classify basal conditions.

The models will help provide an understanding of the interaction between frequency and reflectivity. This knowledge of the interaction will be used to translate the radar measurements into basal conditions (e.g. roughness and distribution of liquid water). The basal conditions can then be used in ice flow models and to verify theoretical models that attempt to predict basal conditions.

Figure 1-10 summarizes the key systems in the radar and data processing and Table 1-1 summarizes the parameters of the radar system. The system-model includes both the propagation model for the ice sheet as well as the radar system. This thesis will address the sensor geometry, some aspects of the system-model, and the SAR processing of radar data.

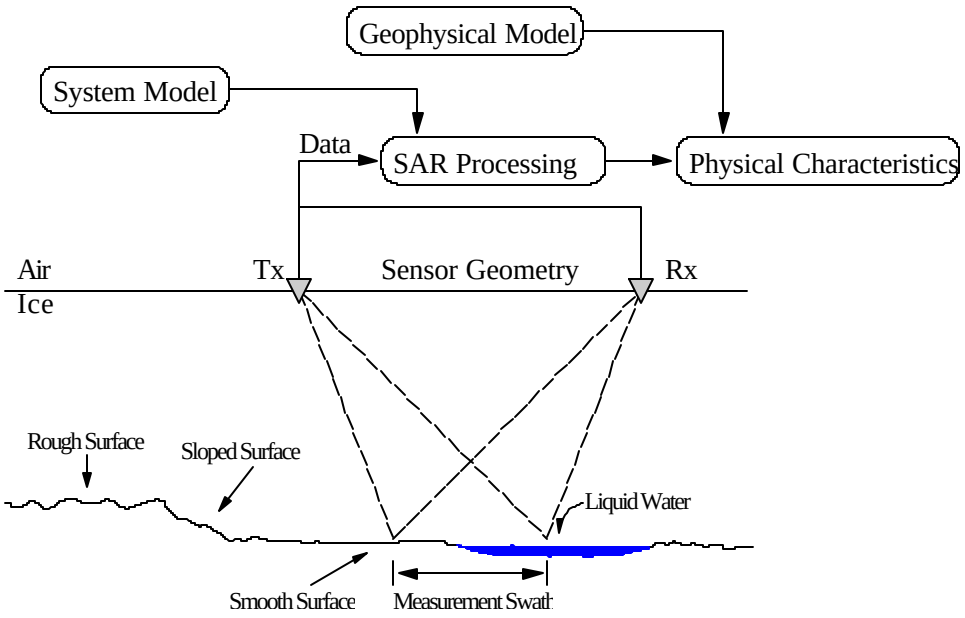


*Figure 1-10: High-level overview of SAR system.*

*Table 1-1: SAR System Parameters*

| Parameter | Value |
|---|---|
| Bedrock Resolution | 100 m |
| Measurement Swath | 1000 m |
| Ice Thickness | 1000-5000 m |
| Center Frequencies | 60, 150, and 350 MHz |
| Height of Antennas Relative to Ice Surface | 0 m |

## 1.4 OVERVIEW

Chapter one discusses an overview of the thesis including the motivation and the principles of operation for the SAR.

An overview of SAR processing and its application for this radar system is given in chapter two. The overview starts with an explanation of the data collection geometry. The measurement model used in this thesis is described next. The various parameters in the model are derived in the following sections. These parameters determine the filter coefficients of the SAR processor for which a matched filter and maximum likelihood filter are derived. The choice of which domain (time/frequency

and space/wavenumber) is considered. The F-k migration algorithm is discussed and its limitations to bistatic processing are shown.

As mentioned above, bistatic mode will take much longer than monostatic mode to cover the same area. Consequently two methods for expediting bistatic measurements are covered in chapter three. The first method, shows how to find the optimal bistatic sensor geometry that minimizes the required length of the cross-track transect. The second method shows how an along-track antenna array can accelerate the bistatic SAR measurements. Constraints are set on how large the antenna array can be while still achieving the desired SAR resolution.

In chapter four, the matched filter's sensitivity to position errors, dielectric errors, and specular surfaces is modeled and limits on the maximum tolerable position errors are proposed.

Finally, in chapter five, results from measurements taken in the sandbox test facility are given. Simulated data is compared with the measurements to test the validity of the system model. The SAR processing algorithm from chapter two is then used to process both the simulated and measured data sets. The results are compared and discussed.

# CHAPTER 2: SAR PROCESSING

## 2.1 INTRODUCTION

The output of the SAR processor is a two-dimensional reflectivity map of the bedrock. To achieve the desired bedrock resolution, our system needs antennas that are very large (e.g. 50 to 200 meters on each side). To build and use such an antenna would be extremely costly and unnecessary. Instead, if the scene of interest is not time varying[2], a large synthetic aperture composed of many measurements with a small antenna can be used. The essential tradeoff is in the time that it takes to collect the data; we have to collect hundreds of individual measurements, one at a time, rather than all the measurements at once.

As mentioned in chapter one, the radar will be capable of operating in monostatic and bistatic modes. The transmitter and receivers will be placed on land vehicles as shown in Figure 2-1. The transmitter (vehicle one) will be used for both monostatic and bistatic modes. The receiver on vehicle one will be used for monostatic operation and the receiver on vehicle two will be used for bistatic operation. Land operation was chosen for the SAR because coordinating bistatic measurements from air borne vehicles and taking the necessary grid of measurements would be much more difficult. Also, by placing the antenna next to the ice surface, energy can be transmitted into the ice at launch angles greater than the critical angle.

[2] The scene can be changing, but the effects of the changes must then be compensated for or the changes must be slow relative to the time over which the measurements are taken.

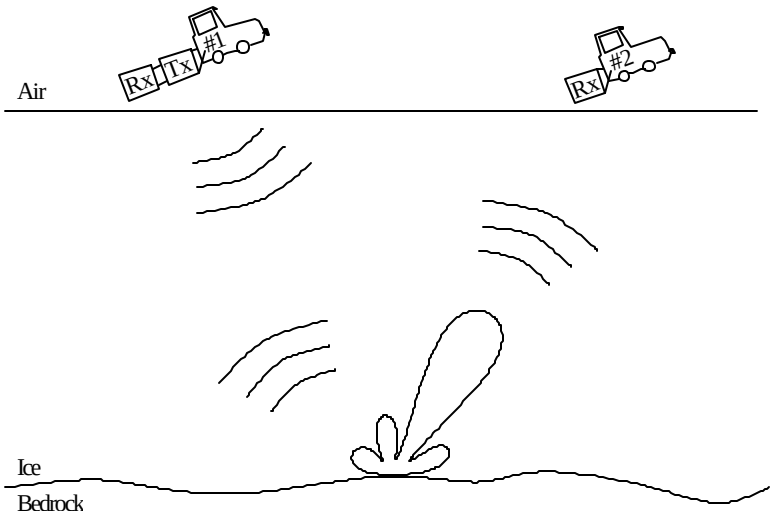


*Figure 2-1: Illustration of ground vehicles with SAR.*

Figure 2-2 shows the monostatic configuration. In this mode, the first vehicle is taking all of the measurements and the second vehicle travels parallel to the first vehicle, but does not operate its receiver. The triangles on the left represent the receiver measurements. The actual system will continuously take measurements and average adjacent measurements over a small aperture (approximately one half wavelength) and this averaged result is a single measurement. The dots on the bedrock represent the pixels of the reflectivity map. The pixel resolution is denoted by $s_x$.

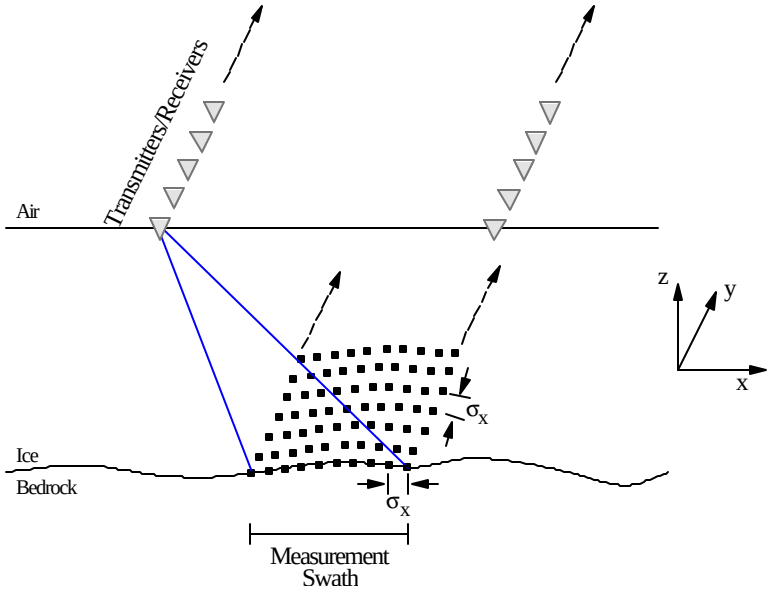


*Figure 2-2: Illustration of monostatic two-dimensional mapping.*

The bistatic configuration is shown in Figure 2-3. In this mode, the second vehicle's receiver will be active. The transmitter will effectively stop at each triangle and pulse the radar as the receiver moves along the x-axis transect building the synthetic beam-forming aperture, capturing energy from both end-points of the swath. When the cross-track aperture formation is finished, both the receiver and transmitter move forward in the along-track (positive y) direction and repeat the process. The expected swath and pixel resolution $s_x$ are indicated.

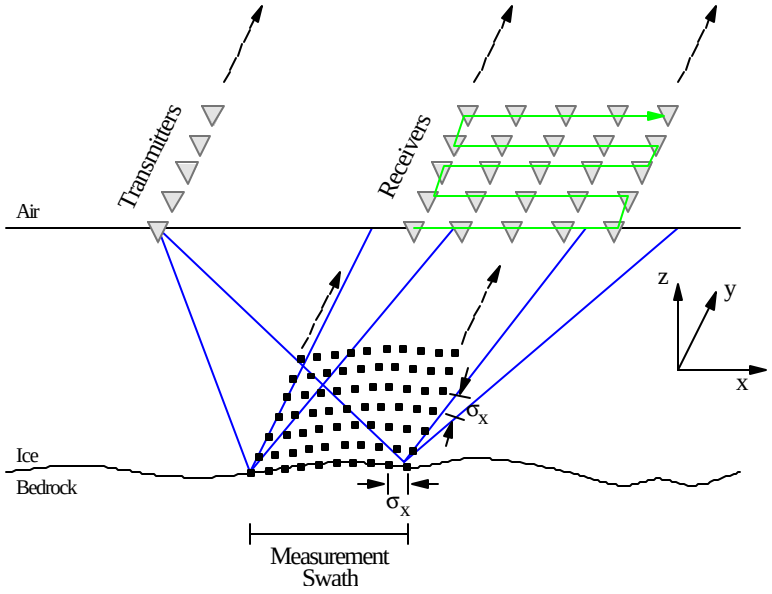


*Figure 2-3: Illustration of bistatic two-dimensional mapping.*

Both modes collect a set of measurements at different spatial positions. The synthetic array processor then collects these raw measurements together from the synthetic aperture, forms a filter with coefficients based on the system model and the desired target location, and filters the data. If the data closely match the expected response from the desired target location, then the filter should indicate a strong reflector at that location. The ability of the filter to resolve two adjacent targets with different reflectivities depends on how similar the expected response from each target is. This is comparable to a band-pass filter's ability to distinguish two frequencies from one another by selecting one and rejecting the other.

One consideration that must be made when using radar over a dielectric half space is that the launch angles into a denser medium such as ice will be restricted by the critical angle. This means that the maximum length of the SAR aperture will be limited by the refraction in the denser medium. This is similar to limiting the delay of a band-pass filter. The delay is the time period of the input over which the filter can form an output. When the time period of the input is limited the filter's frequency resolution is worsened. As mentioned above, by placing the antenna on the surface of the ice, this size limitation on the SAR aperture can be mitigated slightly.

When a plane wave strikes a boundary between two layered media, the phase terms in each media must be equal to ensure that the tangential electric and magnetic fields are continuous across the boundary. This equality is expressed in Snell's Law.

$$n_1 \sin q_i = n_2 \sin q_t \tag{2.1}$$

When the second medium is denser than the first $n_2 > n_1$, the maximum value of $q_t$ is less than ninety degrees. Solving Snell's law for $q_t$:

$$q_t = \sin^{-1}\left(\frac{n_1}{n_2}\sin q_i\right) \tag{2.2}$$

When $q_i$ is ninety degrees, $\sin q_i$ is at its maximum value of unity and $q_t$ is also at its maximum value which is

$$q_t = \sin^{-1}\left(\frac{n_1}{n_2}\right) = q_C \tag{2.3}$$

The maximum transmission angle is called the critical angle $q_C$. When a plane wave strikes a boundary from the opposite direction (effectively switching $n_1$ and $n_2$), angles beyond the critical angle undergo total reflection. Therefore, when attempting to focus with SAR under the plane wave approximation, the maximum look angle is restricted [26] (the look angle is measured from nadir in this case).

While the waves undergo total reflection, an EM-field exists in the second medium called an evanescent wave (non-traveling wave). Assuming the second medium is lossless, this wave does not transmit energy once it has been established (e.g. steady-state sinusoid). If an antenna is placed directly on the boundary, then it is able to couple energy from this evanescent wave and hence transmit and receive energy beyond the critical angle [26] (there are still limitations however). The antenna disrupts the planar boundary and the antenna's impedance can be set to match the impedance of the denser medium beneath the antenna. Another qualitative way to look at this is to consider that an antenna that is directly on the boundary is as

much in the second medium as the first and should therefore be able to couple energy at angles beyond the critical angle.

## 2.2 MEASUREMENT MODEL

The general form of the measurements that will be used to model the radar scene is described now. We will assume that the scene of interest is linear, and therefore the total radar response for each measurement can be found from adding the individual responses from each target. Additionally, the noise is assumed to be complex additive Gaussian noise. Using these two assumptions, the set of measurements can be described as

$$x = Gs + n \tag{2.4}$$

$x$ is a complex n-by-1 vector of n measurements. $s$ is an m-by-1 vector and represents the complex weight of each of the m targets. The linear map between the measurements and the targets is expressed in the complex matrix $G$ that has size n-by-m. The matrix $G$ is the expected target response evaluated for each measurement and target pair; the targets are assumed to have unity weight when calculating $G$ since $s$ represents the target weights. Each column of $G$ is the reference function for the corresponding target in the vector $s$. The columns or reference functions of $G$ are assumed to be linearly independent (linear dependence would mean that perfect ambiguities exist between targets). The noise, $n$, is a complex multivariate Gaussian random vector of size n-by-1 with a cross-correlation matrix of $\Sigma_n$ that is assumed to be nonsingular.

The complex weight of target $i$ is represented by the $i^{th}$ element of $s$ which will be denoted $s_i$. The weight is the unknown parameter being estimated by the SAR processor and is analogous to the radar cross-section of an isotropic target. When determining $s_i$, $G$ is assumed to be known and is found using the system model. The ideal filter finds the $s_i$ given $x$ that best meets a certain criteria. In most of this thesis, we will only consider the matched filter which maximizes signal to

noise ratio. One of the biggest drawbacks of the matched filter is that it only considers noise and does not consider interference from other targets (examples of filters that do consider other targets are the maximum likelihood filter and the minimum mean squared error filter).

## 2.3 SYSTEM MODEL

To create a filter, the nature of and relationship between measurements, expressed in $G$, must be known. The system model creates the columns of G by finding the reference function for each target. The system model is divided into two parameters: the magnitude and the phase. The radar equation is used in the system model to determine the magnitude response, and the range, transmitter/receiver transfer function, and antenna delay are used to determine the phase. Polarization and extinction losses are not considered in the system model.

The steady-state radar equation (2.5) determines the receive power, $P_R$, at a single frequency for a particular transmit power, $P_T$, transmitter response, $H_T$, transmit antenna efficiency, $h_{Teff}$, transmit antenna directivity, $D_T$, transmitter to target separation, $R_T$, scattering cross-section, $s_{bs}$, target to receiver separation, $R_R$, effective area of the receiving antenna, $A_R$, receive antenna efficiency, $h_{\mathrm{Re}\,ff}$, and receiver response, $H_R$ [25]. The following form of the radar equation assumes that the gain of the antennas and the ranges are constant over the target area (i.e. the scattering cross-section is directly related to the target area). Some of the terms, especially the antenna parameters and transmitter and receiver responses, tend to be functions of frequency which will be an important consideration when choosing the time or frequency domain for processing.

$$P_R = P_T H_T h_{Teff} D_T \frac{s_{bs}}{4pR_T^2} \frac{A_R}{4pR_R^2} h_{\mathrm{Re}\,ff} H_R \tag{2.5}$$

The radar equation provides the ability to gain a first-order understanding of the response from a set of targets. This has two purposes. It can be used to create

simulated data sets that can be used for processing and evaluation and as input to the link budget. It also provides the filter coefficients (or at least a first approximation of the coefficients) to the SAR processing algorithms. The results from this section are used for predicting and processing the measured results from the sandbox in our GPR lab. The following details show how each of the parameters in (2.5) is determined.

The transmitter and receiver responses, $H_T$ and $H_R$, are measured with a network analyzer. Similarly, the antenna parameters, $h_{Teff}$, $D_T$, $h_{\mathrm{Re}\,ff}$, and $A_R$ are measured at each launch angle with a network analyzer. The targets are approximated by a set of isotropic point radiators with frequency-independent complex weights. Therefore, the radar cross-section, $s_{bs}$, is not directly represented in the radar equation, but can be approximated by the proper spatial configuration of point targets and weights associated with these targets. Finally, spherical losses are handled by finding the ranges from the transmitter to the target and from the target to the receiver by using a ray-trace approximation at dielectric interfaces.

Note that the radar equation only gives the magnitude response. To determine the phase response of the system, propagation delays and equipment phase information must be known. The propagation delay is found from refraction, path length and changes in velocity. The equipment phase delay is determined from the measured $S_{21}$ parameters of the transmitter and receiver responses and from the antenna $S_{21}$ measurements.

To determine the path lengths and the amount of spherical spreading requires knowledge of how the ray was refracted along its traverse. The focusing algorithms are given the antenna positions and are asked to determine the complex weight for a particular target position. In a homogeneous medium, the ray follows a straight path to the target. With a dielectric half-space in between the antennas and the target, the ray is bent and the two component rays must be determined from the positions and the properties of the dielectrics (see Figure 2-4 below). In a multilayered medium, the effect of multiple refractions must be considered.

Each of the ray-trace models used in this thesis to determine range varies slightly. The system model used in chapter 3 includes only the propagation delay, but uses a multilayered ray-trace model for determining the range to each target. Chapter 4 also only includes the propagation delay and only for a homogeneous medium. Chapter 5, which gives the results from the sandbox laboratory tests includes the entire system model described here and uses a dielectric half-space (air and sand) to determine the ranges. Each of these ray-trace models is explained in the following sections.

### 2.3.1 LAYERED MEDIUM (CHAPTER 3)

The layered medium ray-tracing model is described in [27]. Here an ice core profile from Greenland has been converted into a dielectric profile. This continuous dielectric profile is approximated by discrete layers so that the ray-tracing approximation can be applied. A lookup table rather than a closed form solution is used in this case.

### 2.3.2 HOMOGENEOUS MEDIUM (CHAPTER 4)

This ray-tracing model is the simplest of the three. The sum of the distance between the transmitter and the target and between the target and the receiver gives the path length. The dielectric of the homogeneous medium is used to convert this path length into a time delay. No refraction is present in this model.

### 2.3.3 DIELECTRIC HALF-SPACE (CHAPTER 5)

A dielectric half-space has two media present and the boundary is assumed to be flat. The geometry for this ray-tracing model is given in Figure 2-4. The half-space boundary is considered to be at $z = 0$ for the calculations below.

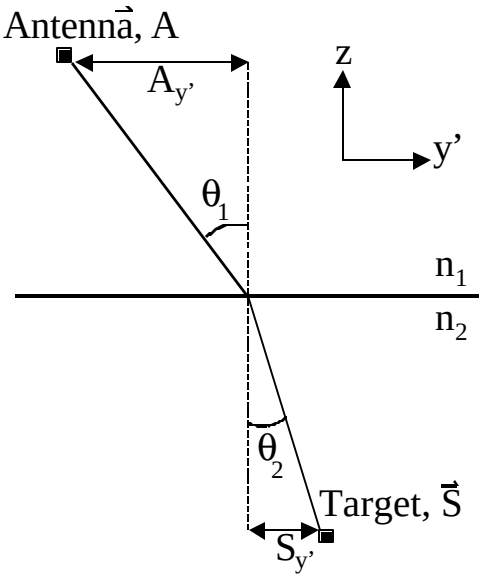


*Figure 2-4: Geometry for solving refraction problem.*

We start with Snell's law that comes from the need to have the tangential electric and magnetic fields be continuous at the half-space boundary.

$$n_1 \sin(q_1) = n_2 \sin(q_2) \tag{2.6}$$

Even though $\vec{A}$ and $\vec{S}$ are three-dimensional coordinates, the rays that connect them lie completely within the plane of incidence. Therefore, we can treat the problem in two-dimensions with the $y'$ separation defined as $y' = \sqrt{(A_x - S_x)^2 + (A_y - S_y)^2}$ and the $y'$ unit vector described as

$$\hat{a}_{y'} = \frac{\left((S_x - A_x)\hat{a}_x + (S_y - A_y)\hat{a}_y\right)}{\left|(S_x - A_x)\hat{a}_x + (S_y - A_y)\hat{a}_y\right|} \tag{2.7}$$

We would then like to find the displacement along the $y'$ axis between the refraction point and the antenna ( $A_{y'}$ ) or target ( $S_{y'}$ ). These displacements are related to Snell's law by the following two trigonometric identities.

$$\sin(q_1) = \frac{A_{y'}}{\left(A_{y'}^2 + A_z^2\right)} \quad \text{and} \quad \sin(q_2) = \frac{S_{y'}}{\left(S_{y'}^2 + S_z^2\right)} \tag{2.8}$$

Plugging these into Snell's law gives the following.

$$\frac{n_1 A_{y'}}{\left(A_{y'}^2 + A_z^2\right)^{1/2}} = \frac{n_2 S_{y'}}{\left(S_{y'}^2 + S_z^2\right)^{1/2}} \tag{2.9}$$

We also know that $y' = A_{y'} + S_{y'}$ or $A_{y'} = y' - S_{y'}$.

$$\frac{n_1 \left(y' - S_{y'}\right)}{\left(\left(y' - S_{y'}\right)^2 + A_z^2\right)^{1/2}} = \frac{n_2 S_{y'}}{\left(S_{y'}^2 + S_z^2\right)^{1/2}} \tag{2.10}$$

Squaring, cross-multiplying and grouping power terms of $S_{y'}$:

$$\begin{aligned}&\left(n_1^2 - n_2^2\right) S_{y'}^4 - 2y'\left(n_1^2 - n_2^2\right) S_{y'}^3 + \left(n_1^2\left(y'^2 + S_z^2\right) - n_2^2\left(y'^2 + A_z^2\right)\right) S_{y'}^2 \\ &\quad - 2y' n_1^2 S_z^2 S_{y'}^1 + y'^2 n_1^2 S_z^2 S_{y'}^0 = 0\end{aligned} \tag{2.11}$$

This fourth order polynomial can be solved using Matlab's roots function. Only one of the roots will be real and within the range from 0 to $y'$ unless there is a double root at 0 (in the case when y' equals zero for a target placed directly beneath the antenna). From $S_{y'}$, we can find $A_{y'} = y' - S_{y'}$.

With $A_{y'}$ and $S_{y'}$ we can then find the two component rays starting from the transmit antenna and traveling to the target as:

$$R_{T1} = A_{y'}\hat{a}_{y'} - A_z\hat{a}_z \text{ and } R_{T2} = S_{y'}\hat{a}_{y'} + S_z\hat{a}_z \tag{2.12}$$

Similarly for the ray traveling from the target to the receive antenna:

$$R_{R1} = A_{y'}\hat{a}_{y'} + A_z\hat{a}_z \text{ and } R_{R2} = S_{y'}\hat{a}_{y'} + S_z\hat{a}_z \tag{2.13}$$

Taking the path length in each medium and dividing by the appropriate velocity gives the propagation delay.

## 2.4 MATCHED FILTER

As mentioned above, the matched filter considers each target separately. Therefore, when determining the matched filter only the $i^{th}$ column of $G$ is considered which is denoted by the vector $g_i$ and only the $i^{th}$ target weight will be considered and is denoted by the scalar $s_i$. When considering only the $i^{th}$ target, Equation (2.4) simplifies to:

$$x = g_i s_i + n \tag{2.14}$$

The matched filter chooses the weight coefficients $f_1, f_2, \ldots, f_n$ such that the weighted sum of the n measurements of $x$ maximizes the signal to noise ratio. Forming $f_1, f_2, \ldots, f_n$ into a vector called $f$, the estimator output, $\hat{s}_i$, of the matched filter is:

$$\hat{s}_i = f^H x = f^H (g_i s_i + n) = f^H g_i s_i + f^H n \tag{2.15}$$

where H denotes the Hermitian or complex conjugate transpose. The signal component of $\hat{s}_i$ is $f^H g_i s_i$ and the noise component is $f^H n$. The signal to noise ratio is then

$$\frac{E\left\{\left\| f^H g_i s_i \right\|_2^2\right\}}{E\left\{\left\| f^H n \right\|_2^2\right\}} \tag{2.16}$$

where $\|\cdot\|$ is the 2-norm (i.e. $\|v\|_2^2 = v^H v$). Evaluating the 2-norm in the numerator gives:

$$E\left\{\left\| f^H g_i s_i \right\|_2^2\right\} = E\left\{\overline{s_i} g_i^H f f^H g_i s_i\right\} \tag{2.17}$$

Using the inner product of two vectors defined by $\langle v, w \rangle = v^H w$, we can rewrite (2.17) as

$$E\left\{\left\| f^H g_i s_i \right\|_2^2\right\} = E\left\{\left|s_i\right|^2 \left\langle g_i, f\right\rangle \left\langle f, g_i\right\rangle\right\} \tag{2.18}$$

Since inner products have conjugate symmetry we have

$$E\left\{\left\| f^H g_i s_i \right\|_2^2\right\} = E\left\{\left|s_i\right|^2 \left\langle g_i, f\right\rangle \overline{\left\langle g_i, f\right\rangle}\right\} \tag{2.19}$$

The inner products are independent of the random variable and can be taken outside of the expectation.

$$E\left\{\left\| f^H g_i s_i \right\|_2^2\right\} = \left|\left\langle g_i, f\right\rangle\right|^2 E\left\{\left|s_i\right|^2\right\} \tag{2.20}$$

Finally, using the Schwarz Inequality, $\left|\left\langle g_i, f\right\rangle\right| \le \left\|g_i\right\|_2 \left\|f\right\|_2$, we have:

$$E\left\{\left\| f^H g_i s_i \right\|_2^2\right\} \le \left\|g_i\right\|_2^2 \left\|f\right\|_2^2 E\left\{\left|s_i\right|^2\right\} \tag{2.21}$$

with equality only when $f$ and $g$ are linearly dependent.

Evaluating the 2-norm in the denominator:

$$E\left\{\left\| f^H n \right\|_2^2\right\} = E\left\{n^H f f^H n\right\} \tag{2.22}$$

$$E\left\{\left\| f^H n \right\|_2^2\right\} = E\left\{\left\langle n, f\right\rangle \left\langle f, n\right\rangle\right\} \tag{2.23}$$

$$E\left\{\left\| f^H n \right\|_2^2\right\} = E\left\{\left(\overline{n_1} f_1 + \overline{n_2} f_2 + \cdots + \overline{n_n} f_n\right)\left(n_1 \overline{f_1} + n_2 \overline{f_2} + \cdots + n_n \overline{f_n}\right)\right\} \tag{2.24}$$

If we assume that the noise between measurements is independent then the cross terms will be zero so that

$$E\left\{\left\| f^H n \right\|_2^2\right\} = E\left\{\overline{n_1} f_1 n_1 \overline{f_1}\right\} + E\left\{\overline{n_2} f_2 n_2 \overline{f_2}\right\} + \cdots + E\left\{\overline{n_n} f_n n_n \overline{f_n}\right\} \tag{2.25}$$

$$E\left\{\left\| f^H n \right\|_2^2\right\} = \left|f_1\right|^2 E\left\{\left|n_1\right|^2\right\} + \left|f_2\right|^2 E\left\{\left|n_2\right|^2\right\} + \cdots + \left|f_n\right|^2 E\left\{\left|n_n\right|^2\right\} \tag{2.26}$$

If the noise is identically distributed then we have:

$$E\left\{\left\| f^H n \right\|_2^2\right\} = \left\|f\right\|_2^2 E\left\{\left|n_i\right|^2\right\} \tag{2.27}$$

Plugging the results back into (2.16):

$$SNR \le \frac{\|f\|_2^2 \|g_i\|_2^2 E\left\{\|s_i\|_2^2\right\}}{\|f\|_2^2 E\left\{\|n_i\|_2^2\right\}} = \frac{\|g_i\|_2^2 E\left\{\|s_i\|_2^2\right\}}{E\left\{\|n_i\|_2^2\right\}} \tag{2.28}$$

Therefore, any set of filter coefficients $f$ for which $f = ag_i$ holds for some $a \in \Re$ maximizes the signal to noise ratio. If we choose $f = \frac{g_i}{\|g_i\|_2^2}$, then the filter output is

$$\hat{s}_i = f^H g_i s_i + f^H n = \frac{g_i^H}{\|g_i\|_2^2} g_i s_i + \frac{g_i^H}{\|g_i\|_2^2} n = s_i + \frac{g_i^H}{\|g_i\|_2^2} n \tag{2.29}$$

As the noise tends toward zero, the estimated target weight tends towards its actual value. This is the matched filter that will be used to SAR process the simulated and measured results throughout this thesis.

## 2.5 MAXIMUM LIKELIHOOD FILTER

The advantage of the maximum likelihood filter is that it simultaneously considers all the targets rather than just one at a time. Considering one target at a time usually leads to interference between closely spaced targets. While the matched filter maximizes signal to noise ratio, the maximum likelihood filter maximizes the signal to interference ratio, and within this subset of results (i.e. the subspace orthogonal to the other measurements), it maximizes the signal to noise ratio. The general form of the measurements given in (2.4) is used and the result for independent, identically distributed noise, as derived in appendix A, is:

$$f^H = \left(G^{\sim 1}\right)_i \tag{2.30}$$

where $G^{\sim 1} = \left(G^H G\right)^{-1} G^H$ is the pseudo-inverse of $G$ and $\left(G^{\sim 1}\right)_i$ is the $i^{th}$ row of this matrix. Each of the rows of $G^{\sim 1}$ is orthogonal to each of the columns of $G$, using an

inner product defined by $\langle v, w \rangle = v^H w$, except for the inner product of the $i^{th}$ row with the $i^{th}$ column, which is unity. The output of the filter is then

$$\hat{s}_i = \left(G^{\sim 1}\right)_i x = \left(G^{\sim 1}\right)_i (Gs + n) = s_i + \left(G^{\sim 1}\right)_i n \tag{2.31}$$

As shown in the appendix, when only one target is considered, the maximum likelihood filter simplifies to the matched filter results given above.

## 2.6 PROCESSING DOMAIN

The data received from the radar will be sampled in time and in space[3]. At each spatial position a set of time samples are taken. These time samples are associated with range bins and will always be regularly spaced in time according to the sampling frequency. The set of time-samples at a particular position is called an A-scope. The spatial positions will generally be regularly spaced, but not necessarily.

Each sample is considered to be a measurement and is tagged with a particular time and spatial position. These measurements are arranged into a single n-by-1 vector that we have called $x$. For processing, the A-scopes can be converted to the frequency domain. This is advantageous since the characterization of much of the system is in the frequency domain and multiplying transfer functions is much faster than convolving impulse responses. Similarly the spatial samples can be converted to the wavenumber domain (i.e. spatial frequency domain). Since the spatial samples are not necessarily regularly spaced, the conversion to the wavenumber domain can be difficult. Additionally, in bistatic mode, the transmitter and receiver beam patterns are not easily accounted for in the wavenumber domain. Another potential advantage of staying in the space domain is that target estimates can be updated at each spatial position rather than after a traverse is collected (since the whole traverse is needed when converting to the wavenumber domain).

[3] The data for the sandbox laboratory tests was collected with a network analyzer so this test data is actually sampled in frequency and space.

### 2.6.1 SPACE-FREQUENCY

The space-frequency domain was chosen for processing for the reasons listed above. This means that the variables $x$, $G$, $s$, and $n$ in equation (2.4) are all in the space-frequency domain. The EM-model from section 2.3 determines the value of $G$, $x$ is the actual data reshaped into a vector, and the value of $s$ is estimated using one of the filters described above.

The matched filter above could be used to match to any target situation as long as the possible set of targets can be represented by complex weights and related linearly to the measurements through the linear map $G$. Therefore, we could determine the response from an ensemble of surfaces, using the EM-model to determine the values of $G$ for each surface. The problem is that the number of possible surfaces is unmanageable (since we would want to consider different reflection and scattering characteristics as well as undulations in the topology). For this reason, the scene is usually broken into a lattice of uncorrelated isotropic point targets. The expected response, $G$, from each of the point targets in the lattice is determined with the EM-model. If every point target along a contour has a strong return, this may be interpreted as a surface rather than a set of discrete point targets. How the returns are interpreted will depend at least in part on our *a priori* knowledge of the scene.

The assumption that a lattice of uncorrelated point targets can represent the scene does not always hold. Specular surfaces (or any set of correlated targets) have the potential of destructively interfering to effectively remove the response from a particular set of targets. With a perfectly flat surface of infinite extent, the energy that the receiver detects is focused into a specular response that comes from one point even though the energy detected is actually the aggregate from the entire surface. The effects of smooth (with respect to wavelength) surfaces on the processing are considered in chapter four.

Another consideration is multipath, or reflections between targets. This creates considerable modeling problems since the number of possible multipath

situations grows as the $n^{th}$ power of the number of targets where n is the number of reflections that are considered. The problem is really only tractable when the multipath sources are known and restricted to a few sources. In the case of the ice sheet, multipath besides what can be handled with propagation matrices through layered media is not a substantial effect and does not need to be considered[4]. In the sandbox, multipath could exist between the horn antennas in the sandbox and the sand surface. However, the multipath was weak enough in this case to be ignored. The two assumptions, uncorrelated isotropic scatterers and no multipath make up the uncorrelated weak-scatterer assumption that is used in the filtering/SAR processing presented in this thesis.

### 2.6.2 F-K MIGRATION

As noted in the previous section, the space-time data can be converted to the frequency-wavenumber (or f-k) domain. To use the multi-dimensional FFT, the data must be regularly spaced in both the time and space domains. Once the data are converted, the filters derived above can be applied as before as long as $x$, $G$, $s$, and $n$ are all in the frequency-wavenumber domain. If the data are regularly spaced in both space and time, one can take advantage of a method called f-k migration. The primary advantage of f-k migration over processing in other domains is speed. F-k migration also handles layered interfaces very naturally both in terms of refraction and changes in velocity (although it does not account for multiple reflections).

To explain f-k migration, an analogy restricted to a single dimension is helpful. Suppose that a plane-wave is traveling in the positive x-direction so that $\|k\|_2 = k_x = -\frac{2p}{l}$. Since the direction of the wave is set, the wave can be completely described by its frequency response. Let us say that we have a receiver at the origin.

[4] In an airborne radar, multipath between the aircraft and the ice surface can occur since the airplane is a strong reflector.

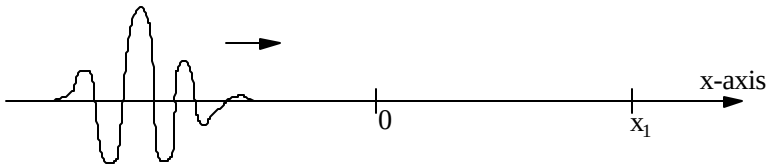


*Figure 2-5: f-k migration in one dimension.*

Let $s_0(t)$ denote the signal recorded by the receiver. To determine the plane-wave at a point x on the x-axis, call it $s_x(t)$, we can add a delay of $\frac{x}{v}$ so that $s_x(t) = s_0\left(t - \frac{x}{v}\right)$ where $v$ is the velocity of the wave in the medium. In the frequency domain, using the time-shift property, this is:

$$S_x(f) = S_0(f)\exp\left(j2pf\left(\frac{-x}{v}\right)\right) \tag{2.32}$$

$$= S_0(f)\exp\left(-j\frac{2pf}{v}x\right) \tag{2.33}$$

$$= S_0(f)\exp\left(jk_x x\right) \tag{2.34}$$

Therefore to determine the frequency response at a position x, we need to multiply $S_x(f)$ with $\exp(jk_x x)$. In the general case, $\|k\|_2 = \frac{2p}{l} = \sqrt{k_x^2 + k_y^2 + k_z^2}$. Since $k_y = k_z = 0$ and the wave is traveling in the positive direction we have $k_x = -\frac{2p}{l}$.

To determine the value at zero-time from the frequency domain response (this will be needed later) we sum all the frequency components together:

$$s(0) = \int_{-\infty}^{\infty} S(f)\exp(j2pf \cdot 0)df = \int_{-\infty}^{\infty} S(f)df \tag{2.35}$$

Or if the signal is discrete and of finite length N we have:

$$s(0) = \frac{1}{N}\sum_{n=0}^{N-1} S(n)\exp(j2pnf_0 \cdot 0) = \frac{1}{N}\sum_{n=0}^{N-1} S(n) \tag{2.36}$$

If the plane-wave is allowed to travel in three dimensions there are three free variables $k_x$, $k_y$, and $k_z$ but only one constraint equation. However, if we have samples in the x and y domain (e.g from a synthetic aperture) we can use this information to determine $k_x$ and $k_y$. This leaves only $k_z$ which can be found as:

$$k_z = \pm\sqrt{\left(\frac{2p}{l}\right)^2 - k_x^2 - k_y^2} \tag{2.37}$$

Assuming that the waves are coming from the negative z direction and substituting in frequency for wavelength this becomes

$$k_z\left(f, k_x, k_y\right) = -\sqrt{\left(\frac{2pf}{v}\right)^2 - k_x^2 - k_y^2} \tag{2.38}$$

Therefore, if we have space-time data that are collected on the surface of the ice sheet or the sandbox, we will have sampled in the time, x, and y dimensions (assuming negative z is normal to the surface and points into the ice/sand). This data can be transformed to the frequency-wavenumber domain through a three-dimensional FFT. Each point in the three-dimensional FFT is associated with a corresponding $f$, $k_x$, and $k_y$ given by:

$$f = \frac{-1}{2dt}, \frac{-1}{2dt} + \frac{1}{N_t dt}, \frac{-1}{2dt} + \frac{2}{N_t dt}, \ldots, \frac{1}{2dt} - \frac{1}{N_t dt} \tag{2.39}$$

$$k_x = \frac{-1}{2dx}, \frac{-1}{2dx} + \frac{1}{N_x dx}, \frac{-1}{2dx} + \frac{2}{N_x dx}, \ldots, \frac{1}{2dx} - \frac{1}{N_x dx} \tag{2.40}$$

$$k_y = \frac{-1}{2dy}, \frac{-1}{2dy} + \frac{1}{N_y dy}, \frac{-1}{2dy} + \frac{2}{N_y dy}, \ldots, \frac{1}{2dy} - \frac{1}{N_y dy} \tag{2.41}$$

where $dt$, $dx$, and $dy$ are the spacings in the original space-time domain and $N_t$, $N_x$, and $N_y$ are the number of samples in each dimension (assumed to be even). To predict the signal that would have been measured if the receivers were placed 1 m in

the negative z-direction, we solve for $k_z\left(f,k_x,k_y\right)$ using (2.38) at each data point and then apply a delay as before in (2.34):

$$S_{-1\mathrm{m}}\left(f,k_x,k_y\right)=S_0\left(f,k_x,k_y\right)\exp\left(jk_z\left(f,k_x,k_y\right)\cdot -1\right) \tag{2.42}$$

The result is the predicted frequency response that would have been observed if the receivers had been placed 1 m below their actual positions. This process can be used to find the predicted waveform at any position (x, y, or z) by multiplying by the appropriate spatial phase shift. Note that this shifts all the spatial measurements simultaneously, which is key to fk migration's speed advantage over space or time domain processing.

To apply this spatial shifting to radar processing, we must consider the position of the transmitter, which generates the original signal $s(t)$. In the monostatic case, the transmitter and receiver are collocated – if the receiver is moved, the transmitter must also be moved. The original signal $s(t)$ is delayed by the transmitter movement and the received signal is delayed further by the receiver movement. This collocation effectively doubles the effect of the radar movement. This can be dealt with by doubling the index of refraction of the medium. Using the simplified example from above, the delay for the receiver movement is $\frac{x}{v}$. The delay for the transmitter movement is also $\frac{x}{v}$. Therefore the total delay is $\frac{2x}{v}$. Since the doubling factor appears everywhere the velocity or wavelength is used, we can interpret the effect as a doubling of the index of refraction.

The fk migration technique involves moving the radar to each of the target positions of interest via phase shifts and reading the zero-time response. If there is a strong response at zero-time after moving (phase shifting) the radar then there is should be a target in the immediate vicinity of the radar since a zero-time delay corresponds to zero range. Since we generally treat the scene as a lattice of isotropic point targets, the fk migration technique can process whole sections of the lattice simultaneously. This is because the entire SAR aperture is moved when the phase

shift is applied rather than each "receiver" being moved individually. Since each "receiver" in the SAR aperture gives the response at that point we have simultaneously determined the response at N new points. In other words, if the SAR aperture has N elements in it, we can process N targets after each phase shift (assuming the SAR aperture matches up with the lattice of isotropic point targets).

The final response needed by the processing is usually in the space-domain. As mentioned above, the value at zero-time can be found by summing all of the frequency points. This should be done before transforming from the wavenumber domain to the space domain using the IFFT. By summing first, the number of IFFTs is reduced by a factor of $N_t - 1$.

In the bistatic mode, the transmitter does not have to move with the receiver. This complicates matters because the received signal is now a function of the transmitter, receiver, and target locations. This means that after the receiver has been moved back to the target location, an additional phase delay due to the transmitter-target separation must be accounted for. This effectively negates the speed advantage that processing in the frequency-wavenumber domain provides. One possibility for applying the phase shift on a per-target basis is the following. The data is converted from the wavenumber domain to the space domain so that a per-target phase shift can be applied. The delay between each transmitter/target pair is found. The delay is then converted into phase shifts that form a set of frequency dependent weights. Finally the inner product between the corresponding phase shift and target response gives the value at zero-time. The inner product, in this case, component-wise multiplies the data with the conjugate of the phase shifts and then sums.

There are two caveats that need to be mentioned when using the f-k migration algorithm. The first is that the process above assumes that the signal is band-limited in space and time. If the signal were truly band-limited then there would be no energy in parts of the data matrix that correspond to $\sqrt{k_x^2 + k_y^2 + k_z^2} > \|k\|_2 = \frac{2p}{l}$. In other words, there are portions of the frequency-wavenumber data matrix that may

represent a combination of $k_x$, $k_y$, $k_z$, and $l$ that require the wave to be evanescent. The presence of evanescent waves is not necessarily a problem, but out-of-band signal/noise power can be aliased to the evanescent region. Based on simulated and measured results, this evanescent region should be gated out of the data before processing.

The second issue comes from the periodic nature of discrete representations. Because the signal is being represented discretely and circular convolution is being used in the frequency domain, zero-padding may be necessary in some cases to remove artifacts due to the non-linear nature of circular convolution (i.e. aliasing).

# CHAPTER 3: BISTATIC SENSOR GEOMETRY

## 3.1 INTRODUCTION

As mentioned in the preceding chapter, the bistatic mode will use synthetic beam-forming to improve the cross-track resolution. This requires creating a two-dimensional grid of receiver measurements as shown with the triangles in Figure 3-1. The spacings between each measurement (triangle) must meet a spatial version of Nyquist sampling frequency. For a perfectly rough bedrock surface and no restriction on launch angle into the ice, this is half wavelength sampling for beam-forming and quarter wavelength sampling for SAR. Also, the length of the cross-track transect (parallel to the x-axis) of the receiver must be long enough to image the entire measurement swath to a pixel resolution of $s_x$.

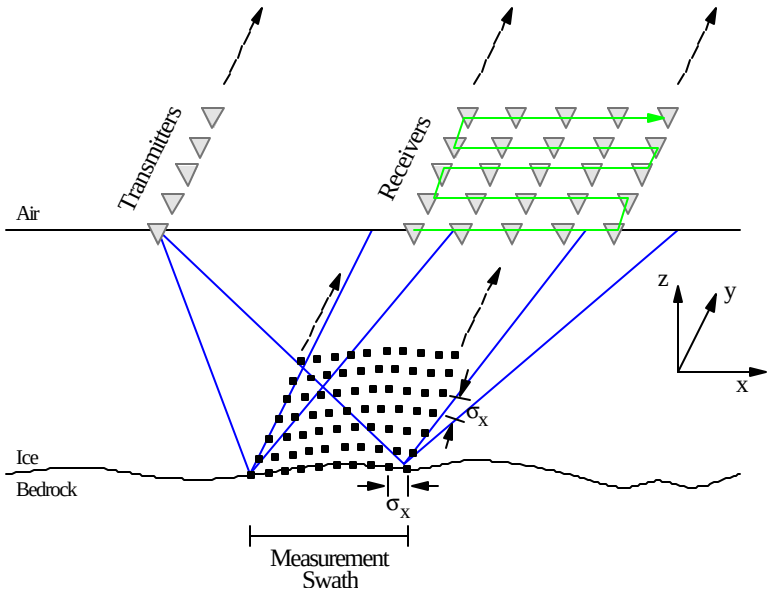


*Figure 3-1: Illustration of bistatic two-dimensional mapping.*

Two methods for improving traverse time are described in this chapter. The first method for minimizing measurement time is to choose the transmitter position such that it minimizes the cross-track traverse length. The second method uses a

small real-aperture aligned with the along-track direction to focus energy to a smaller section of the along-track. Using this technique, less sampling in the along-track direction is required to meet the Nyquist sampling rate. If the aperture is kept small enough, the SAR can still focus the measurements effectively.

## 3.2 IDEAL TRANSMITTER POSITION

### 3.2.1 BACKGROUND

The scattering properties of a surface are usually described in terms of the backscatter (for monostatic) and the forward-scatter (for bistatic). The amount of energy scattered is given with respect to the backscatter angle and forward-scatter angle respectively. The backscatter angle is the angle between the collocated transmitter/receiver and the nadir or normal line as shown on the left side of Figure 3-2. The forward-scatter angle is the angle between the receiver and the specular ray as shown on the right side of Figure 3-2. Because we do not currently have measurements of the forward-scatter for ice bedrock surfaces we used backscatter results. In this case, the backscatter angle of $r$ corresponds to a forward-scatter angle of $b = 2r$ (again shown in Figure 3-2).

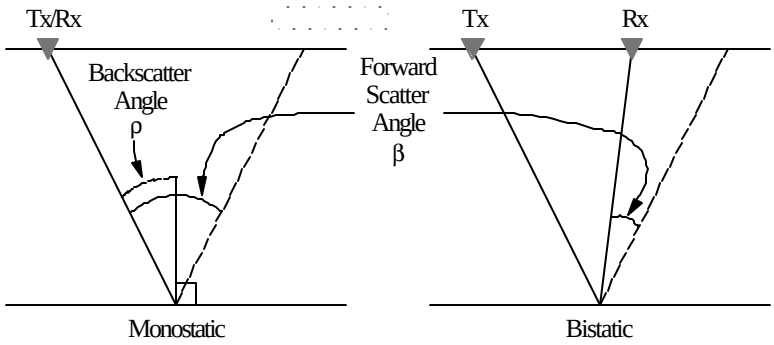


*Figure 3-2: The backscatter angle for the monostatic case is given in the left-hand image. The forward-scatter angle for both cases is shown along with a comparison to the backscatter angle. The rays from the transmitter to the target and from the target to the receiver are solid. The specular ray is dashed.*

The bedrock at several locations beneath the Greenland ice sheet was found to have a maximum backscatter angle, defined as being the largest backscatter angle in which significant energy is received[5], of around 4 to 7.5 degrees [19]. A small maximum backscatter angle limits the maximum synthetic array size. If we assume that the forward-scatter follows the same characteristics as the backscatter, this dictates that the receiver measurements to resolve a particular target must be taken within this small arc of scattered energy. To image a swath of bedrock, the two end-points of the swath determine the minimum and maximum extent of the receiver movement. This is shown in Figure 3-3 where $R_M$ is the minimum receiver movement such that the receiver will pick up a return from both end-points of the swath. $R_X$ is the maximum receiver movement that will receive energy from the two end-points of the swath.

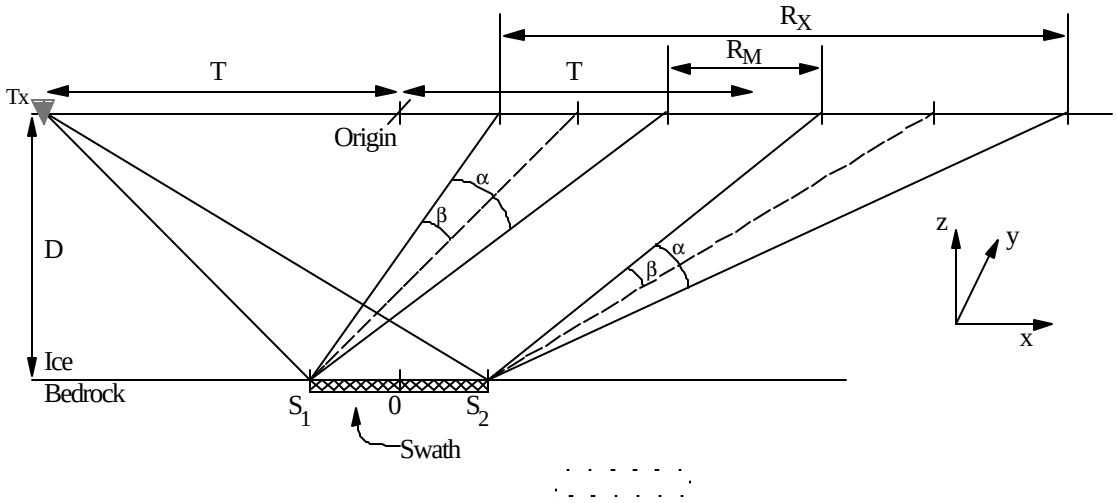


*Figure 3-3: $R_M$ and $R_X$ show the minimum and maximum receiver aperture sizes that include energy from the two end-points of the measurement swath ($S_1$ and $S_2$ are the end points).*

As the transmitter is moved away from the swath, the aperture size can be decreased as shown in Figure 3-4.

[5] The minimum receiver energy was taken to be 20 dB less than the nadir reflection (backscatter angle equal to zero).

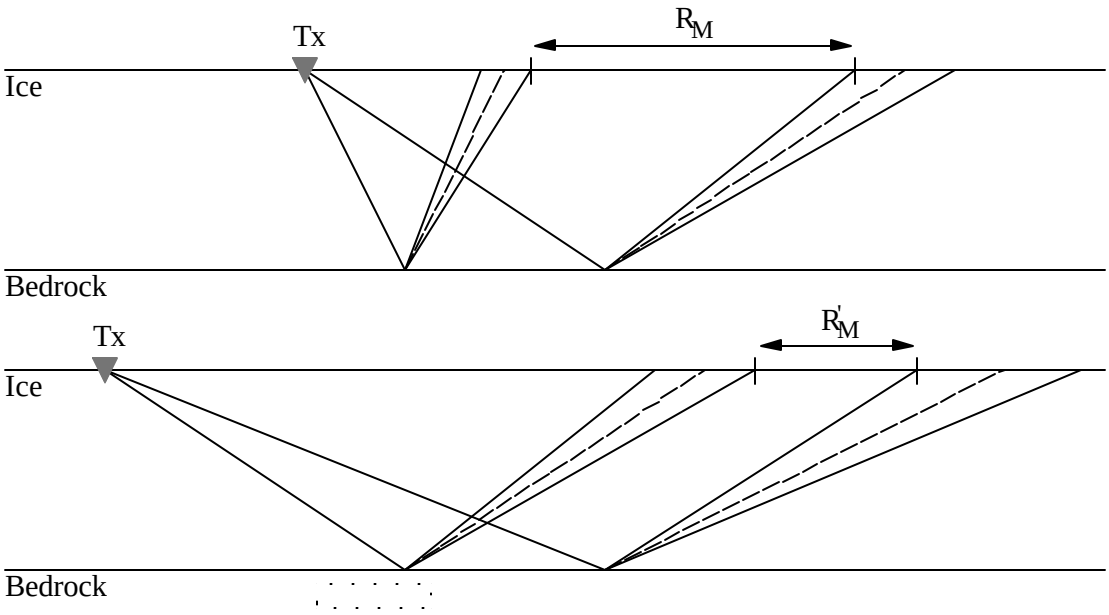


*Figure 3-4: As the transmitter is moved away from the swath, the minimum receiver aperture decreases (i.e. $R_M' < R_M$).*

Concurrent to this decrease in the receiver aperture, is a degradation of the spatial resolution. As the swath moves away from the broadside of the receiving antenna, two factors begin to degrade the spatial resolution. The first factor is that the angular resolution becomes coarser as the beam is steered toward the end-fire case. The second factor is that the area subtended by the beam increases as the beam moves away from broadside. Because more bedrock is subtended within the same angle, $b_x$, the spatial resolution along the bedrock becomes coarser (see Figure 3-5). Therefore, not only does the angular resolution become coarser when the transmitter-receiver separation is increased, but the spatial resolution for a given angular resolution gets worse.

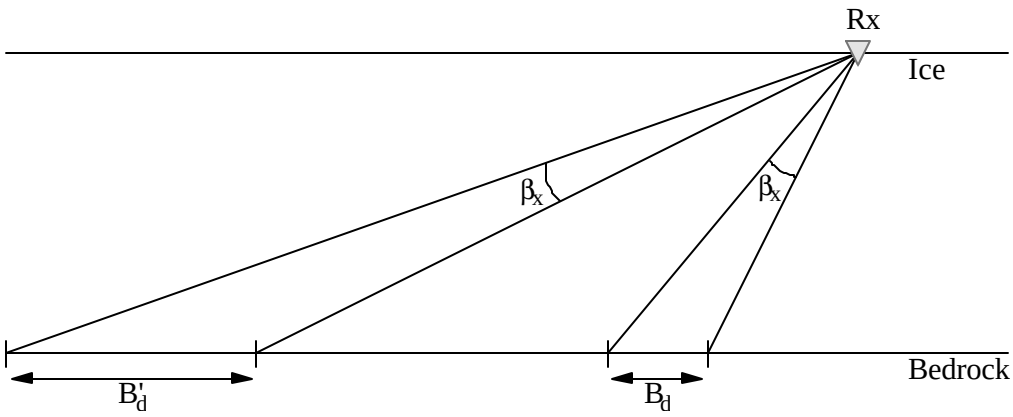


*Figure 3-5: The area subtended increases as the beam moves away from broadside and $B_d' > B_d$ for the same $b_x$.*

Because the resolution is degraded, a larger synthetic aperture must be formed to compensate for the degraded resolution. This required increase in the synthetic aperture size versus the decrease in minimum aperture represents the tradeoff that must be resolved. As a side note, this report does not account for path losses; but the power loss due to spherical power spreading and attenuation through the ice will increase for larger transmitter-receiver separations. While this factor is ignored in the calculations presented below, it should be included in the final decision on what the transmitter-receiver separation to ice thickness ratio should be.

### 3.2.2 DERIVATION OF MINIMUM BISTATIC APERTURE

We want to find the transmitter position, T, which will minimize the receiver's required length. First, we find an equation that relates T to the receiver aperture size that meets our resolution and swath width criteria. We will then use this equation to iteratively find the value of T that minimizes the received aperture size. To model the forward-scattering, we will assume that it behaves similarly to backscattering and has a value of unity within $\pm b$ degrees of the specular point and is zero outside of these angles. Therefore if the backscatter has significant return for any angle up to five degrees incidence, we will set $b$ to be ten degrees. The reason for the doubling can be seen in Figure 3-6.

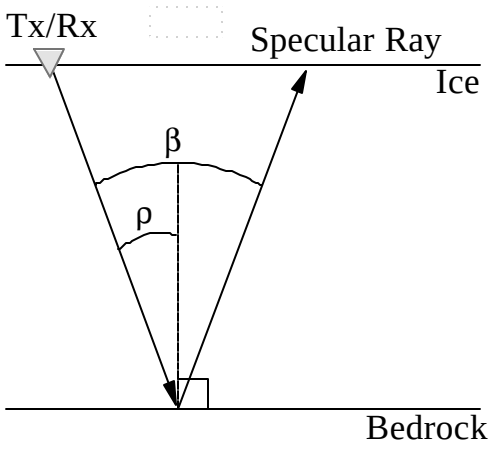


*Figure 3-6: A backscatter angle of $r$ has a forward-scatter angle of $b = 2r$.*

The next assumption that we make is that the receiver aperture is in the Fraunhoffer region (far-field) and we can use the plane wave approximation when determining the minimum synthetic aperture size required to achieve the desired resolution.

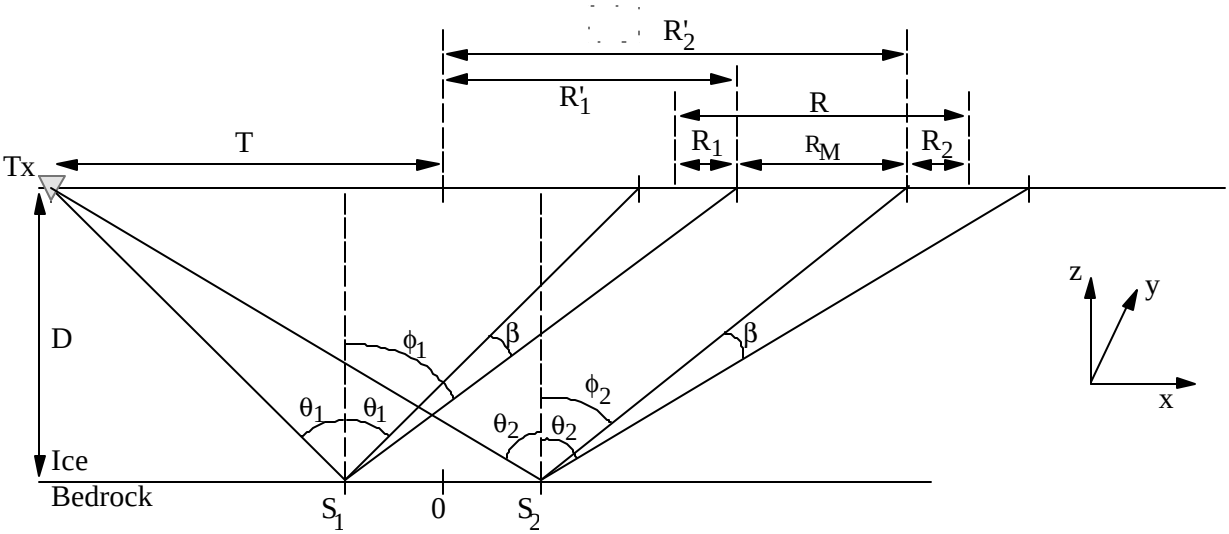


*Figure 3-7: System geometry.*

Given these assumptions, the next step is to look at our system geometry and label the values that will be of interest to us. This is done in Figure 3-7. The distance between the center of the swath and the transmitter antenna is called T. The thickness of the ice, or depth of the bedrock, is D. The angle $?_1$ is:

$$?_1 = \text{atan}\left(\frac{T - S_1}{D}\right) \tag{3.1}$$

The angle $?_1$ is the launch angle from the transmitter, Tx, to the closest target on the swath, $S_1$. Since the air/ice interface and ice/bedrock interfaces are parallel, $?_1$ is also the incident angle on to $S_1$. For plane waves incident on flat surfaces, the specular reflection angle will also be $?_1$.

The angle $f_1$ determines the ray from target $S_1$ that will reach the largest value on the x-axis. This scattering angle will be $b$ larger than $?_1$ since $b$ represents the maximum forward-scatter angle between the scattering angle and the specular reflection angle.

$$f_1 = ?_1 + b = \text{atan}\left(\frac{T - S_1}{D}\right) + b \tag{3.2}$$

Similarly for $S_2$, the angle $?_2$ is:

$$?_2 = \text{atan}\left(\frac{T + S_2}{D}\right) \tag{3.3}$$

The angle $f_2$ determines the ray from target $S_2$ that will reach the smallest value on the x-axis and is given by:

$$f_2 = ?_2 - b = \text{atan}\left(\frac{T + S_2}{D}\right) - b \tag{3.4}$$

$R_1'$, the distance from mid-swath to the far edge of the cone of energy scattered from the nearest end of the swath (relative to the transmitter), is given by:

$$R_1' = D\tan(f_1) - S_1 \tag{3.5}$$

$R_2'$, the distance from mid-swath to the near edge of the cone of energy scattered from the far end of the swath (relative to the transmitter), is given by:

$$R_2^{'} = D\tan(f_2) + S_2 \tag{3.6}$$

The receiver aperture, $R_M$, which will receive energy from both $S_1$ and $S_2$ is given by:

$$R_M = R_2^{'} - R_1^{'} = S_1 + S_2 + D(\tan(f_2) - \tan(f_1)) \tag{3.7}$$

We can perform a quick verification of (3.7) by setting $b$ to 0. In this case, $R_M$ should be twice the swath width or $2(S_1 + S_2)$.

$$\begin{aligned} R_M &= S_1 + S_2 + D\left\{\tan\left[\operatorname{atan}\left(\frac{T + S_2}{D}\right)\right] - \tan\left[\operatorname{atan}\left(\frac{T - S_1}{D}\right)\right]\right\} \\ &= S_1 + S_2 + D\left\{\frac{T + S_2}{D} - \frac{T - S_1}{D}\right\} = 2(S_1 + S_2) \end{aligned} \tag{3.8}$$

This receiver aperture is big enough to receive energy from the two endpoints, but does not include the additional length on each end of the aperture that will be required to *resolve* the two end points. Therefore, we define the minimum receiver aperture, $R$, that provides a cross-track resolution of $s_x$ for all points along the swath, to be

$$R = R_1 + R_M + R_2 \tag{3.9}$$

where $R_1$ is the minimum synthetic aperture size required to resolve $S_1$ and $R_2$ is the minimum synthetic aperture size required to resolve $S_2$. To determine $R_1$ and $R_2$, we will use the plane wave approximation and assume that a linear equally spaced array is used. In this report, we define the ability to resolve targets, such that, an interfering target, $s_x$ meters away from the desired target, will be in the first null when a uniform amplitude taper is used on the receive antenna elements (boxcar window) and the phases are set to maximize the desired target's return.

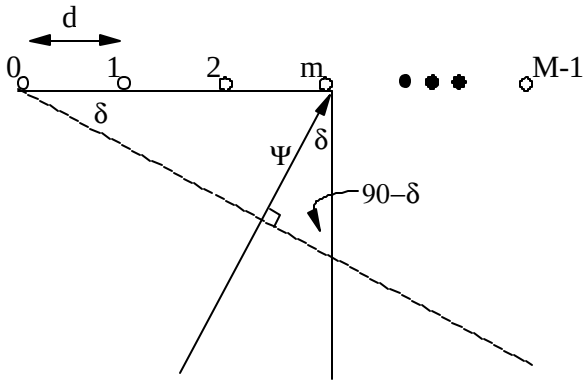


*Figure 3-8: Linear equally spaced array with M elements and a plane wave incident at d radians from broadside.*

Figure 3-8 shows a linear equally spaced antenna array with M elements. If the plane wave is incident on the array at an angle of δ from broadside, the path difference between element 0 and element m will be given by:

$$\Psi_m = dm\sin(d) \tag{3.10}$$

We set the element zero as the reference. In other words, element zero sees the signal as $s_0(t)$ and all the other elements see $s_0(t)$ with a delay that depends on their spatial position and the angle of the incoming plane wave. By converting the path length difference to a time difference, the received signal at each antenna element is given by:

$$s_m(t) = s_0\left(t - \frac{\Psi_m}{v}\right) = s_0\left(t - \frac{dm\sin(d)}{v}\right) = s_0\left(t - \frac{dmn\sin(d)}{c}\right) \tag{3.11}$$

Where $n$ is the speed of light in the medium, $n$ is the index of refraction of the medium, and c is the speed of light in free space.

If we assume that the received signal $s_0(t)$ is a complex sinusoid with a magnitude of $A$ and a phase of $g$, then we have:

$$s_m(t) = A\exp\left(jwt + jg - \frac{jdm?\sin(d)}{v}\right) \tag{3.12}$$

If we sum the signal at each of the antenna elements together we get:

$$s(t) = \sum_m s_m(t) = \sum_m A\exp(jwt + jg)\exp\left(\frac{-jdm? \sin(d)}{v}\right) \tag{3.13}$$

The time dependence of the sinusoid does not depend on the summation variable k and can be pulled out of the summation.

$$s(t) = A\exp(jwt + jg)\sum_m \exp\left(\frac{-dm? \sin(d)}{v}\right) \tag{3.14}$$

Since $?$ is related to $v$ by $\frac{?}{v} = \frac{2p}{?}$, where $l$ is the wavelength in the medium we can write

$$s(t) = A\exp(jwt + jg)\sum_m \exp\left(\frac{-j2pdm\sin(d)}{?}\right) \tag{3.15}$$

We can rewrite (3.15) as a discrete Fourier transform with $m$ being the summation variable and $\frac{d\sin(d)}{?}$ being the normalized frequency variable. If we want to prevent aliasing[6], the maximum normalized frequency should be strictly less than 0.5 and strictly more than –0.5 (the angular frequency would be $0.5 \cdot 2p = p$ and $-0.5 \cdot 2p = -p$ respectively). Since $\sin(d)$ can have a maximum value of 1 and a minimum value of -1, this means that d must be strictly less than $\frac{?}{2}$. For $d = \frac{l}{2}$, this gives[7]:

---

[6] If two values of $\delta$ map to the same relative phase $\left[\frac{2pd\sin(d)}{l} \text{ modulo } 2p\right]$, then the two angles will be ambiguous because they will have the same value because $\exp(jt) = \exp(jt + j2p)$.

[7] Choosing $d = \frac{l}{2}$ causes $d = \frac{p}{2}$ and $d = -\frac{p}{2}$ to look exactly the same, this is okay in our case because we are not receiving signals from both of these directions.

$$s(t) = A\exp(jwt + jg)\sum_{m}\exp\left(-j2p\frac{\sin(d)}{2}m\right) \tag{3.16}$$

Evaluating (3.16) as a fast Fourier transform (FFT) returns an impulse function weighted by the time dependent constant in front. Taking the discrete Fourier transform shows a periodic sinc-like function with zeros at each of the fast Fourier transform's samples as shown in Figure 3-9.

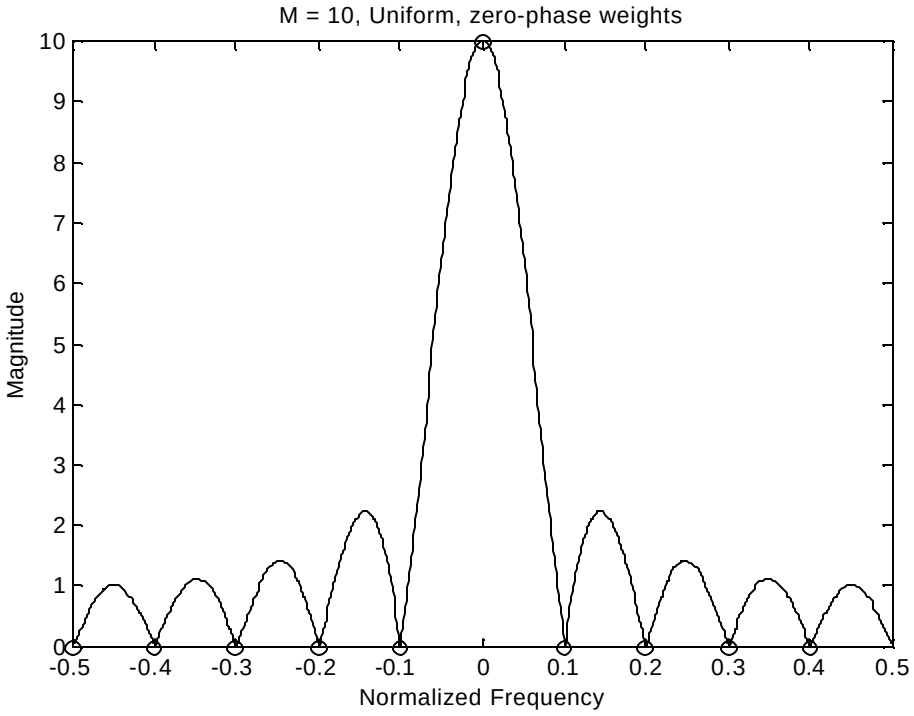


*Figure 3-9: Output of the linear equally spaced array with 10 elements versus normalized frequency, $\frac{\sin(d)}{2}$. The nulls at ±0.5 are due to aliasing and represent one null.*

Therefore, when $\frac{\sin(d)}{2}$ is zero (i.e. broadside plane wave with $\delta$ = 0), the output is maximized and there are M-1 equally spaced nulls (the zeros of the FFT). If each of the antenna element outputs were independently time delayed by $t_m$ we would have:

$$s_k(t) = s_0\left(t - \frac{dm\sin(d_1)}{v} - t_m\right) \tag{3.17}$$

If we set $t_m = \frac{-dm\sin(d_2)}{v}$, (3.17) becomes:

$$s_m(t) = s_0\left(t - \frac{dm\sin(d_1)}{v} + \frac{dm\sin(d_2)}{v}\right) \tag{3.18}$$

Which, when we use complex sinusoidal signals and sum the antenna elements becomes:

$$s(t) = A\exp(jwt + jg)\sum_m \exp\left(j2p\frac{\sin(d_2)}{2}m\right)\exp\left(-j2p\frac{\sin(d_1)}{2}m\right) \tag{3.19}$$

When the FFT is taken, the result is a frequency shifted impulse function because $\exp\left(j2p\frac{\sin(d_2)}{2}m\right)$ is the frequency-shift property. Therefore, the DTFT is the sinc-like function shifted in frequency, but there are still M-1 equally spaced nulls since it is the same function as before only shifted as shown in Figure 3-10. When the incident plane wave has $d_1 = d_2$, the output s(t) is maximized. This is not formally proven here, but can be proven by showing that when $d_1 = d_2$, s(t) is the magnitude squared of each of the components and we can use Schwartz's Inequality to prove that this is the maximum. The uniqueness of the maximum depends on whether or not the system is aliased or not. As a side note, this reasoning is very similar to the reasoning used to prove that the matched filter maximizes signal to noise ratio since this result is the matched filter.

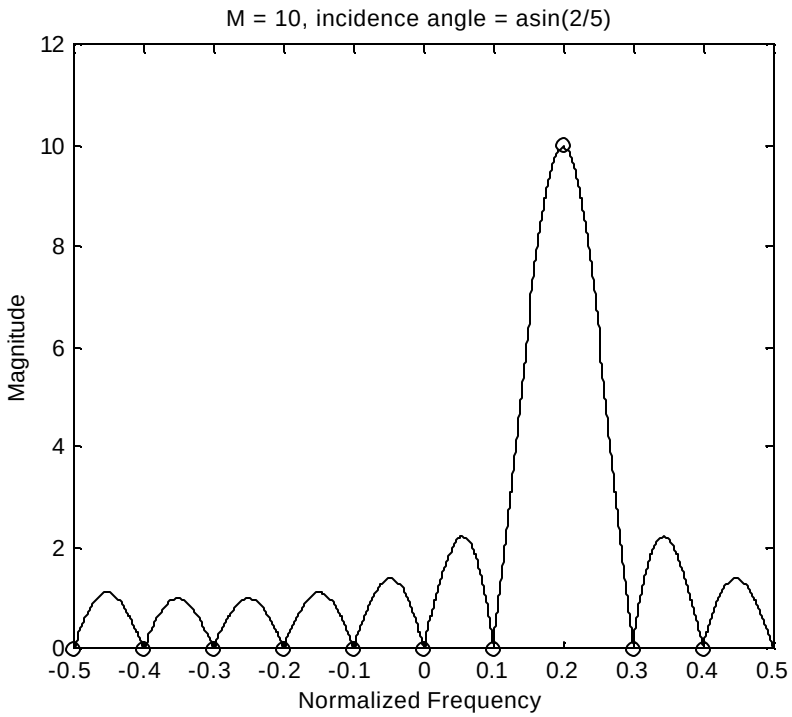


*Figure 3-10: Output of a linear equally spaced array with 10 elements and phase delays added to each input. The phase delays are equal to:*

$$t_m = -pm\sin(\text{asin}(2/5)) = -m2p/5$$

Before we can use this result, the frequency axis $\frac{\sin(d)}{2}$ must be converted back into incidence angle $d$. The M-1 nulls are spaced $\frac{2p}{M}$ radians apart (at the FFT samples of the DTFT as shown in Figure 3-10). Using our definition for resolution, we can resolve two normalized frequencies as long as they are spaced $\frac{2p}{M}$ radians apart. If we know the two incidence angles we wish to resolve, say $\delta$ and $\varphi$, then these two angles, when translated must be separated by $\frac{2p}{M}$ radians.

$$2p\left|\frac{\sin(d)}{2} - \frac{\sin(f)}{2}\right| = \frac{2p}{M} \tag{3.20}$$

If (3.20) is satisfied, $|d-f|$ is the difference in incidence angle between the maximum and its closest null. Since we are given $s_x$, we can determine the two incidence angles as shown in Figure 3-11.

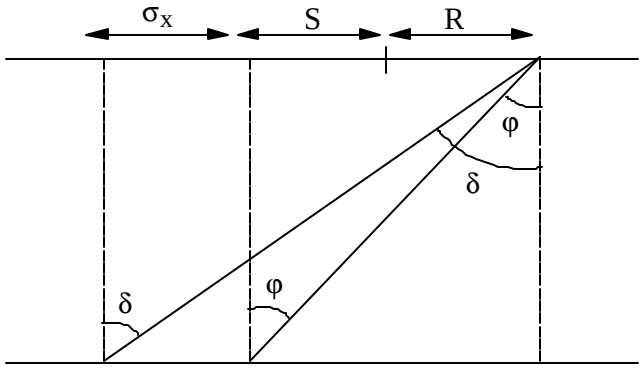


*Figure 3-11: Geometry for determining the incidence angles for the target and interferer.*

For the two end-points, the corresponding incidence angle from the interferers is:

$$d_1 = \text{atan}\left(\frac{s_x + R_1 + S_1}{D}\right) \tag{3.21}$$

And

$$d_2 = \text{atan}\left(\frac{s_x + R_2 - S_2}{D}\right) \tag{3.22}$$

Next, we find the number of elements our aperture needs. This can be found by solving (3.20) for M. Since we would like M to be an integer, we use the ceiling function as follows:

$$\text{M} = \left\lceil \left| \frac{\sin(d)}{2} - \frac{\sin(f)}{2} \right|^{-1} \right\rceil \tag{3.23}$$

Since the antenna spacing is $\frac{?}{2}$, this gives a minimum aperture size of $(M-1)\frac{?}{2}$ or

$$R_1 = \left( \left| \frac{\sin(d_1)}{2} - \frac{\sin(f_1)}{2} \right|^{-1} - 1 \right) \frac{?}{2} \tag{3.24}$$

$$R_2 = \left( \left| \frac{\sin(d_2)}{2} - \frac{\sin(f_2)}{2} \right|^{-1} - 1 \right) \frac{?}{2} \tag{3.25}$$

We now have all of the components we need to find the minimum receiver aperture, $R$, which will obtain a cross-track resolution of $s_x$ over a swath width of $S_1 + S_2$.

For transmitter positions close to the origin, the minimum receiver aperture is dominated by $R_M$. As the transmitter is moved away from the origin, $R_M$ decreases as shown in Figure 3-4 above. Eventually, $R_M$ goes to zero and the minimum receiver aperture is dominated by $R_1$ and $R_2$. $R_M$ will continue to decrease. When $R_M$ assumes a negative value, this effectively represents the overlap of the regions illuminated by targets $S_1$ and $S_2$. This overlap helps slow the corresponding increase in the synthetic apertures represented by $R_1$ and $R_2$. Eventually, when the overlapping region is larger than $R_1$ or $R_2$, the two synthetic apertures completely overlap and the larger of the two synthetic apertures determines the minimum receiver aperture. At this point, $R_1'$ and $R_2'$ are not equal to the values given in (3.24) and (3.25). This is because the ideal receiver position for the target *closest* to the transmitter is constrained by the target *furthest* away from the transmitter as shown in Figure 3-12. The synthetic aperture will always be largest for the target closest to the transmitter because, for completely overlapping apertures, this implies that the target is the farthest from the receiver (farthest away implies a larger incidence angle $\delta$). This means that the minimum receiver aperture size is determined solely by the synthetic aperture size required to resolve the target closest to the transmitter. The results in the next section account for this condition.

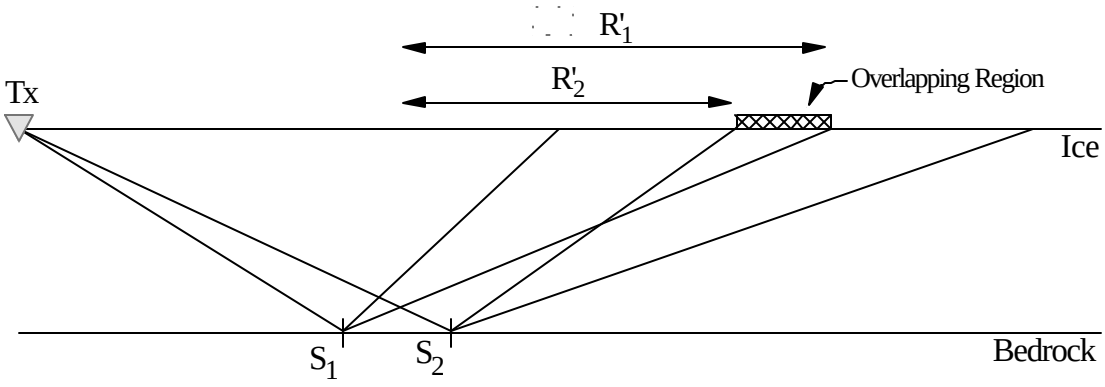


*Figure 3-12: When the transmitter is placed far enough away from the swath and the maximum forward-scatter angle is large enough, the two regions illuminated by the end-points of the swath overlap.*

### 3.2.3 RESULTS

Figure 3-15 through Figure 3-18 plot the minimum receiver aperture, R, versus transmitter position for an ice thickness of 3000 meters. The absolute minimum is circled and indicates the best possible transmitter position for minimizing the receiver aperture. In all cases, $s_x = 100$ m, $S_1 = -500$ m, $S_2 = 500$ m, the carrier frequency is 150 MHz, and the dielectric profile derived from the GRIP[8] ice core is used. The carrier frequency and index of refraction are only needed to find the wavelength. Simulations using CAD software were performed which show that the maximum launch angle into firn[9] is approximately 65° [28]. This maximum launch angle was determined by dividing the 3 dB beamwidth of the antenna in the firn by two. The dashed vertical lines in the figures represent the point where the maximum launch angle has been reached. The lines indicate that any absolute transmitter position beyond this line will not work unless a greater launch angle can be achieved; hence we are restricted to the transmitter positions between these two lines. If there are no dashed vertical lines, then the launch angle never reaches 65° for the transmitter positions shown. For reference, the largest launch angle corresponding to each transmit position is plotted on the right y-axis.

---

[8] GReenland Ice-core Project organized by the European Science Foundation (ESF).

[9] The firn is the upper layer of the ice sheet, which is packed snow rather than pure ice. It was modeled as a lossless dielectric with $e_r \approx 1.6$.

A ray-tracing model accounts for refraction through the ice by approximating the continuous dielectric profile as a set of thin discrete layers [27]. The derivations above assumed a constant dielectric, so a method for mapping is needed between launch angle, bedrock incident angle, and the x-offset of the ray corresponding to these angles (Figure 3-13). The ice density is directly related to depth, which is why the rays in Figure 3-13 steadily bend downward the further into the ice they travel (the amount of change in the curves has been exaggerated for illustration).

The ray-tracing model is used to create a conversion table between the three parameters. The ray-tracing model takes the dielectric profile of the ice versus depth (from the GRIP ice core) and the launch angle and then computes the two other parameters. This is done for each of the possible launch angles and a table is formed that allows mapping between each of the parameters. The effect of these mappings in the calculations above is to replace trigonometric expressions with the appropriate mapping since the ray from the transmitter/receiver to the target of interest (or vice versa) is no longer a straight line.

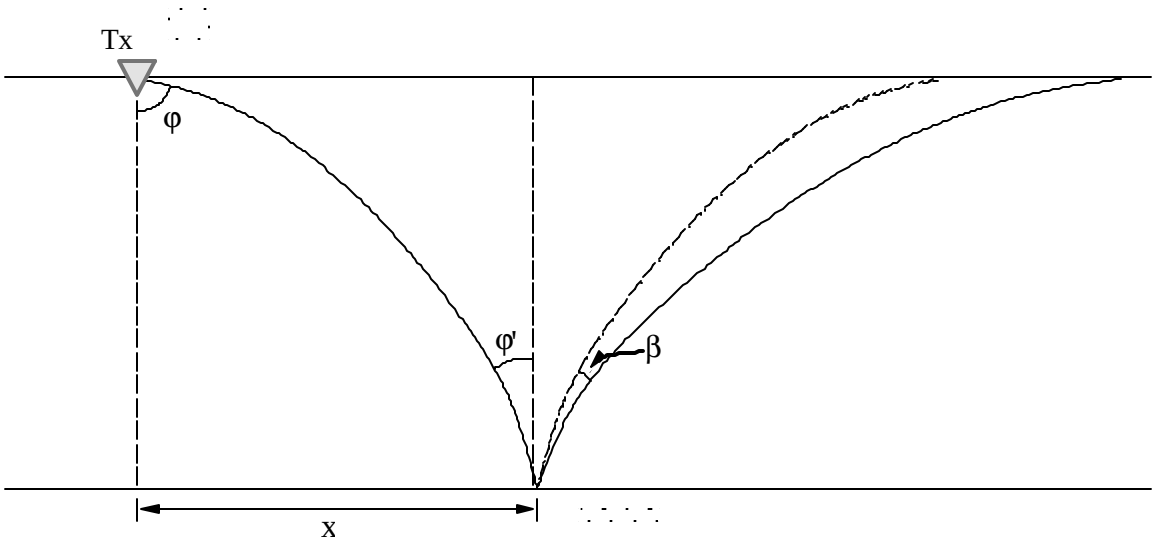


*Figure 3-13: Example of the relationship between launch angle, $f$, bedrock incident angle, $f'$, and an arbitrary x-offset, x. The forward-scatter angle, $b$, is shown for illustrative purposes; here the dashed-curved line is the specular response which $b$ is measured from.*

Since one of the reasons for choosing the bistatic mode of operation was to decrease the minimum receiver aperture size, a comparison to monostatic mode is made in each of the figures. The monostatic mode in this case is not the standard side-looking radar setup since we are assuming that the surface is too smooth for side-looking radar. The monostatic mode instead builds a cross-track synthetic aperture similar to the receiver in the bistatic mode as shown in Figure 3-14. Since the transmitter and receiver are collocated in monostatic mode, it is assumed that the middle of the synthetic aperture is aligned with the middle of the swath. The minimum is shown as a horizontal dashed line in the figures below.

The minimum size of the monostatic aperture is controlled by the maximum backscatter angle, $r$, in much the same way that the bistatic aperture is controlled by the maximum forward-scatter angle. The only part of the synthetic aperture that affects the resolution of the end-points of the swath is the part that lies within the backscatter from the end-points (region demarcated by $R_1$ and $R_2$). Therefore, the monostatic synthetic aperture $R_{Mono}$ must be enough larger than $R_M$ such that $R_1$ and $R_2$ are large enough to resolve the end-points to within $s_x$. Also because the receiver and transmitter move together, a true synthetic aperture, like the monostatic case described here, achieves twice the angular resolution of the synthetic beam-forming used in the bistatic case for the same sized aperture.

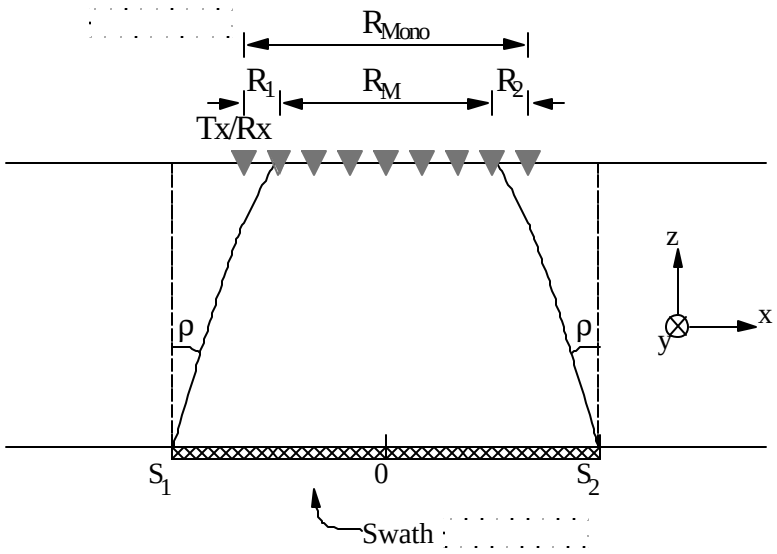


*Figure 3-14: Illustration of monostatic synthetic aperture.*

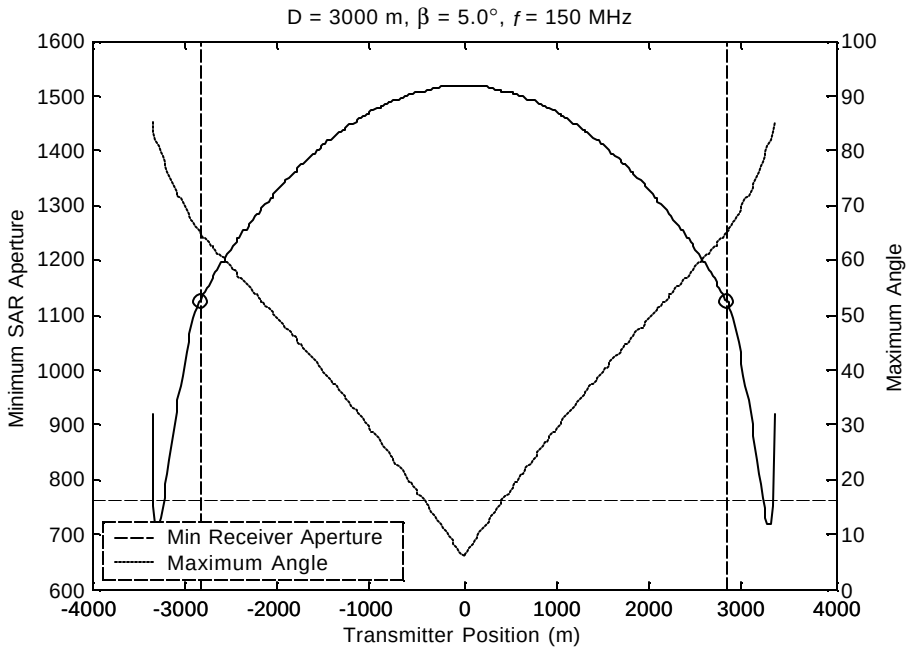


*Figure 3-15: Minimum receiver aperture size versus transmitter position for a maximum forward-scatter angle, $\beta$, of 5° and ice thickness of 3000 m.*

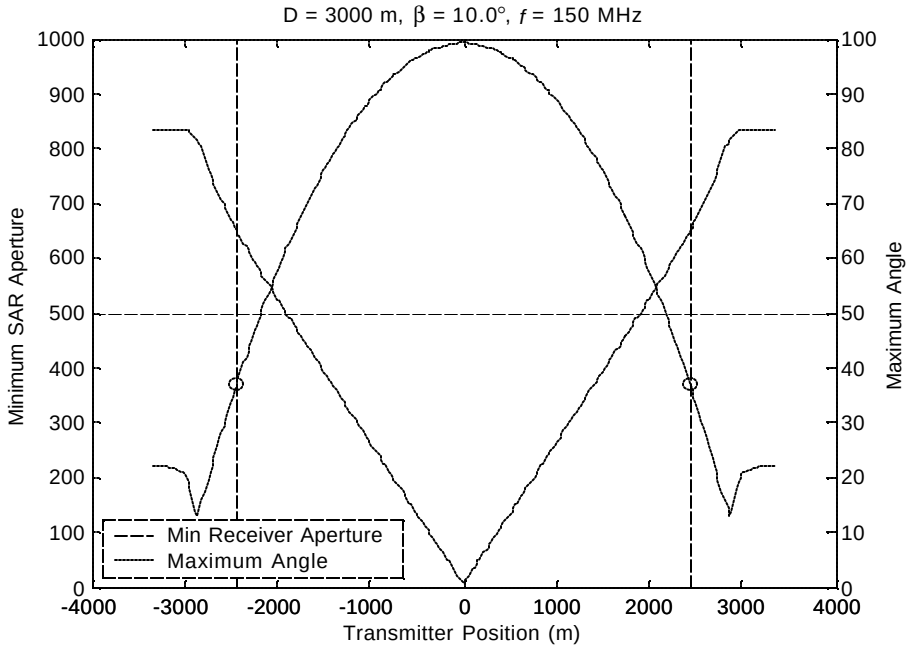


*Figure 3-16: Minimum receiver aperture size versus transmitter position for a maximum forward-scatter angle, $\beta$, of 10° and ice thickness of 3000 m.*

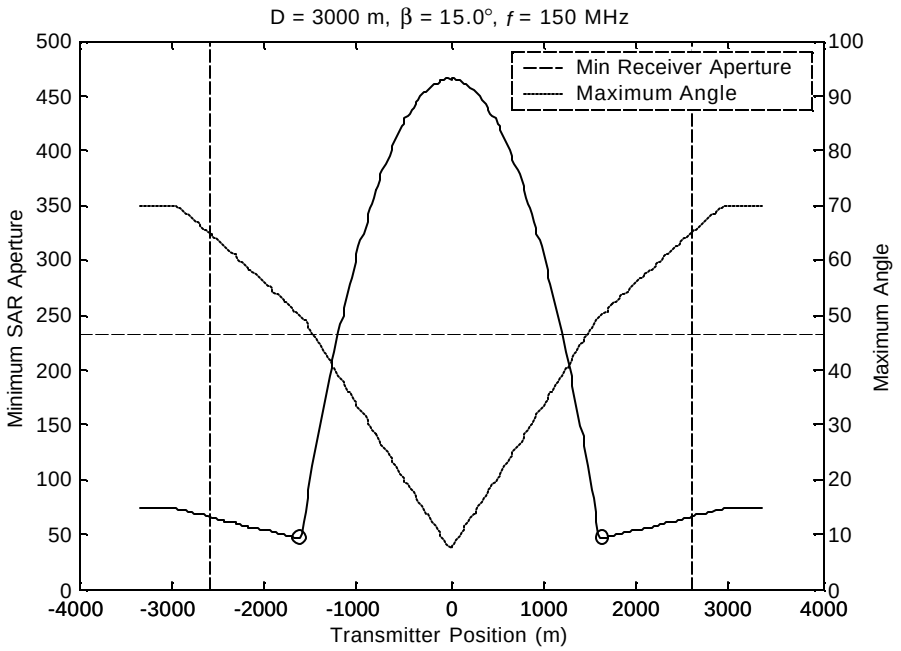


*Figure 3-17: Minimum receiver aperture size versus transmitter position for a maximum forward-scatter angle, $\beta$, of 15° and ice thickness of 3000 m.*

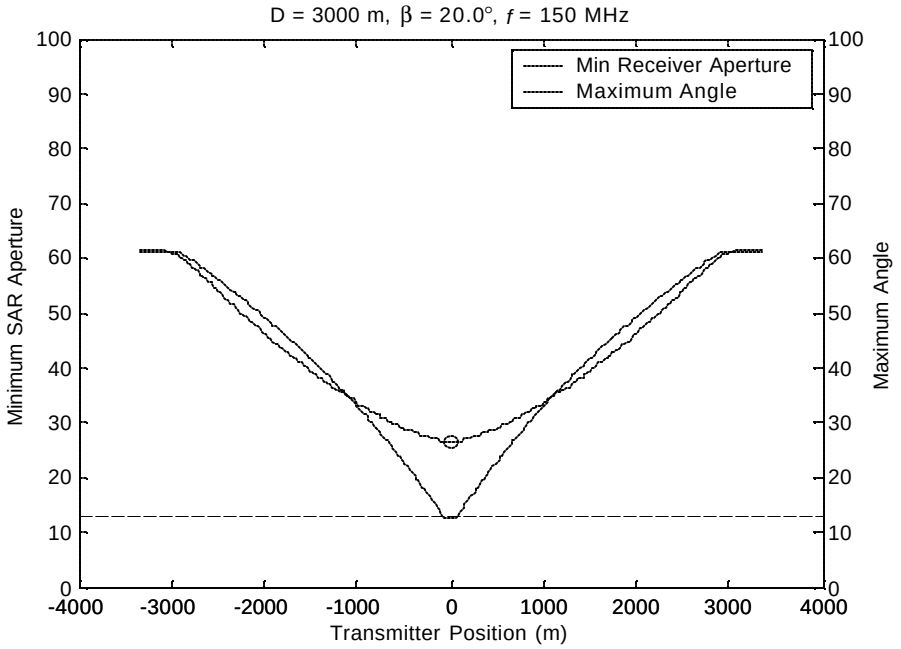


*Figure 3-18: Minimum receiver aperture size versus transmitter position for a maximum forward-scatter angle, $\beta$, of 20° and ice thickness of 3000 m.*

Figure 3-15 through Figure 3-18 show how sensitive the ideal transmitter position is to the maximum forward scatter angle. The ideal transmitter position is also a function of frequency and ice thickness as is shown below. However, it is relatively insensitive to frequency and the ice thickness will not change quickly so these dependencies are not a significant problem. On the other hand, sensitivity to maximum forward scatter angle is a large problem because we expect the regions being imaged to contain different types of scattering surfaces. Indeed, scattering is one of the parameters being measured. This means that a compromise between optimal transmitter positions will have to be made. Fortunately, in most cases, the transmitter position can be placed beyond the ideal transmitter position without a substantial penalty in minimum receiver aperture size. One of the advantages of the monostatic mode – this is the mode described above and is not side-looking – is that the ideal center of the aperture is always aligned with the center of the swath since the ice is relatively flat. Only the length of the aperture changes with backscatter, frequency response or depth of ice and this can be determined as the aperture is formed.

Table 3-1 through Table 3-3 summarize the results for 1000 m, 2000 m, 3000 m, 4000 m, and 5000 m thick ice and for maximum forward-scatter angles of 5, 10, 15 and 20 degrees. Table 3-1 is for 60 MHz, Table 3-2 is for 150 MHz, and Table 3-3 is for 350 MHz. The 1000, 2000, 4000, and 5000 m ice profiles were adapted from the 3000 m GRIP profile by extending or shrinking the cold, dense inner layers (above the geothermally heated layer next to the bedrock and below the firn). Figure 3-19 through Figure 3-23 illustrate the results from the tables at maximum forward scatter angles ranging from 0 to 30 degrees with 1-degree steps; for the monostatic case this means that the maximum backscatter angle ranges from 0 to 15 degrees in 0.5 degree steps.

*Table 3-1: The minimum receiver aperture for bistatic synthetic beam-forming and monostatic SAR when f = 60 MHz.*

| Ice Thickness (m) | Max. forward-scatter angle (deg) | Tx Position (m) | Min. Receiver Aperture (m) | Min. Monostatic Aperture (m) |
|---|---|---|---|---|
| 1000 | 5 | 641 | 1790 | 932 |
| 1000 | 10 | 1150 | 974 | 843 |
| 1000 | 15 | 1031 | 829 | 754 |
| 1000 | 20 | 923 | 700 | 667 |
| 2000 | 5 | 1741 | 1560 | 867 |
| 2000 | 10 | 1792 | 921 | 691 |
| 2000 | 15 | 1556 | 500 | 513 |
| 2000 | 20 | 1380 | 111 | 334 |
| 3000 | 5 | 2831 | 1323 | 799 |
| 3000 | 10 | 2435 | 538 | 535 |
| 3000 | 15 | 1710 | 121 | 273 |
| 3000 | 20 | 0 | 66 | 32 |
| 4000 | 5 | 3605 | 1144 | 734 |
| 4000 | 10 | 2910 | 190 | 383 |
| 4000 | 15 | 0 | 86 | 42 |
| 4000 | 20 | 0 | 86 | 42 |
| 5000 | 5 | 4378 | 954 | 667 |
| 5000 | 10 | 2350 | 159 | 230 |
| 5000 | 15 | 0 | 107 | 53 |
| 5000 | 20 | 0 | 107 | 53 |

*Table 3-2: The minimum receiver aperture for bistatic synthetic beam-forming and monostatic SAR when f = 150 MHz.*

| Ice Thickness (m) | Max. forward-scatter angle (deg) | Tx Position (m) | Min. Receiver Aperture (m) | Min. Monostatic Aperture (m) |
|---|---|---|---|---|
| 1000 | 5 | 641 | 1740 | 920 |
| 1000 | 10 | 1150 | 909 | 831 |
| 1000 | 15 | 1031 | 769 | 742 |
| 1000 | 20 | 923 | 645 | 653 |
| 2000 | 5 | 1741 | 1442 | 842 |
| 2000 | 10 | 1792 | 800 | 665 |
| 2000 | 15 | 1556 | 392 | 488 |
| 2000 | 20 | 1330 | 43 | 309 |
| 3000 | 5 | 2831 | 1125 | 762 |
| 3000 | 10 | 2435 | 371 | 498 |
| 3000 | 15 | 1610 | 47 | 234 |
| 3000 | 20 | 0 | 26 | 13 |
| 4000 | 5 | 3605 | 895 | 684 |
| 4000 | 10 | 2730 | 72 | 332 |
| 4000 | 15 | 0 | 34 | 17 |
| 4000 | 20 | 0 | 34 | 17 |
| 5000 | 5 | 4378 | 654 | 604 |
| 5000 | 10 | 2100 | 60 | 166 |
| 5000 | 15 | 0 | 43 | 21 |
| 5000 | 20 | 0 | 43 | 21 |

*Table 3-3: The minimum receiver aperture for bistatic synthetic beam-forming and monostatic SAR when f = 350 MHz.*

| Ice Thickness (m) | Max. forward-scatter angle (deg) | Tx Position (m) | Min. Receiver Aperture (m) | Min. Monostatic Aperture (m) |
|---|---|---|---|---|
| 1000 | 5 | 641 | 1721 | 915 |
| 1000 | 10 | 1150 | 885 | 827 |
| 1000 | 15 | 1031 | 746 | 738 |
| 1000 | 20 | 923 | 624 | 648 |
| 2000 | 5 | 1741 | 1397 | 832 |
| 2000 | 10 | 1792 | 753 | 656 |
| 2000 | 15 | 1556 | 351 | 478 |
| 2000 | 20 | 1330 | 19 | 299 |
| 3000 | 5 | 2831 | 1049 | 748 |
| 3000 | 10 | 2435 | 307 | 484 |
| 3000 | 15 | 1580 | 20 | 219 |
| 3000 | 20 | 0 | 11 | 6 |
| 4000 | 5 | 3605 | 800 | 664 |
| 4000 | 10 | 2670 | 30 | 313 |
| 4000 | 15 | 0 | 15 | 7 |
| 4000 | 20 | 0 | 15 | 7 |
| 5000 | 5 | 4378 | 539 | 581 |
| 5000 | 10 | 2010 | 25 | 142 |
| 5000 | 15 | 0 | 18 | 9 |
| 5000 | 20 | 0 | 18 | 9 |

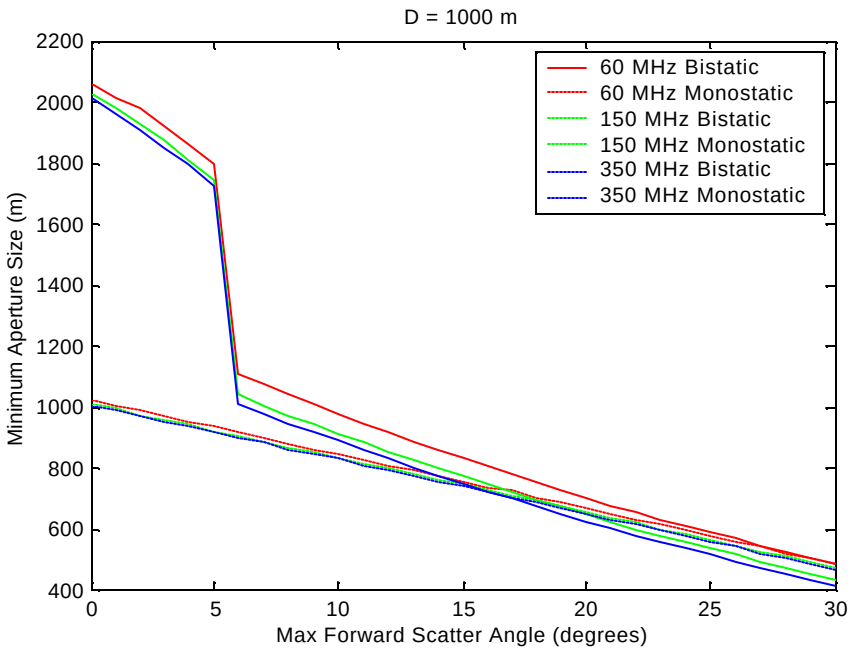


*Figure 3-19: Minimum receiver aperture size versus maximum forward-scatter angle with an ice thickness of 1000 (m).*

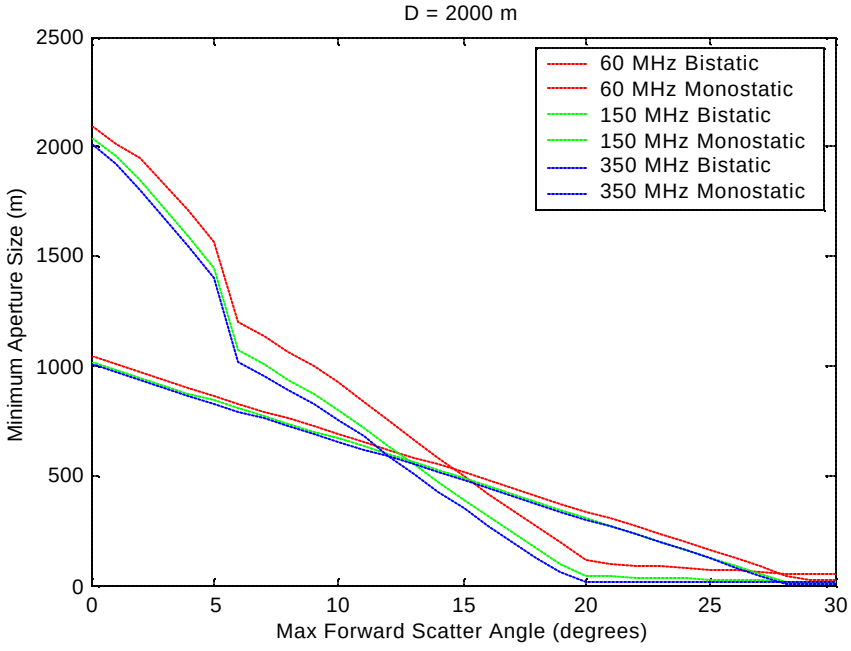


*Figure 3-20: Minimum receiver aperture size versus maximum forward-scatter angle with an ice thickness of 2000 (m).*

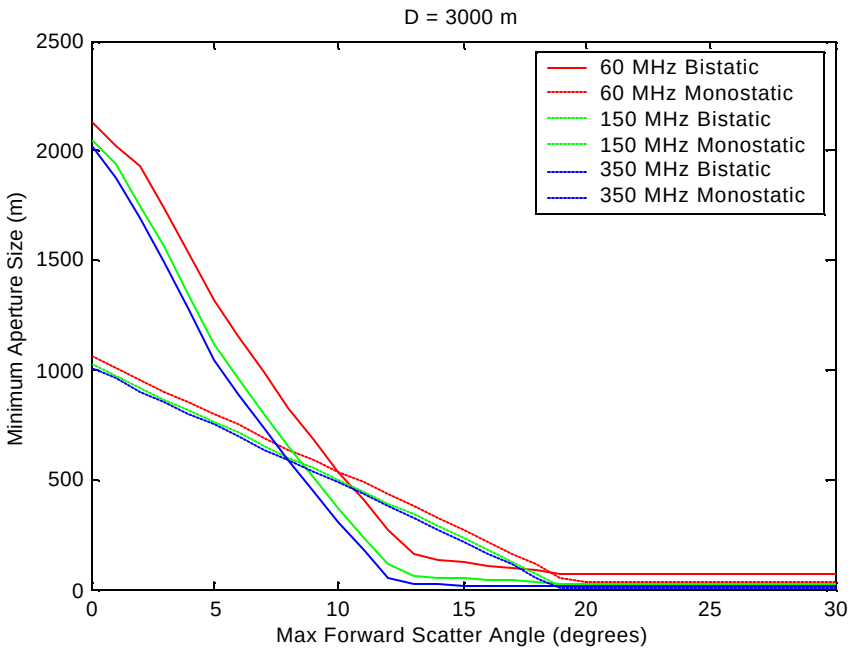


*Figure 3-21: Minimum receiver aperture size versus maximum forward-scatter angle with an ice thickness of 3000 (m).*

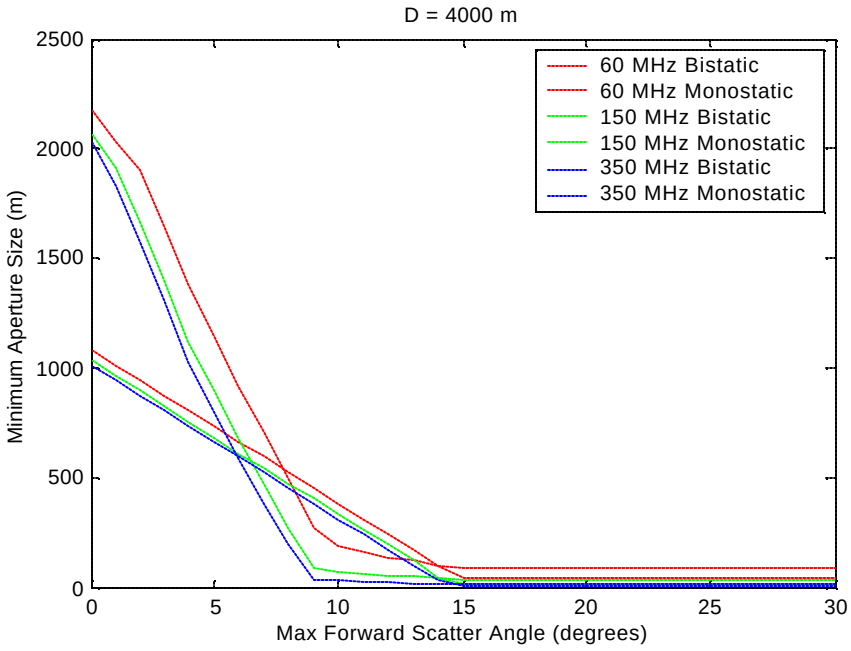


*Figure 3-22: Minimum receiver aperture size versus maximum forward-scatter angle with an ice thickness of 4000 (m).*

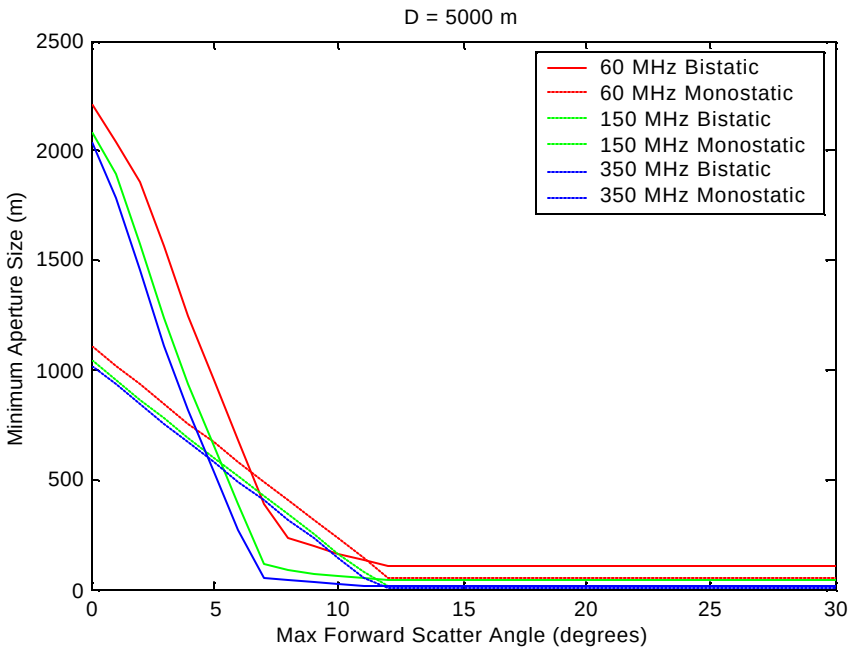


*Figure 3-23: Minimum receiver aperture size versus maximum forward-scatter angle with an ice thickness of 5000 (m).*

According to [19], the maximum backscatter measured from four different locations in Greenland varied between 5 and 10 degrees. This corresponds to a maximum forward scattering of 10 to 20 degrees based on the assumption that $b = 2r$. In this region, the bistatic mode usually performs the same as the monostatic mode (doing better for certain maximum scattering angles and worse at other maximum scattering angles). The lower the frequency, the worse bistatic mode performs since the apertures must be twice the size of the monostatic apertures (since only the receiver moves in bistatic mode). If the ice is very smooth ( $b < 10°$ ) or rough ( $b > 20°$ ) then the monostatic mode is superior.

Despite the complexity of the bistatic sensor geometry, the bistatic mode provides information about the forward scattering that any kind of monostatic configuration cannot provide. The monostatic side-looking mode also provides information that the bistatic mode cannot provide. Therefore, simultaneous operation of the two modes may actually be the ideal situation.

## 3.3 REAL APERTURE

As mentioned in the chapter one, the bistatic mode requires spatial sampling to improve cross-track resolution and is therefore considerably slower than monostatic mode. One possibility is to use an antenna array on the transmitter in the along-track direction as shown in Figure 3-24 (the individual antenna element is a broadband bowtie antenna). By using an array in the along-track direction, the energy transmitted to the other vehicle will be focused toward that vehicle according to the length of the array. Because the energy is focused, the along-track sampling can be reduced, hence requiring fewer cross-track transects by the other vehicle. The traverse speed increase by using an array depends on the length of the real aperture. Without an array, the along-track sampling must be done every half wavelength. If the array is M half-wavelengths long, the time to traverse is improved by M. On the other hand, practical considerations will limit how large the real aperture may be.

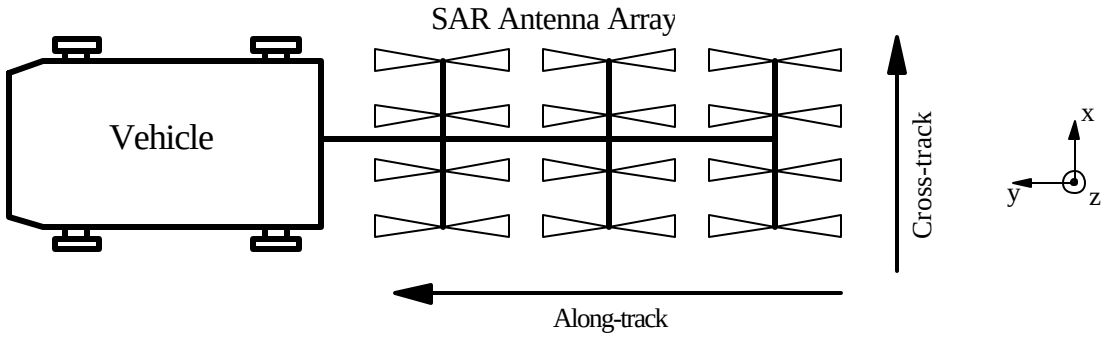


*Figure 3-24: Position of the antenna array on the transmitter vehicle. The antenna array in the along-track direction (3-elements in length as depicted here) makes it so that less cross-track transects need to be made by the other vehicle. The cross-track array is necessary for monostatic mode and is shown here with 4 elements for completeness (i.e. it is not necessary for the calculations in this section).*

In the space domain, this array looks like a rectangle function (the large antenna with half-wavelength spacing) convolved with an impulse train (the synthetic aperture). Therefore, the beam pattern of the larger real antenna combined with the sparsely sampled synthetic aperture is the multiplication of the two individual beam

patterns. This product/convolution relationship mirrors the time and frequency domain relationship.

To demonstrate this, consider a ten-element linear equally spaced (LES) array dragged behind the transmitter and aligned in the along-track direction. The sampling is assumed to be sufficient to remove ambiguities (i.e. half-wavelength). The total length of the LES array is then five wavelengths. We treat this length-10 discrete-space sequence similar to a length-10 discrete-time sequence. To determine the spatial frequency characteristics of the antenna, we take the fast Fourier transform (FFT) of the discrete-space sequence. The result is in the $k_x$ or x-spatial frequency domain. If we limit ourselves to just one frequency, we can determine all the possible spatial frequencies, $\vec{k}$. The spatial frequency components must satisfy this equation:

$$\|k\|_2 = \sqrt{k_x^2 + k_y^2 + k_z^2} = \frac{2p}{l} \tag{3.26}$$

Since we are mainly interested about the effects on the x-axis resolution (along-track resolution), we can ignore y-propagating waves (cross-track). Doing this, changes the constraint equation to

$$\|k\|_2 = \sqrt{k_x^2 + k_z^2} = \frac{2p}{l} \tag{3.27}$$

This essentially means that we are looking only at plane waves that are not propagating in the y-direction, i.e. $k_y = 0$.

Since $k_x$ is known from the FFT and the wavelength is given, the value of $k_z$ can be determined as:

$$k_z = \pm\sqrt{\left(\frac{2p}{l}\right)^2 - k_x^2} \tag{3.28}$$

The ± accounts for the fact that the LES array has an ambiguity between waves propagating from the back and from the front. Both wave fronts will cause the same

phase signature across the LES array. For the purposes of illustrating the convolution, a wave propagating from the front is assumed (choose the +).

Since each spatial frequency component is known, the direction of arrival, $\delta$, can be determined as

$$d = \tan^{-1}\left(\frac{k_x}{k_z}\right) = \tan^{-1}\left(\frac{k_x}{\sqrt{\left(\frac{2p}{l}\right)^2 - k_x^2}}\right) \tag{3.29}$$

The result of the direction of arrival versus the FFT is shown in Figure 3-25.

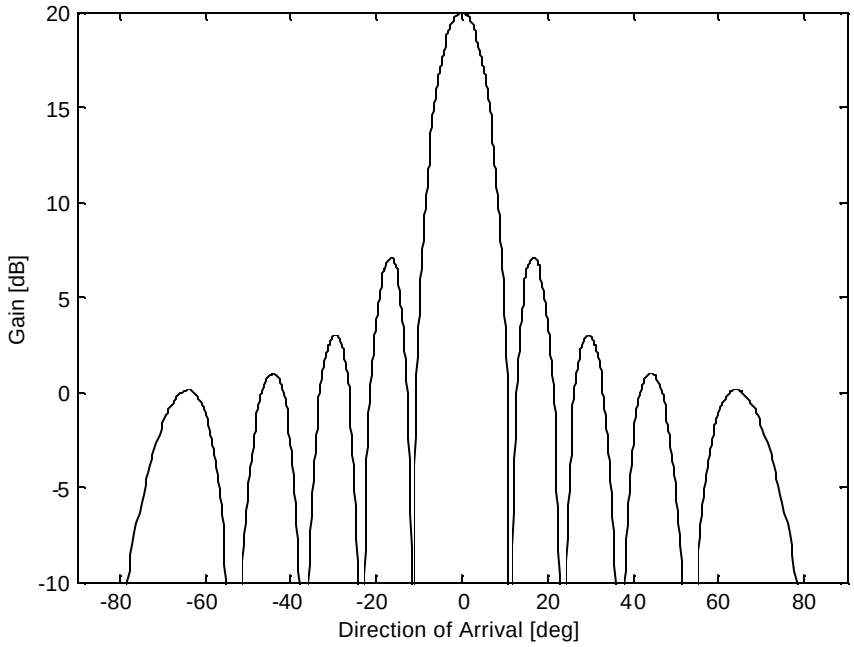


*Figure 3-25: Array gain for ideal 10-element linear equally spaced **real** array with half wavelength spatial sampling.*

This pattern has a single main lobe because it is not undersampled, but the main lobe is over 20 degrees wide, which is too broad for our application. However, we have not included the effects of the synthetic aperture yet. To show this effect, we take the FFT of a length five, five-wavelength spaced LES. The length of the

aperture is 20 wavelengths, but it is undersampled. The results are shown in Figure 3-26. The grating lobes are due to the undersampling. To determine the combined array gain, the two FFT sequences are multiplied together. To avoid periodic convolution, each of the arrays were zero-padded to a length of 1000 (half-wavelength spacings). This also has the added benefit of creating an image more closely resembling the DTFT, which is the actual beam-pattern representation. This is shown in Figure 3-27.

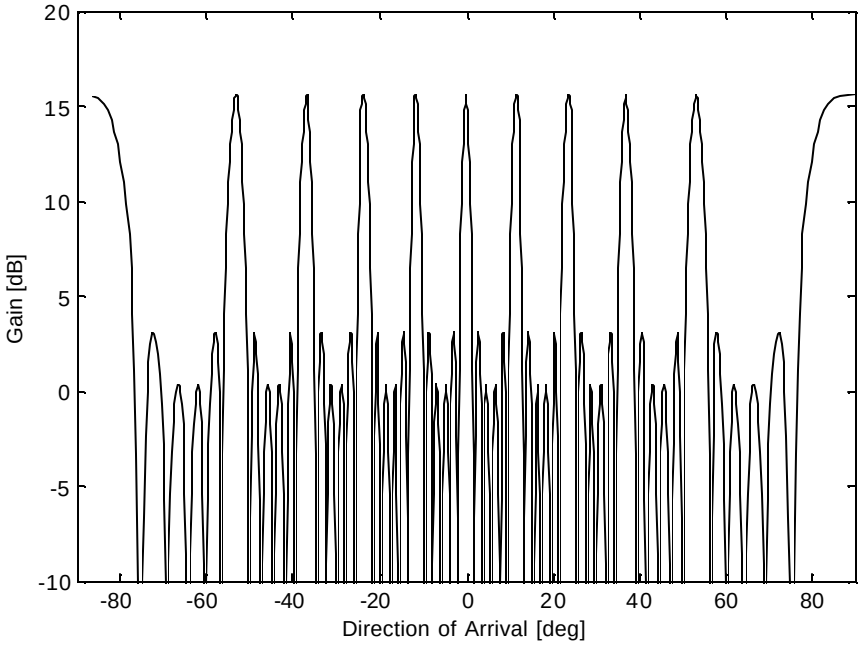


*Figure 3-26: Array gain for 5-element linear equally spaced **synthetic** array with five-wavelength sampling. Note the 11 grating lobes.*

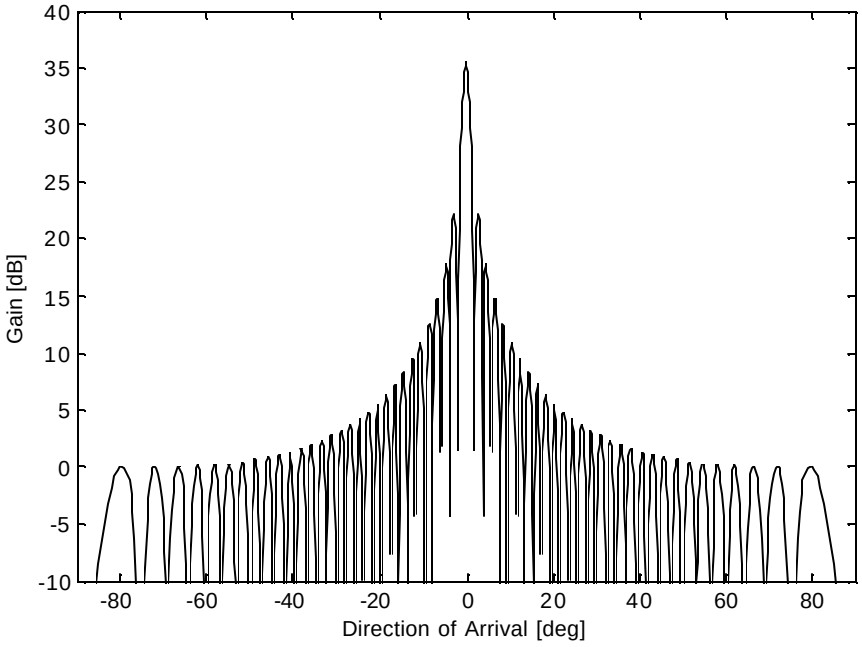


*Figure 3-27: Combined array gain for the two arrays. This is the same array gain as for a 50-element array.*

The above derivation is inaccurate because it assumes that the direction to the target doesn't change across the SAR aperture, in other words it assumes plane waves when the EM-fields are closer to spherical waves. The approximate SAR resolution obtainable from an aperture that is $\ell$ meters long is $\ell/2$ meters. So there is an effective limit to how long the aperture can be. However, for our desired resolution of 100 m, this is 200 m, which is beyond the length that can be physically managed.

Also, when the radar is operating in bistatic mode, the surface of the ice is likely to be specular. In this case, it is unnecessary to achieve half-wavelength sampling because our effective maximum look angle (backscatter angle) is limited to 4 to 7.5 degrees, which means that we can have grating lobes as long as they are more than 7.5 degrees from broadside. The allowance of grating lobes means that we can undersample the arrays. This might be another technique worth investigating. The disadvantage of this approach is that, if there are a few bright scatterers that fall in the grating lobes, they would severely interfere with the main signal. Another phenomena that focuses the antenna beam is mentioned in section 2.1 above; the

beamwidth of the antennas will be focused by the denser medium of ice which again allows for grating lobes in the “stop-band” of the antenna’s beam pattern – this time with no penalties since the antenna itself is incapable of picking up energy from these oblique directions.

# CHAPTER 4: INSTRUMENTAL AND MODEL ERRORS

A simple system model is used to determine SAR resolution and to show the SAR processor's sensitivity to position and dielectric errors and to specular surfaces. The propagation model, described briefly in the next section, is based solely on propagation delay. The model is used to create simulated measurements and then provides the filter coefficients for processing these measurements with a space-frequency domain matched filter.

## 4.1 SYSTEM MODEL

The following assumptions are made in the EM propagation model. All antennas are isotropic. The medium is homogeneous, isotropic and linear. The targets are isotropic point targets. The targets were assumed to be weak scatterers with no coupling or reflections between targets. Surfaces are simulated by placing many closely spaced point targets along a contour. The spacing used was one twentieth of a wavelength in the ice ($spacing = 0.05\lambda = \frac{c}{20nf}$). The transmitted signal has a flat spectrum across its bandwidth so the modulus of the transmitted waveform is a sinc function.

The simulated signal at the receiver is comprised of a summation of the individual returns from each of the targets as given in (2.4). The simulation of the dataset was done in the space-frequency domain and the SAR processing was also done in this domain. The SAR processing uses a matched filter except where noted.

The system geometry is shown in Figure 4-1. The geometry is taken from the optimal transmitter position results from the last chapter for 3000 m thick ice and a maximum backscatter angle of 5 degrees. The synthesized receiver antenna array lies on the x-axis (y = 0 and z = 0). The transmitter is placed at -2435 m on the x-axis. The middle of the receiving antenna array is at +2435 m on the x-axis. The ice is

3000 m thick (for rough surfaces, the ice is 3000 m thick on average). The swath to be measured is 1000 m wide unless indicated otherwise and is centered about the origin. The carrier frequency is 60, 150, or 350 MHz. The bandwidth of the sinc pulse is approximately 10 MHz, 20 MHz, or 40 MHz respectively except where noted. The index of refraction of the ice is taken to be that of solid ice or $n_{ice} = 1.78$ ($e_r = 3.17$). And the cross-track array is a linear equally spaced array with an antenna spacing of one half wavelength.

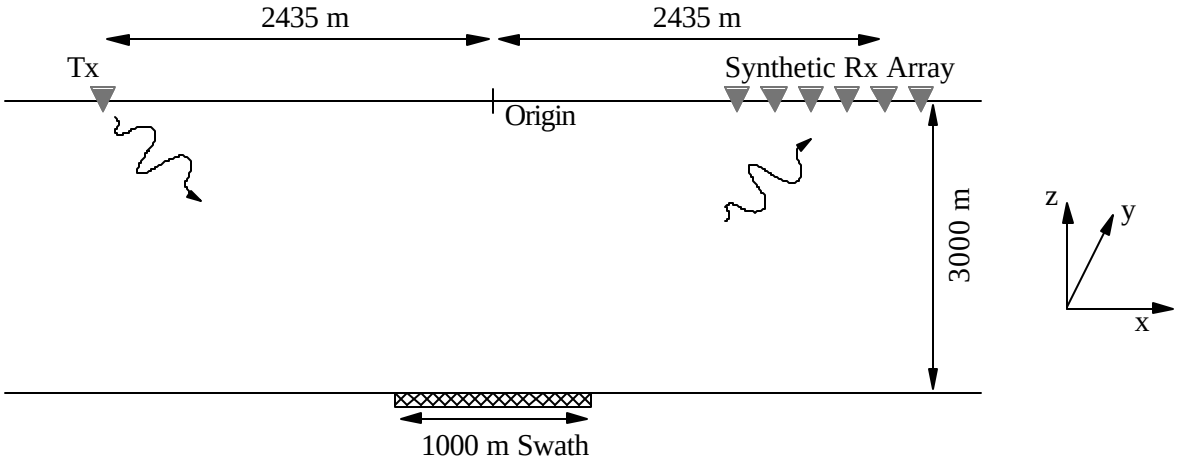


*Figure 4-1: System geometry*

## 4.2 SPATIAL RESOLUTION

The location of a target and its corresponding reflectivity are the outputs desired from the radar. This section uses the results from chapter three in which a minimum aperture size was determined to resolve targets to within 100 m along a 1000 m swath. The receiver aperture is set to this minimum aperture length.

The matched filter does not account for other targets when its coefficients are determined. When only one target is present this is not a problem as shown in Figure 4-2. When multiple targets are present, interference between targets can cause the estimated reflectivity of a target to be skewed by adjacent targets. This is shown in Figure 4-3 and Figure 4-4. There are eleven unity weight targets, buried 3000 m in the ice, spaced 100 m apart along the x-axis, starting at x = -500 m and ending at x =

+500 m. Since the weights are plotted in dB, the actual target weights are all 0 dB (unity weight).

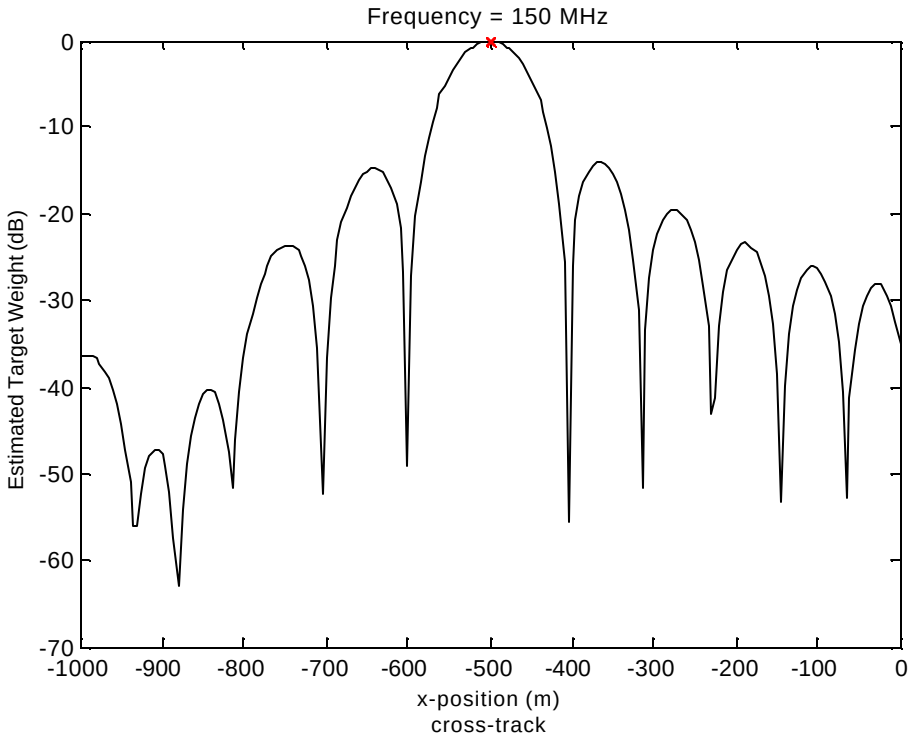


*Figure 4-2: Verification of the SAR resolution derivation in the last chapter. Note the null at –600 m, which is in agreement with the derivation.*

Three simulations were run in Figure 4-4. When only one target at position −500 m was present, data point indicated by a square, the estimated target weight was the actual weight. Both the matched filter and ML filter produce a perfect estimate for one target since the ML filter, as mentioned in chapter 2, simplifies to the matched filter when only one target is considered. The circle and exes represent a comparison between the matched filter and the maximum likelihood filter. The matched filter results only varied by about 1.3 dB from the expected value indicating that the minimum receiver aperture size required for a 100 m resolution determined in chapter three is fairly accurate. However, because the matched filter does not account for other targets, the interference from these targets, despite zero thermal noise, has caused the estimates to not be perfect. The maximum likelihood filter on the other hand, produces perfect estimates when no noise is present.

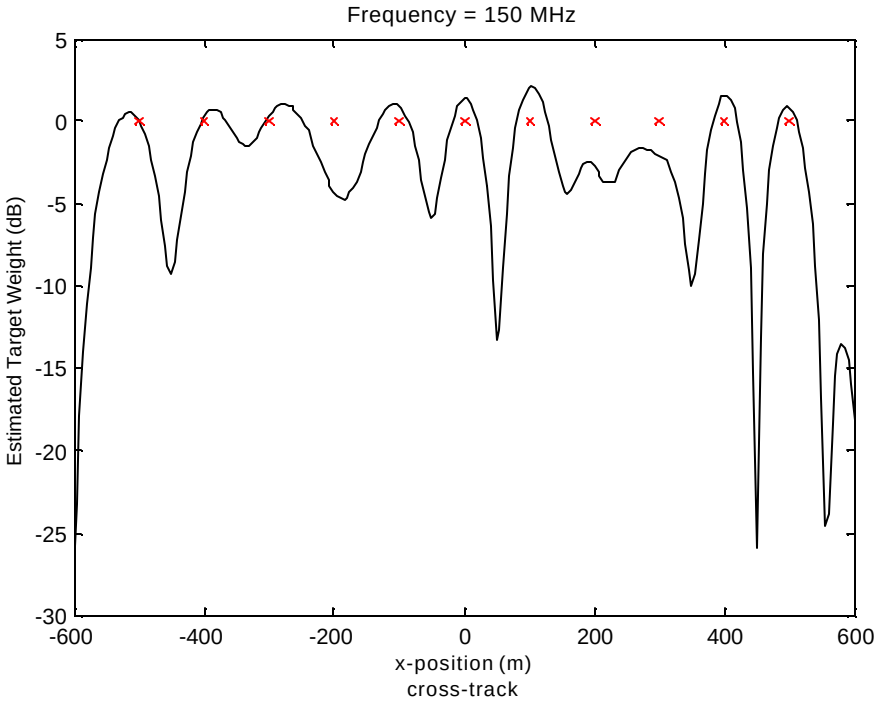


*Figure 4-3: Matched filter output of unity weight targets (0 dB). Most of the targets are imaged showing that the aperture length derived in chapter 3 to resolve 100 m spaced targets provides a decent estimate.*

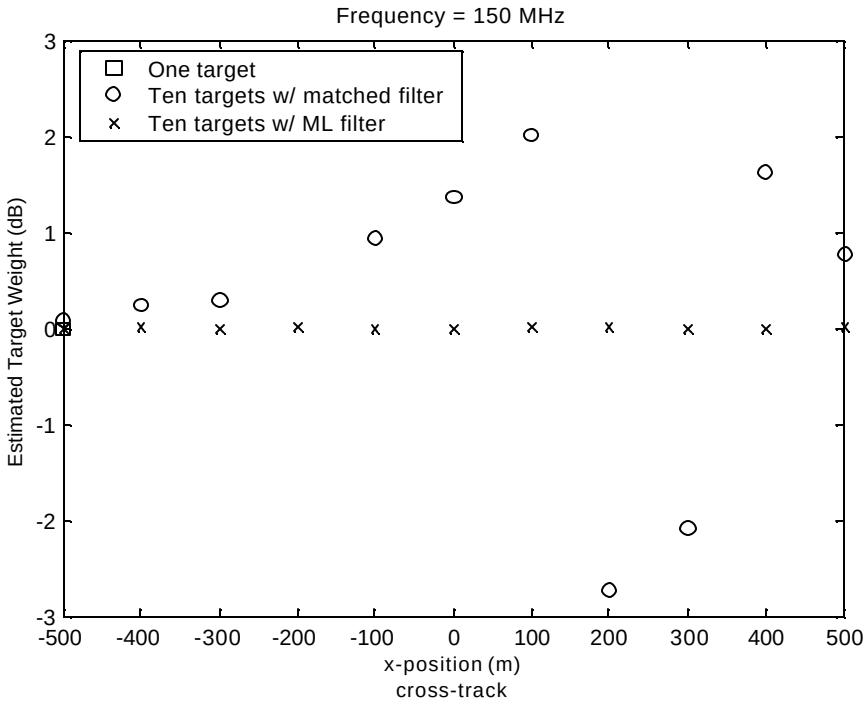


*Figure 4-4: SAR processed output of unity weight targets (0 dB). Note the ML filter produces exact results and the matched filter varies around the exact results.*

Figure 4-5 shows the noise to signal power at each target position for targets with weights uniformly distributed between 0.5 and 1.5. 2000 simulation runs were averaged to provide an estimate of the noise and signal power. This figure suggests that the maximum dynamic range with zero noise is around 6 to 8 dB when the matched filter is used.

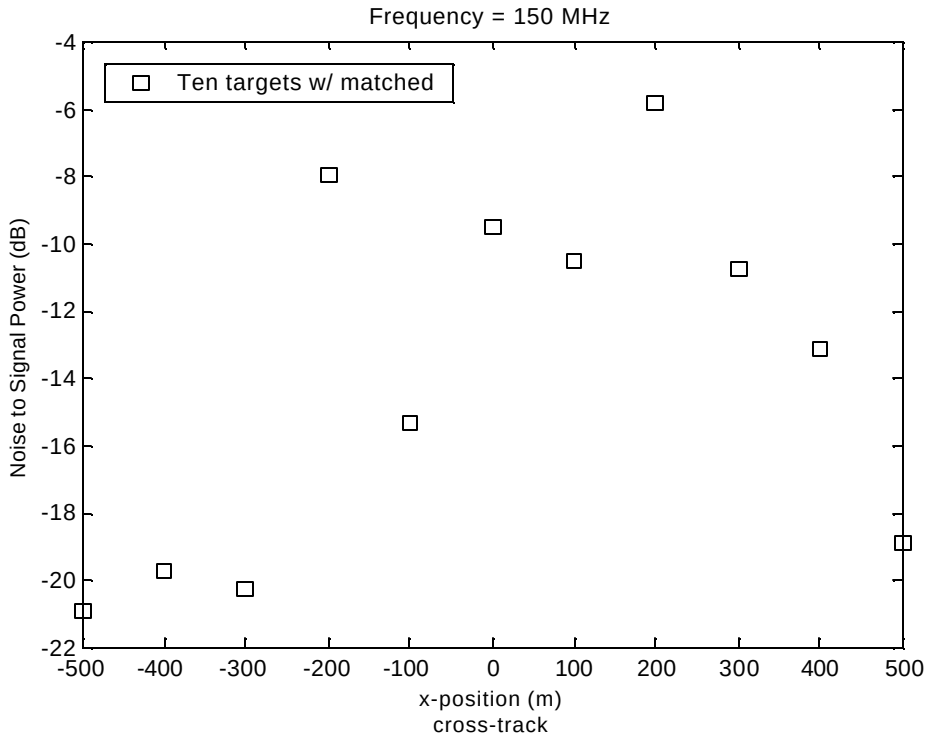


*Figure 4-5: Noise to signal ratio for matched filter with zero noise.*

One effect that has been mentioned several times is the variance in resolution across the swath. Because the receiver resolution is determined for the worst case scenario (i.e. the target furthest from the receiver aperture), the target closest to the receiver aperture has significantly better resolution. Figure 4-6 and Figure 4-8 demonstrate the two-dimensional resolution of single point targets at the ends of the swath (-500 in Figure 4-6 and +500 m in Figure 4-8). Note the side lobes for each point target. They follow the constant-range ellipse and are typical of the matched filter response.

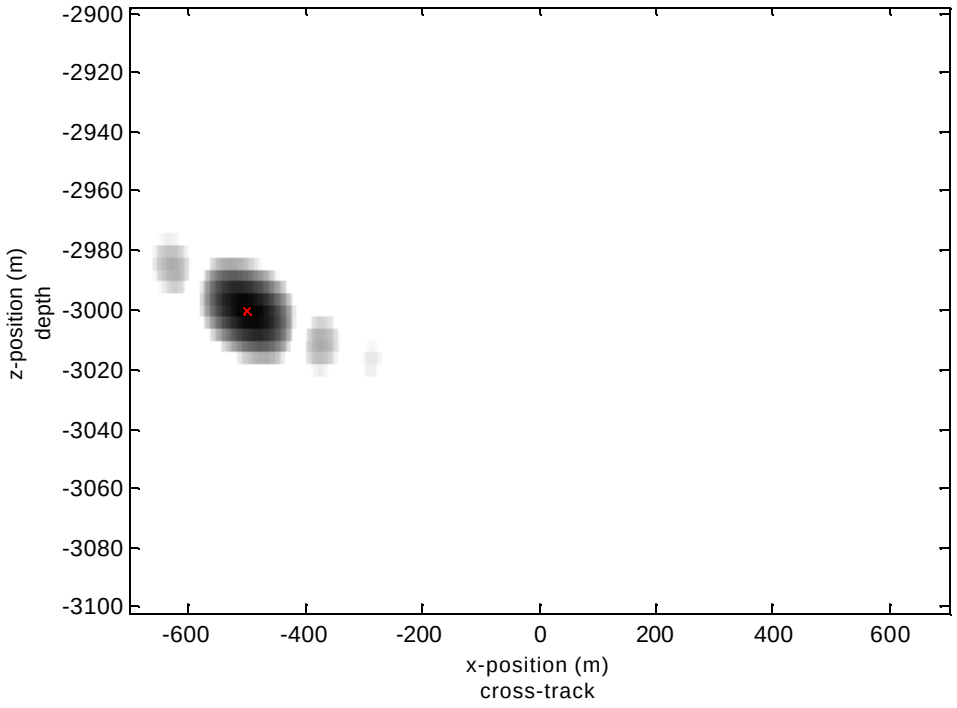


*Figure 4-6: Single point target located at –500 m along y-axis with a matched filter.*

Note that the cross-track resolution of the target located at –500 m is degraded from the resolution of the target located at +500 m. This is because the amount of ice surface subtended by a particular angle increases as the surface in question moves away from the broadside of the receiving antenna array (see **Error! Reference source not found.** for an illustration of this).

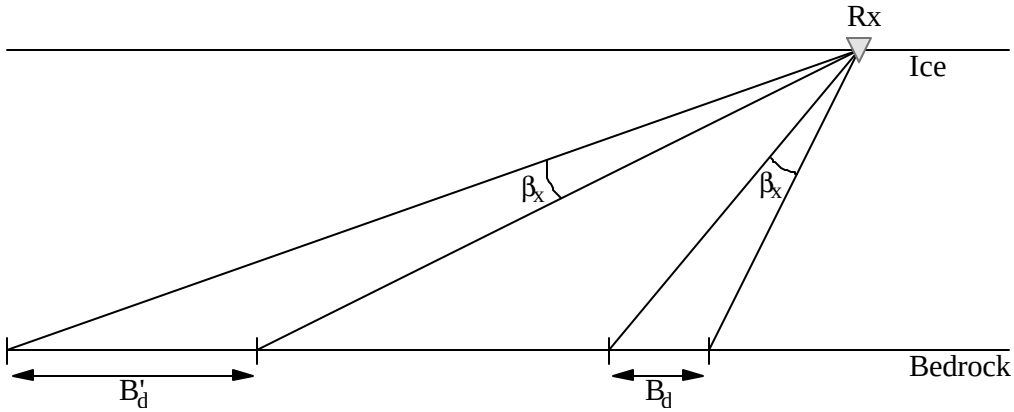


*Figure 4-7: The area subtended increases as the beam moves away from broadside and* $B_d' > B_d$ *for the same* $b_x$.

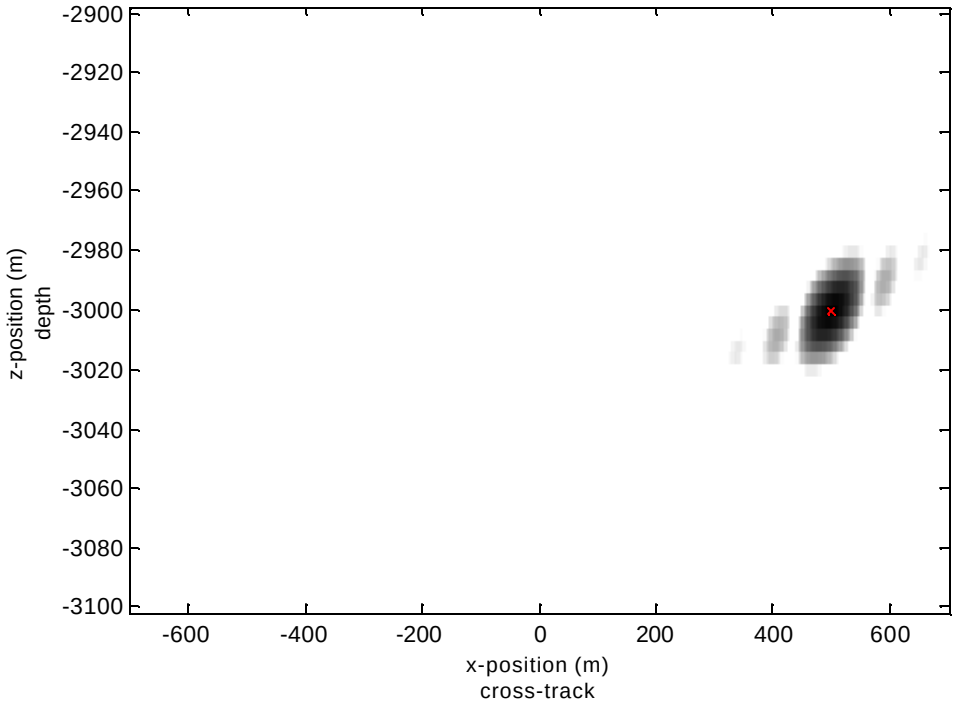


*Figure 4-8: Single point target located at +500 m along y-axis with a matched filter.*

## 4.3 ANTENNA POSITION ERRORS

The primary method for determining the position of the antennas will employ a global positioning system (GPS). GPS, even in differential mode, has errors that are a significant fraction of a wavelength. The standard deviation of position errors of the highest end systems usually falls between 5 to 10 cm for latitude and longitude with elevation errors twice that (i.e. 10 to 20 cm). The affect of the position errors is to introduce noise into the reflectance estimates for each target. The effects of position errors on reflectance measurements are shown in this section using simulations.

The actual positions of the receiving antenna array elements are equally spaced along the x-axis (cross-track axis). A Gaussian distributed error sequence is added onto the actual positions when SAR processing the data. Three different error correlation lengths are considered. This is to simulate the possibility that position

errors from one position to the next will be correlated, but become uncorrelated over space and/or time. The correlation lengths considered are 0, 10 and 50 m with 0 m corresponding to uncorrelated position errors.

For each simulation there were eleven unity weight targets, buried 3000 m in the ice, spaced 100 m apart along the x-axis, starting at x = -500 m and ending at x = +500 m. Each result consists of 500 simulation runs averaged together to get an estimate of the average noise to signal power ratio. The results were found for three different bands of operation: 55-65, 140-160, and 330-370 MHz with respective center frequencies of 60, 150, and 350 MHz. Two different standard deviations for the errors, $s = 0.05$ m and $s = 0.1$ m, were used. $s$ is related to each of the individual axes standard deviations as follows:

$$s_{Latitude} = s \tag{4.1}$$

$$s_{Longitude} = s \tag{4.2}$$

$$s_{Elevation} = 2s \tag{4.3}$$

Figure 4-9 through Figure 4-14 show the effects of position errors for the three different correlation lengths. The plots show the noise to signal power after maximum likelihood filtering has been applied. The noise comes completely from interference caused by position errors as the thermal noise was set to zero (i.e. $x = Gs + n = Gs + 0 = Gs$). Therefore if the position errors had been zero, the noise to signal power would have been $-\infty$ dB.

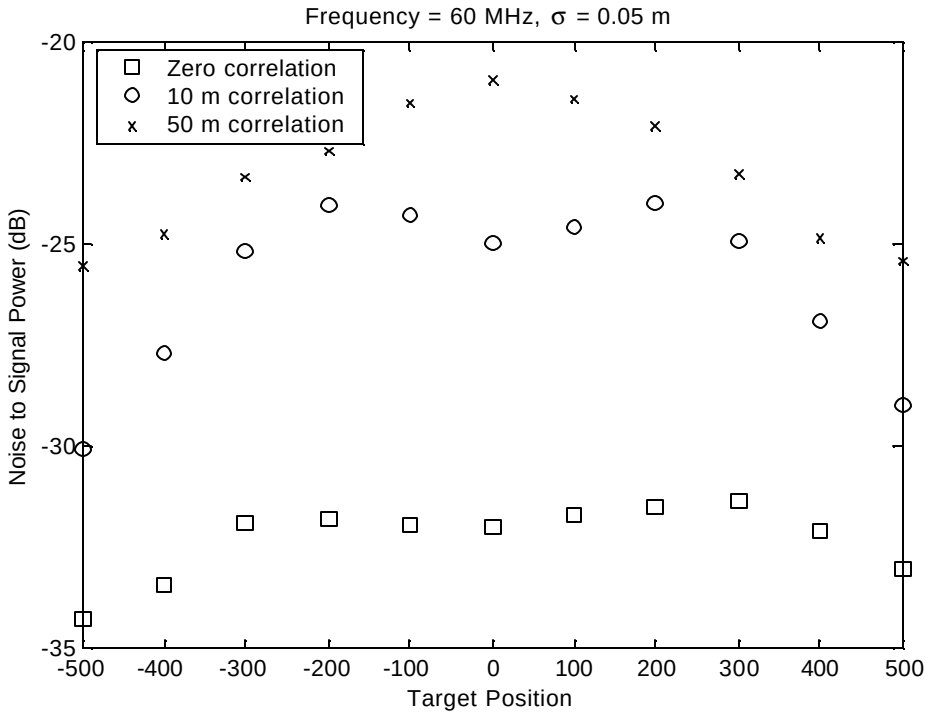


*Figure 4-9: Position errors for $f_c$ = 60 MHz (BW = 10 MHz) and $s = 0.05\ m$.*

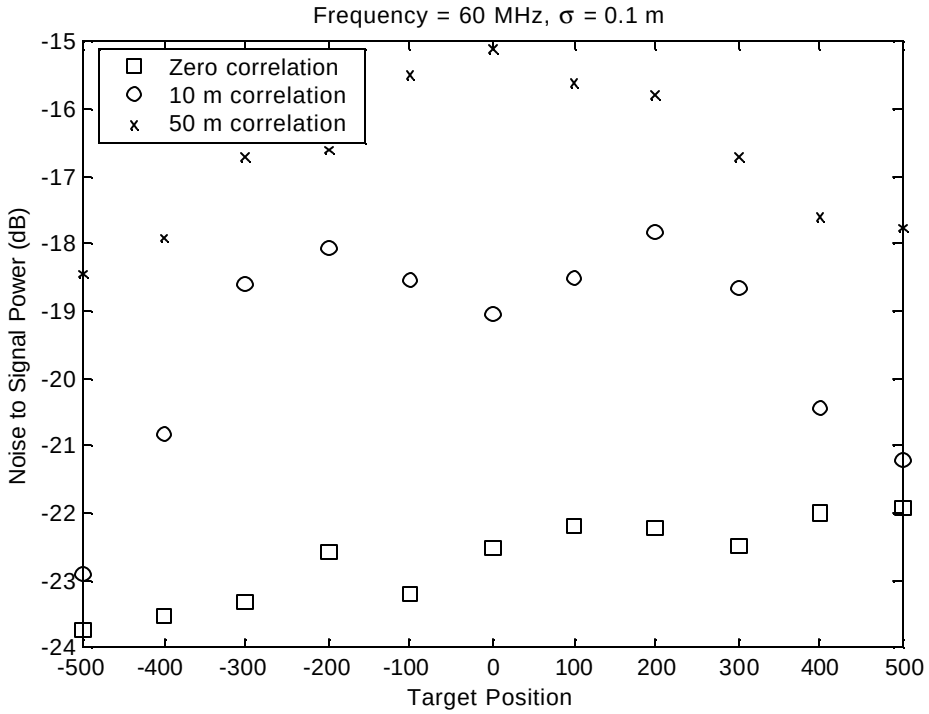


*Figure 4-10: Position errors for $f_c$ = 60 MHz (BW = 10 MHz) and $s = 0.1\ m$.*

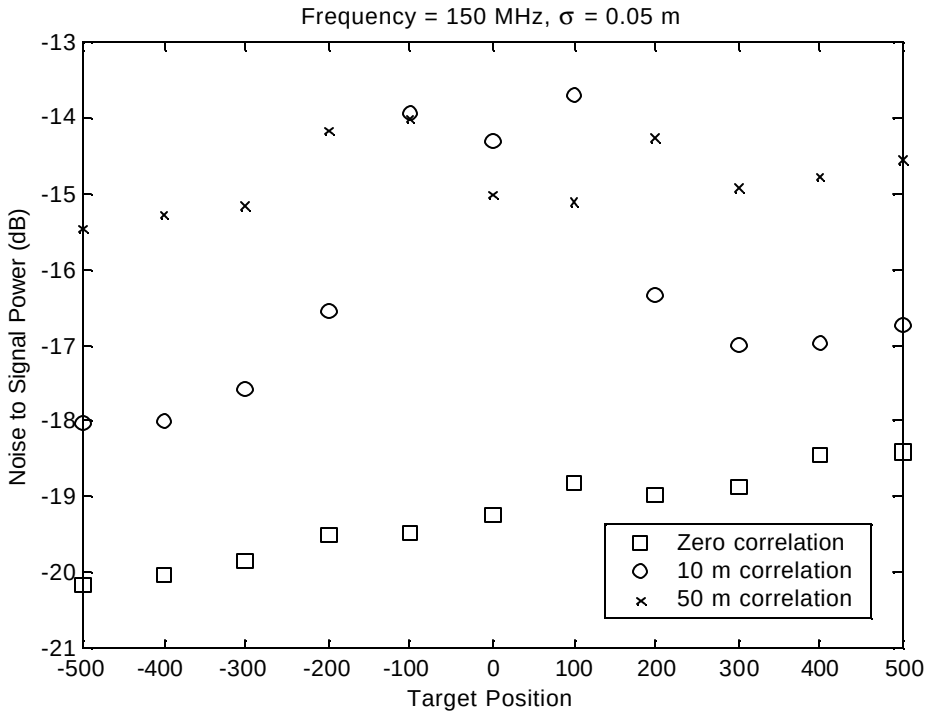


*Figure 4-11: Position errors for $f_c$ = 150 MHz (BW = 20 MHz) and $s = 0.05\ m$.*

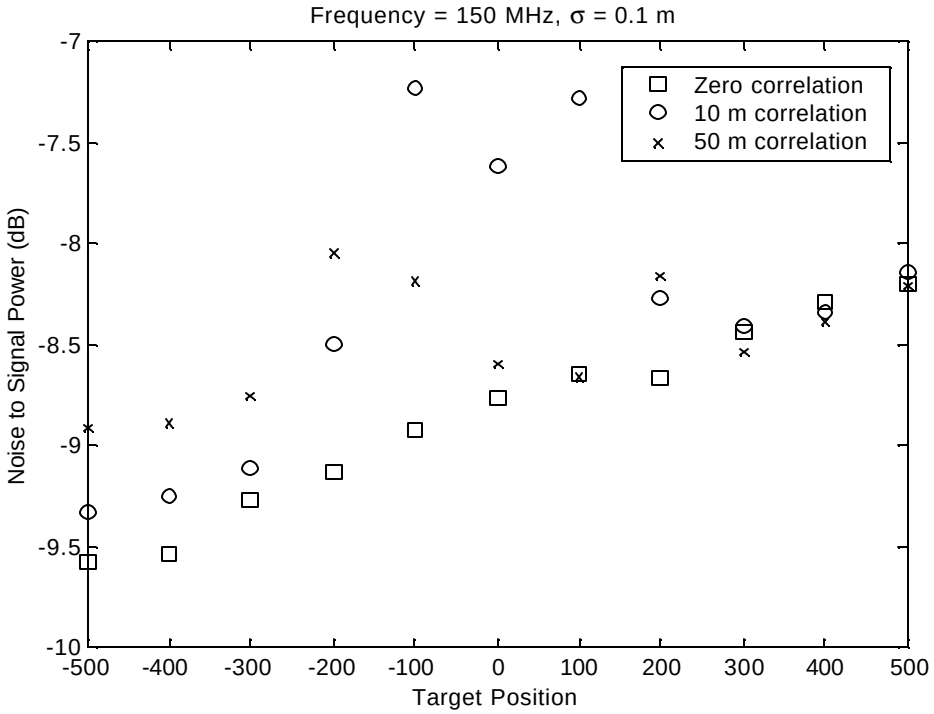


*Figure 4-12: Position errors for $f_c$ = 150 MHz (BW = 20 MHz) and $s = 0.1\ m$.*

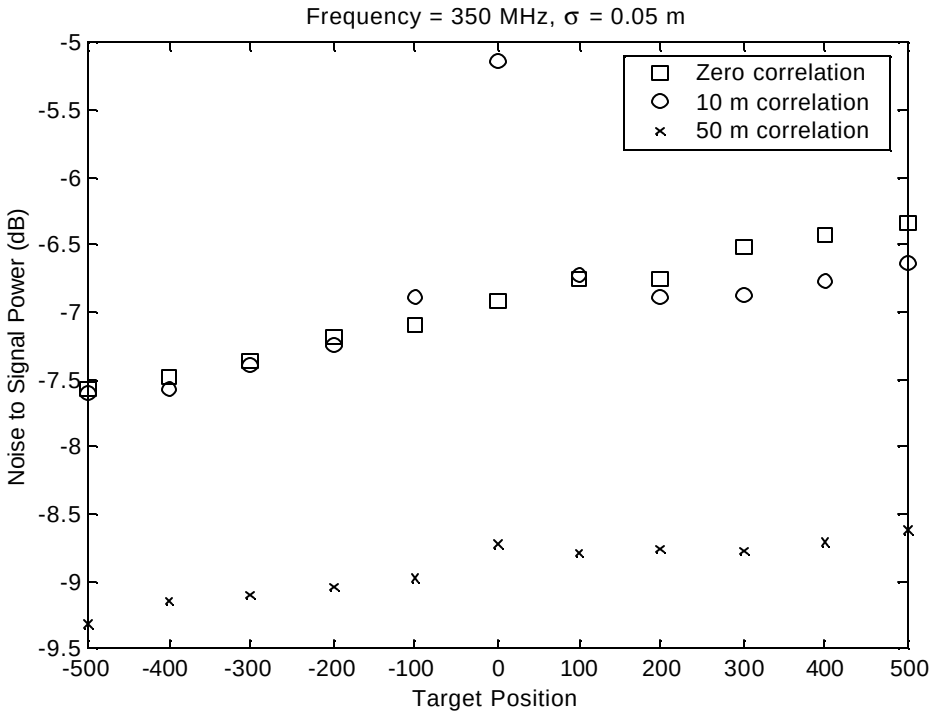


*Figure 4-13: Position errors for $f_c$ = 350 MHz (BW = 40 MHz) and $s = 0.05\ m$.*

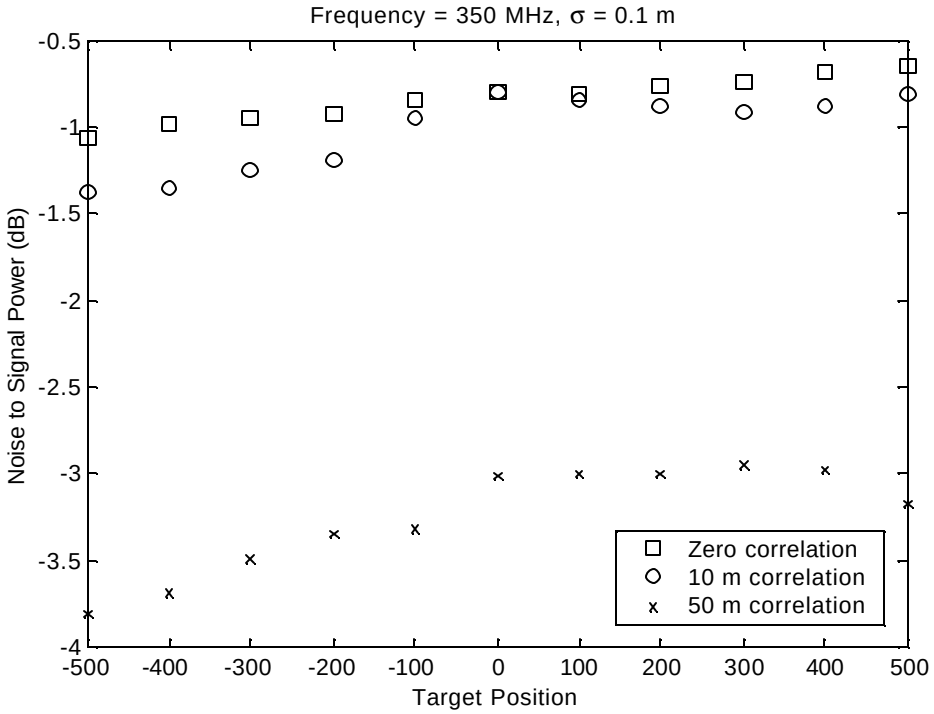


*Figure 4-14: Position errors for $f_c$ = 350 MHz (BW = 40 MHz) and $s = 0.1\ m$.*

For long enough apertures, errors from uncorrelated position errors seemed to partially cancel and produce noise to signal ratios that are around 6 dB lower than for correlated position errors. On the other hand, the 350 MHz aperture is much shorter than the 60 and 150 MHz apertures and the long correlation lengths meant that the position errors were relatively constant across the entire aperture. Constant position errors, only cause a position offset in the focused image. Since the position errors are very small (5-20 cm) and the time resolution is coarse (on the order of a meter), this offset has little effect on the estimated reflectance.

Also, note the trend toward improved noise to signal ratios as the target being considered moves toward negative x values. This is because the received response from those targets is less sensitive to z-axis movement. The z-axis position errors are twice as large, so being less receptive to z-axis movement produces better results.

Based on these results, the focusing algorithm can tolerate position errors on the order of a tenth of a wavelength while still providing about 7-10 dB of dynamic range between closely spaced targets. This translates to 28 cm at 60 MHz, 11 cm at 150 MHZ, and 5 cm at 350 MHz.

## 4.4 DIELECTRIC ERRORS

Figure 4-15 through Figure 4-19 show the eleven point targets focused with dielectric errors of 0, -0.05, +0.05, +0.1, and +0.2. The transmitted waveform is a Gaussian pulse which helps smooth the resultant image so that each target can be seen clearly (sinc pulse tends to have many side lobes which is visually confusing even though the main lobe of the target is sharper). The aperture length was also doubled so that clear distinctions between targets could be seen and compared for each of the different dielectric errors. The figures show that the focusing algorithm's ability to correctly identify the absolute position of targets is sensitive to dielectric error (as expected because the dielectric provides the map between time delay and distance). Based on the results, a spatially constant shift in the dielectric has not dramatically decreased the ability to relatively resolve the targets. However, because our

translation between time and space is skewed, the mapping from range bin to range has changed and our mapping between relative phase shifts between antennas to angle of arrival has changed.

The effects of dielectric error, which will most likely come from the firn layer, could be mediated by auto-focusing techniques, such as maximizing the contrast of the image or imaging with sub-apertures and comparing the results between sub-apertures. These techniques were not investigated.

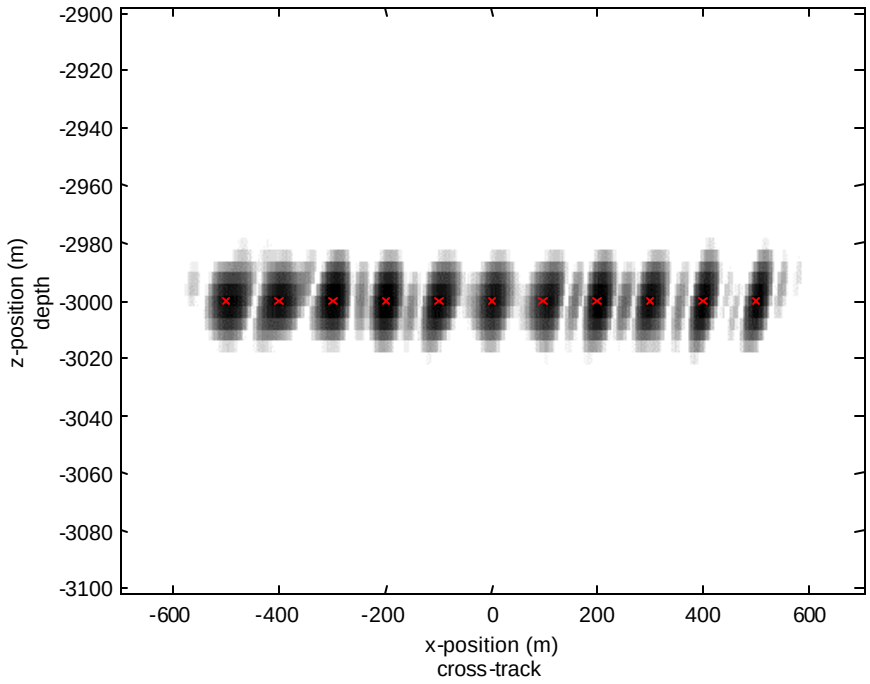


*Figure 4-15: Zero dielectric error.*

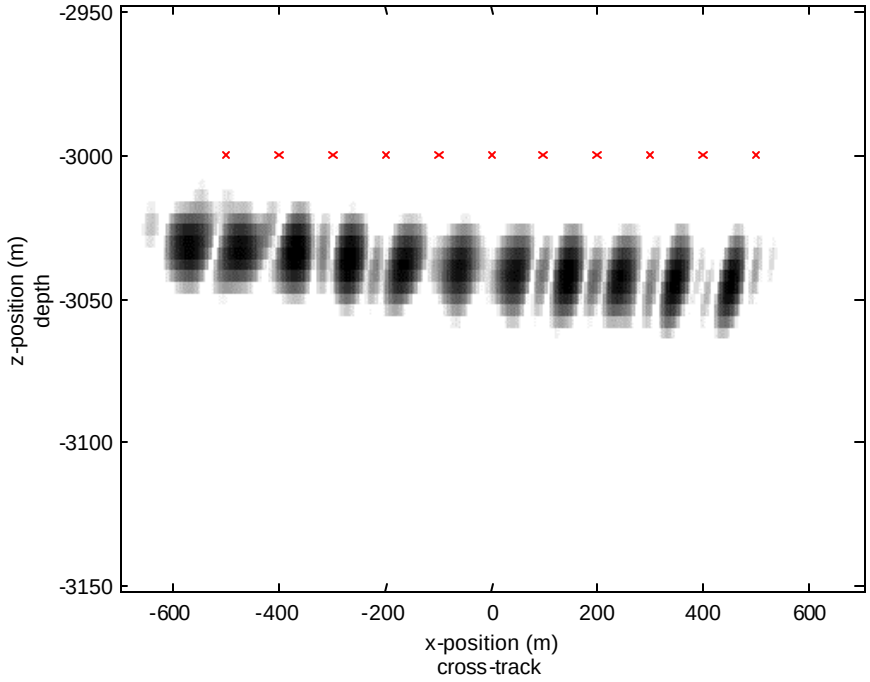


*Figure 4-16: -0.05 dielectric error*

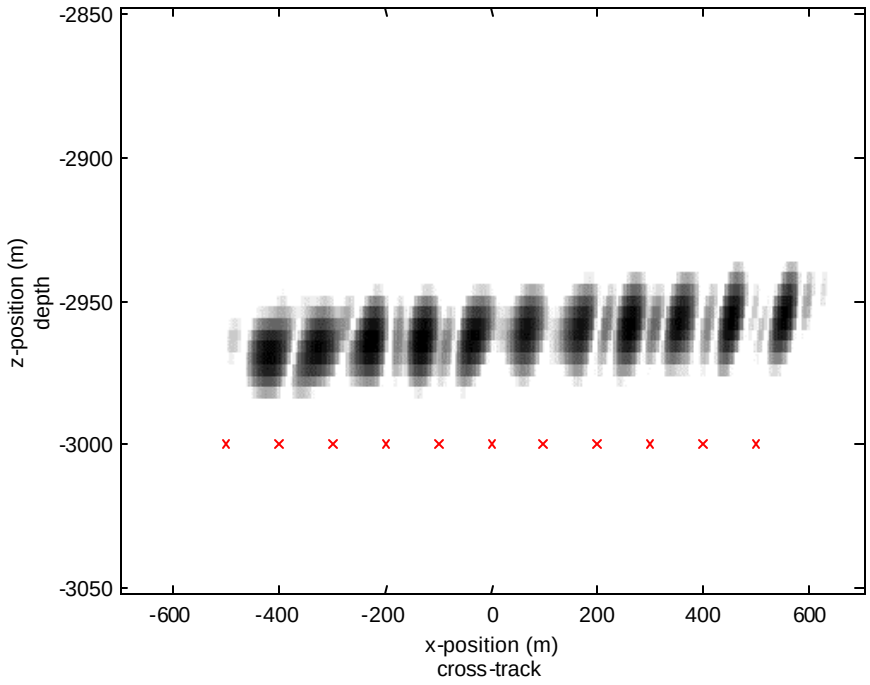


*Figure 4-17: Dielectric error of +0.05*

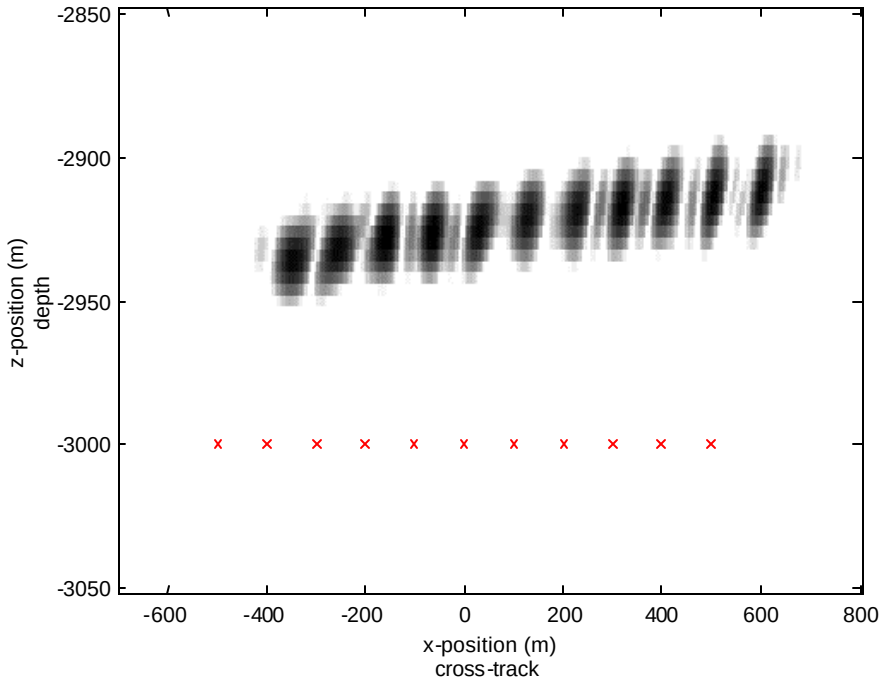


*Figure 4-18: Dielectric error of +0.1*

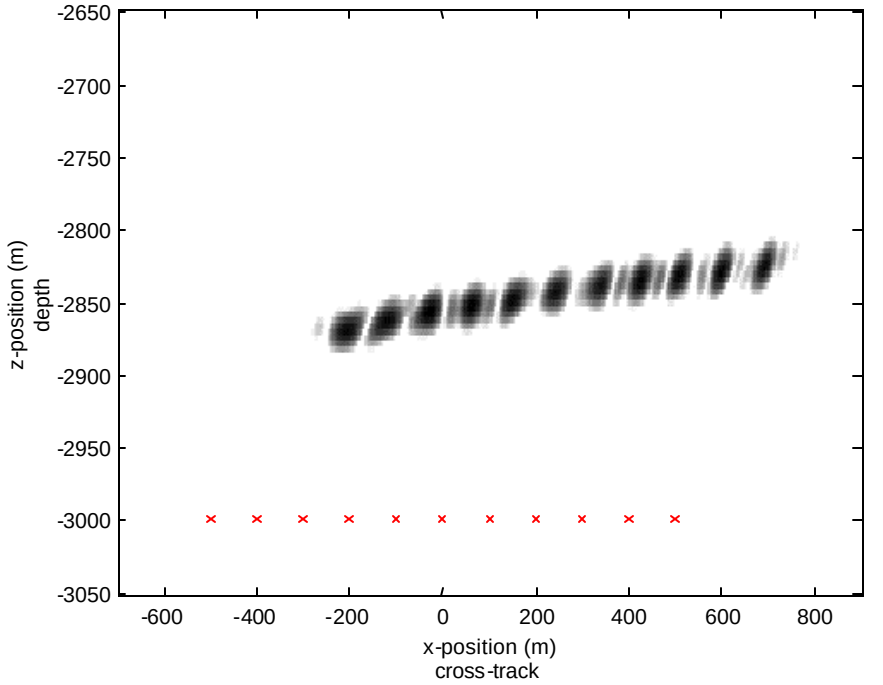


*Figure 4-19: Dielectric error of +0.2*

## 4.5 EFFECTS OF SPECULAR SURFACES ON SAR PROCESSING

As mentioned in chapter two, the uncorrelated weak-scatterers assumption does not apply to quasi-specular surfaces because the targets are correlated. In our case, we are measuring topology with a large RMS height of 7 m (large compared to the wavelength) and a small RMS slope (RMS slope m on the order of 0.02 to 0.04) [19]. This means that we will only be able to image the extrema (i.e. the tops of hills and the bottoms of valleys). This is because much of the target response is specular and suffers from Fresnel diffraction. Most to all of the return falls into the first Fresnel zone. The first Fresnel zone is the specular path (in a communication system this is the line-of-sight path). The second, third, fourth, etc. Fresnel zones provide very little contribution (in a communication system these are dealt with by diffraction models such as knife-edge diffraction).

Figure 4-20 and Figure 4-21 show how the focusing algorithm fails to properly image smooth surfaces. In both cases, the contour extends from –1000 m to +1000 m and the original contour is drawn in red over the focused image. The frequency band used was 140 to 160 MHz with the number of elements dictated by the results from chapter three. These results show that specular responses can be simulated fairly well by placing a series of point targets close together. With a large RMS height and low RMS slope, the contours look like a series of "specular" sheets attached together. To properly image these surfaces, only the part of the antenna aperture that received substantial energy from the target should be weighted heavily. In reference to (2.4) this means larger values for $G$. This additional information requires including a component in the EM-model that includes correlation between targets.

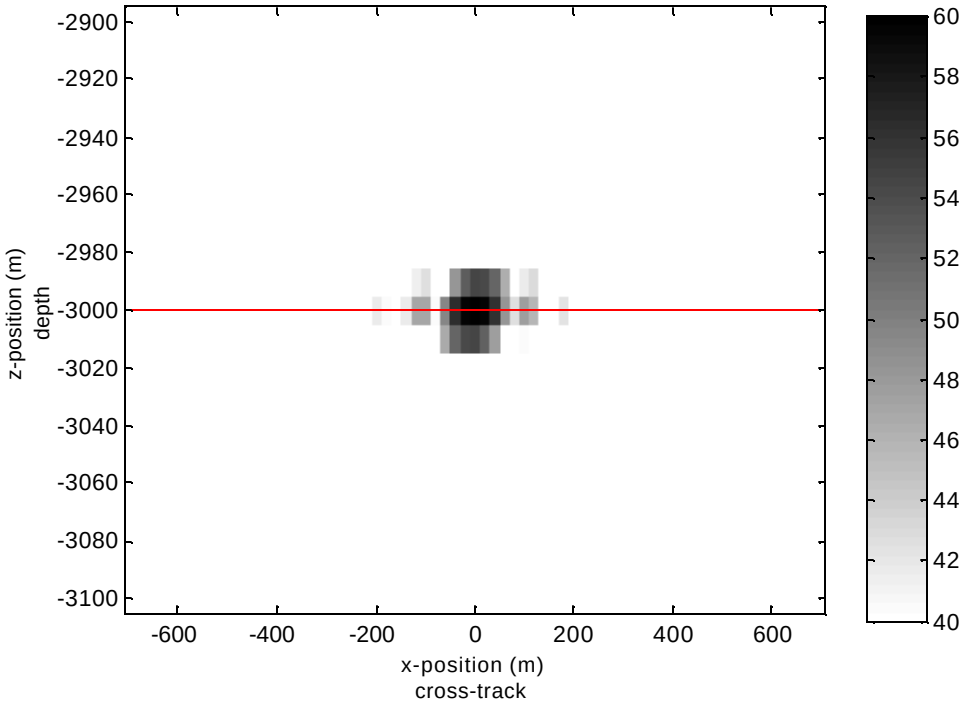


*Figure 4-20: Specular surface (0 m RMS height and 0 m RMS slope contour) and its focused image.*

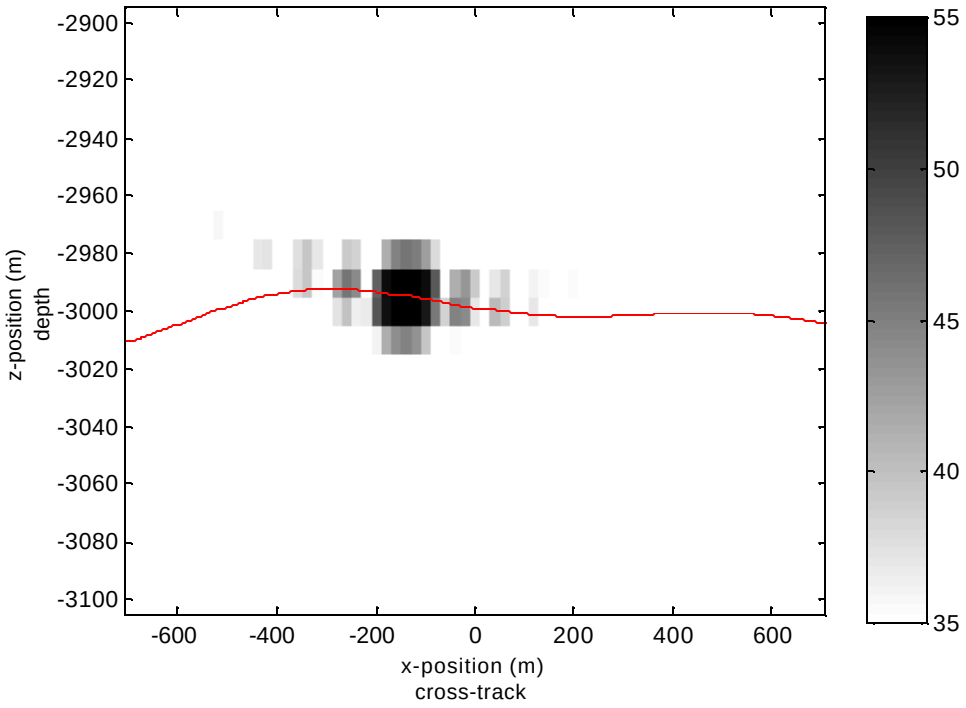


*Figure 4-21: 7.0 m RMS height and 0.02 m RMS slope contour and its focused image.*

# CHAPTER 5: MEASUREMENTS

## 5.1 MEASUREMENT SETUP

### 5.1.1 SYSTEM LEVEL

The sandbox facility, illustrated in Figure 5-1, consists of a 181" by 157" by 72" box filled with quartz sand. There are two permanent PVC pipes buried over three feet down in the sand. One pipe extends the whole length and is parallel to the x-axis. The second pipe extends about three feet into the sandbox and is open ended. These pipes are buried over a foot beneath the targets that will be measured and therefore should not interfere with the measurements.

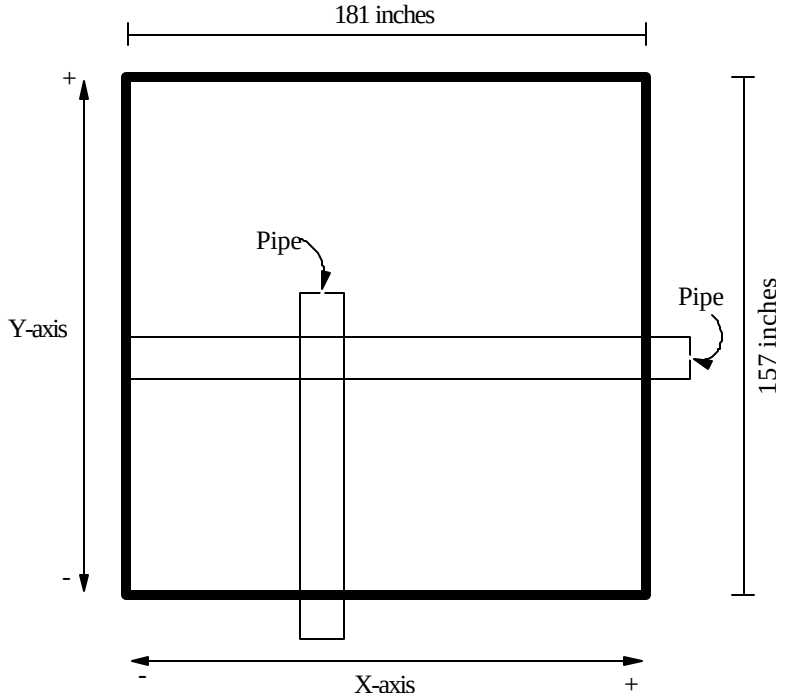


*Figure 5-1: Diagram of sandbox test facility (looking down onto sandbox).*

The sandbox includes a linear motion system that allows for two antennas to be moved independently. One antenna mount was used for the transmitter and the other for the receiver. Two servomotors move each antenna mount – one servomotor

controls x-movement, the other controls y-movement. Optical encoders are used to determine how far the antennas have moved. The optical encoders are nominally accurate to within 1/356 of an inch (i.e. there are 356 encoder "counts" per inch). However, the antenna mounts are connected to the servomotors and the shaft of the optical encoder by a plastic belt that can stretch. Also, while in motion the antenna mounts occasionally vibrate. Errors in the optical encoder due to vibrations during motion and the stretching of the plastic belts increases this error to about 1-2 mm (over a large area after moving the antennas multiple times). Given that SAR imaging usually requires at least one-tenth of a wavelength accuracy, the minimum wavelength suggested by this position error is ten times 2 mm. Therefore the highest frequency that should be used in SAR processing with this system is:

$$f_{\max} = \frac{\frac{c}{\sqrt{e_{sand}}}}{l_{\min}} = \frac{\frac{3e8}{\sqrt{3.05}}}{10 \cdot 0.002} \approx 8.6\ GHz \tag{5.1}$$

Here, a sand dielectric of 3.05 is used which is based on measurements described in section 5.2 below.

The servomotors[10] and optical encoders are connected to an industry standard architecture (ISA) board for automated control of the system. Functions have been written so that the ISA board can be controlled from Matlab as well as from the DOS command line. Along the tracks that move the antenna mounts are conduits for RF cables that are used to attach a network analyzer to the antennas. The RF system diagram is shown in Figure 5-2. The network analyzer is connected to a Peripheral Component Interconnect-General Purpose Interface Bus (PCI-GPIB) card that allows the network analyzer to be controlled from Matlab (or any other program that interacts with the GPIB).

[10] The servomotors are driven by external amplifiers, but the amplifiers are controlled by the ISA board.

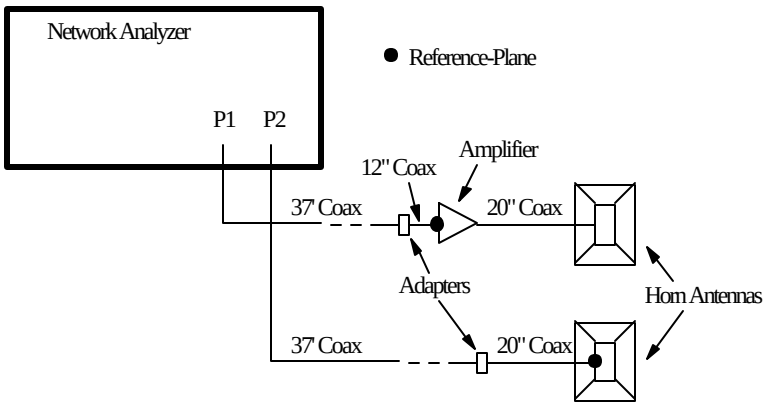


*Figure 5-2: RF circuitry for sandbox.*

Ideally the network analyzer would be calibrated at the outputs of the horn antennas. However, providing known loads to the horn antenna outputs is a difficult problem. Also, the amplifier has over 80 dB of reverse-isolation (see Figure 5-3) making the calibration of port 1 after the output of the amplifier essentially impossible. Since the amplifier has a reflection coefficient of –10 to –20 dB, a dynamic range of over 70 dB would be required to isolate the two signals as well as many averages to lower the noise floor beyond 90 dB. The directivity of the network analyzer is only 55 dB after error correction, which means the necessary dynamic range cannot be achieved. This calibration was attempted several times with no success.

Since the non-ideal amplifier characteristics and connector/cable mismatches were not removed in the calibration process these must be accounted for in the post-processing. This is detailed in section 5.4 below.

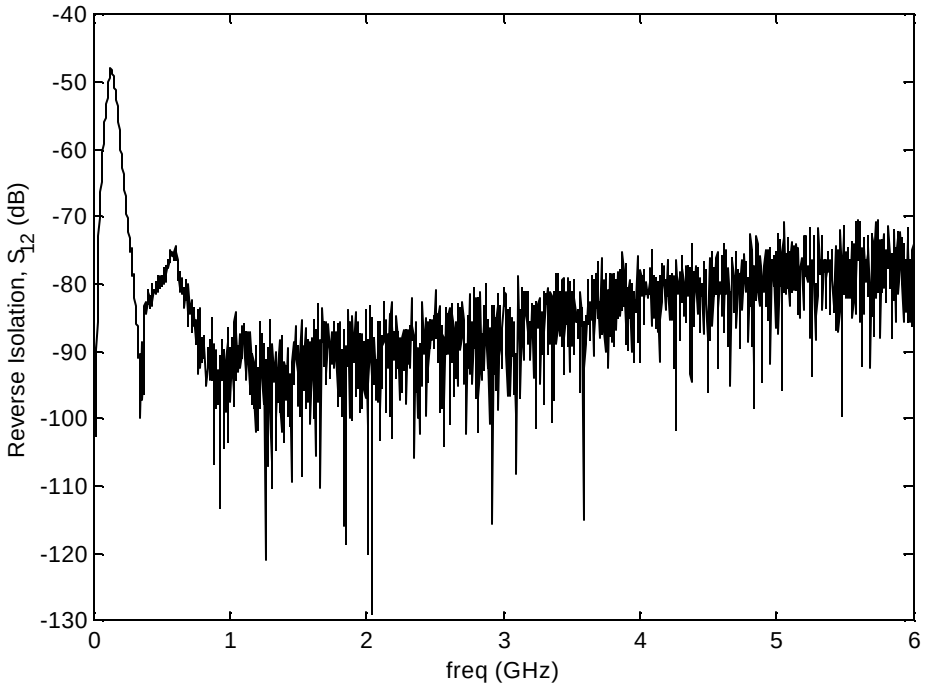


*Figure 5-3: Reverse isolation ($S_{12}$) of the amplifier.*

## 5.1.2 SYSTEM PARAMETER SELECTION

The first parameter selected was the frequency range. The sandbox is too small for the operating frequencies of the final radar system (55-370 MHz). Therefore the wavelength had to be scaled to fit the sandbox. To keep the SAR aperture smaller than a meter requires a wavelength on the order of 10 cm or smaller, which corresponds to a frequency of 3 GHz. The network analyzer in the sandbox laboratory is a Hewlett-Packard 8753D with a maximum operating frequency of 6 GHz. While other network analyzers were available that could handle up to 40 GHz, the wavelength is only 5 cm at 6 GHz and the positioning accuracy already imposed at this frequency makes this a reasonable upper bound. As mentioned in the previous section, the position errors in the linear motion system suggest a maximum operating frequency of 8.6 GHz. Also, lower frequencies are less sensitive to phase changes when flexing the cable, which necessarily happens when the antennas are moved to each measurement position.

The next consideration was the operating frequencies of the devices in the system. The amplifier has a frequency range from 0.5 to 12 GHz and the horn antennas have a frequency range from 2-18 GHz. The horn antennas, therefore, set a lower bound on the operating frequency of 2 GHz; the $S_{11}$ parameter at 2 GHz is actually above –10 dB and transients are already severe so pushing this boundary lower did not seem reasonable. A large bandwidth helps isolate targets in time, but we do not want to use too large of a bandwidth that the time resolution becomes so fine that we are unable to properly test the spatial resolution. If a B = 4 GHz system were used, the range resolution would be:

$$s_r = \frac{c}{B\sqrt{e_{sand}}} = \frac{3e8}{4e9 \cdot \sqrt{3.05}} = 4.3\ cm \tag{5.2}$$

For B = 1 GHz, the range resolution is four times this:

$$s = \frac{c}{B\sqrt{e_{sand}}} = \frac{3e8}{1e9 \cdot \sqrt{3.05}} = 17.2\ cm \tag{5.3}$$

While we may want to only use 1 GHz of bandwidth, collecting data over a wide bandwidth allows for more flexibility in post-processing because sub-bands of the data can be processed allowing a narrower band system to be mimicked. The disadvantage to collecting data over a large bandwidth is the increase in the data collection time.

Based on the above considerations a bandwidth between 2 and 6 GHz was chosen (B = 4 GHz). The horn antenna set the low frequency limit and the network analyzer set the upper frequency limit. This set of frequencies provides a wide bandwidth, is low frequency enough that positioning requirements are not too stringent, and is high frequency enough that the SAR aperture can still be kept under 1 meter.

Once the bandwidth is set, the number of frequency points can be determined by finding the maximum path length in the system. The maximum path length is measured from the transmitter reference plane to the receiver reference plane. The

maximum path length, $d_{\max}$, in this system will be set by the sky shot[11]. Since the sandbox is indoors, the sky shot will have a substantial reflection from the ceiling. This path is close to 10 m. We would like the frequency sampling to be such that time-domain aliasing is negligible. To determine this we take the maximum path and divide this by the velocity. This gives the time taken to travel along the path. Then we determine the number of time samples this would be with a sampling frequency of 4 GHz. Since the number of time samples must equal the number of frequency samples we are finished. Effectively this means that a frequency spacing of $df$ can resolve time changes on the order of $df^{-1}$. Therefore, $df$ is selected such that $df^{-1}$ is equal to the time taken for the major reflection to die down. The time taken for a single reflection from the ceiling is $\frac{d_{\max}\sqrt{e_{air}}}{c}$ and $df = \frac{B}{N_t}$, therefore the number of points, $N_t$, is restrained by the following equation.

$$N_t > \frac{d_{\max}\sqrt{e_{air}}}{c} B = \frac{10 \cdot 1}{3e8} 4e9 = 133 \ pts \tag{5.4}$$

The larger the number of points the more data that must be stored and the longer data collection takes. However, because of the low cost of data storage and the sweep time restraints described below, the number of points was chosen to be 1601 to minimize potential aliasing problems from multiple reflections.

Sweep time, IF bandwidth and averaging are several interrelated system parameters that must be considered. The sweep time determines how long the network analyzer takes to pass or "sweep" through its list of frequency points once. The maximum path length and the SNR requirements determine the sweep time. For determining the sweep time, the maximum path length is measured from the network analyzer's source to the network analyzer's receiver regardless of where the reference plane is. When the network analyzer is in sweep mode (as opposed to stepped mode),

[11] The horn antennas are turned upside down on their mounts in the sandbox laboratory so that the broadside of the horn antennas is pointing towards zenith (i.e. the ceiling).

it operates similar to a FMCW radar that only reads the first range bin. The first range bin is detected by the IF filter.

Let the sweep time be $T_R$ and the IF bandwidth be $B_{IF}$. The RF source of the network analyzer is swept over B Hertz in $T_R$ seconds, which corresponds to a sweep rate of $\frac{B}{T_R}$ Hertz per second. A discontinuity located x meters from the source will create a reflection of the signal that when received by the receiver is delayed by $\frac{2x\sqrt{e_{medium}}}{c}$. This time delay corresponds to a frequency shift of $\frac{2x\sqrt{e_{medium}}}{c}\frac{B}{T_R}$. When this signal is mixed with the source and low pass filtered a pure frequency tone equal to the frequency shift will be left. All significant reflections must create frequency shifts that are within the bandwidth of the IF bandwidth so that $B_{IF} > \frac{2x\sqrt{e_{medium}}}{c}\frac{B}{T_R}$ or else the reflection will be rejected by the filter. Given that the bandwidth B is fixed, this means that either $B_{IF}$ or $T_R$ must be made larger. When $B_{IF}$ is made larger than the amount of noise allowed through the IF filter is increased and more measurement averages must be done to keep the SNR constant and hence the measurement time increases. If $T_R$ is increased, the measurement time increases directly. If either $B_{IF}$ or $T_R$ is made too small, some reflections will fall outside of the IF filter and not be recorded.

As shown in Figure 5-2, the cables to the antennas are each 37 ft long with a velocity factor of 0.85. In addition to this, the sky test requires about 10 m of free-space length. The total path length's free-space equivalent is

$$L = 2\left(37\text{ ft}\cdot\frac{0.3048\text{ m}}{1\text{ ft}}\cdot 0.85^{-1}\right)+10\text{ m} = 36.5\text{ m} \tag{5.5}$$

If we allow for up to ten full path-length reflections then the IF bandwidth required to see up to ten of these reflections unambiguously is

$$B_{IF} = 10 \cdot \frac{L}{c} \frac{B}{T_R} = \frac{4871}{T_R} \tag{5.6}$$

Setting $B_{IF}$ to 3 kHz (which sets the SNR for a single pass with no averaging applied yet) and solving for $T_R$ we get

$$T_R = 10 \cdot \frac{L}{c} \frac{B}{B_{IF}} = \frac{4871}{B_{IF}} = 1.6 \text{ s} \tag{5.7}$$

To verify that this sweep time was sufficient, the network analyzer's sweep time was set to 0.5 s and raised until no changes were seen between sweep time increases (hence indicating that all significant reflections were included). This value was around 1.3 seconds, which is the final value that was chosen. As mentioned above, the number of points was set to 1601. Normally, setting the number of points to a larger than necessary value means that more time needs to be taken since each point requires $B_{IF}^{-1}$ seconds to resolve plus overhead to account for network analyzer processing time. The total time required to sweep through 1601 points with two-port error correction comes out to 1.3 seconds for the network analyzer that was used.

The maximum power output by the network analyzer is 10 dBm and the maximum recommended output power is 5 dBm. With cables losses (4 dB in each cable) this comes to –3 dBm of energy that is actually broadcast and received from the channel. We used a 25 dB amplifier to increase the signal power. Since the recommended maximum input power for the network analyzer is 10 dBm, the source power was set to $-8$ dBm. After the gain of the amplifier and loss in the cables this comes out to be 9 dBm.

Finally, ten averages were chosen to improve the SNR. Three datasets of ten averages were taken with each measurement to provide a rough estimate of the noise power.

The SNR was measured by taking multiple datasets of the sand with no targets. The resultant SNR was determined by taking the ratio of the signal strength to the variance between datasets. The SNR is plotted versus time in Figure 5-4.

Notice that the SNR peaks around the direct path and surface reflections (range bins 18 through 30) and then slowly rolls off. As can be seen from Figure 5-4, the SNR is above 45 dB starting from the direct path response out to range bin 70, which is beyond the range bins that will contain targets. A reduction in the number of averages or the removal of the amplifier could probably be tolerated considering how high the SNR is. By reducing the number of averages, the experiment time could be decreased and removing the amplifier would allow calibration directly at the transmit antenna's input.

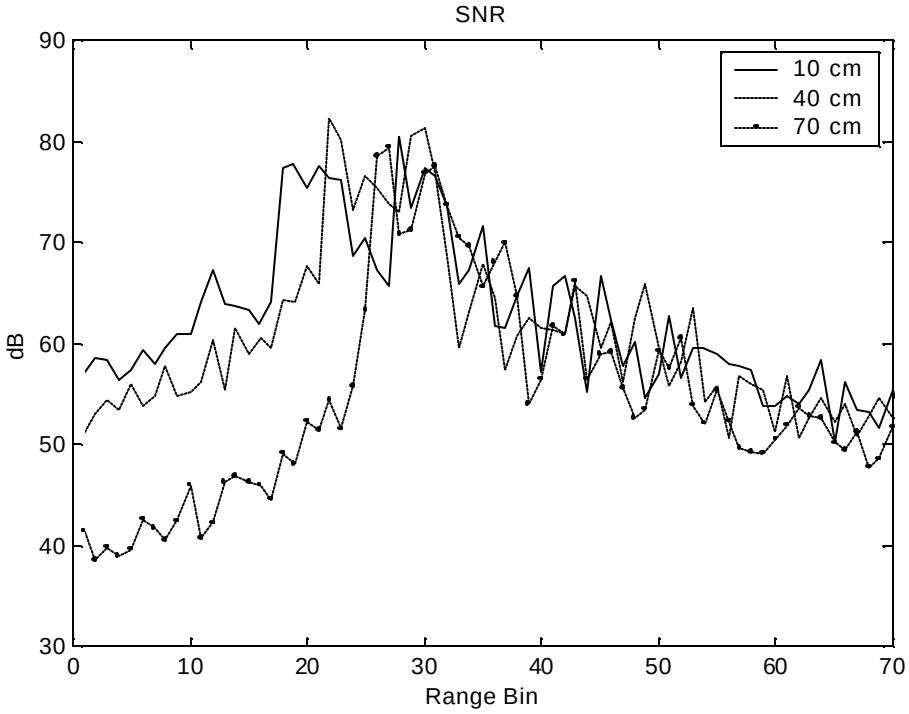


*Figure 5-4: SNR for 10 cm, 40 cm, and 70 cm separation of the antennas. The SNR is over 45 dB for the range bins of interest.*

### 5.1.3 SYSTEM GEOMETRY

A bistatic system geometry was used to take the measurements and calibrate the system. Even by increasing the frequency of the system to 2-6 GHz, the dimensions of the ice sheet could not be modeled completely – the ice sheet is kilometers thick which translates to hundreds of wavelengths. In the sandbox, we would need to bury the targets over 30 meters deep to get a comparable geometry.

This is because the frequency has only been scaled by 10 times, while the ice sheet is around 1000 times thicker than the sand. Despite this, the sensor placement was kept as close as possible to the expected placements in the final radar system. Figure 5-5 shows the general setup of a cross-track transect with a metal tube buried in the sand. The transmitter remains stationary while the receiver makes the cross-track transects. Then both the transmitter and receiver move forward in the along-track direction together. An example of 5 cross-track transects from the measurement set for the metal tube test is shown in Figure 5-6. The highlighted section is from a single cross-track transect. All of the measurements that were taken are a variation of Figure 5-6 changing only the step-size between measurements.

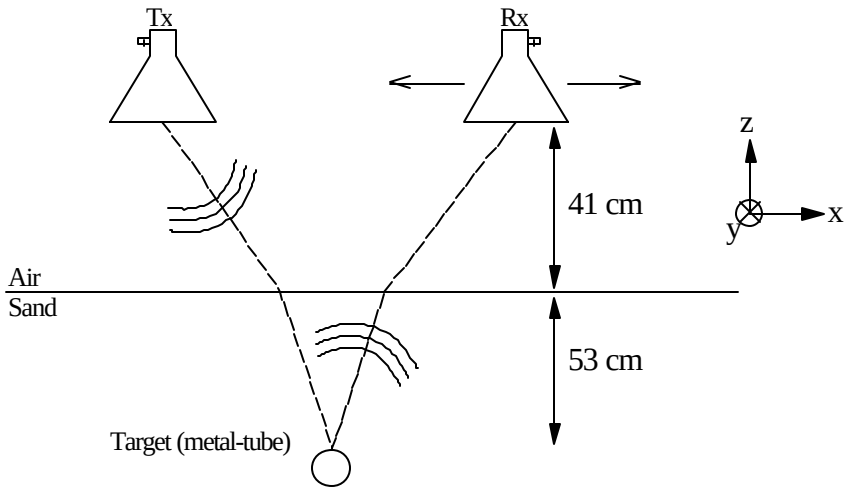


*Figure 5-5: Profile of horn antenna configuration for a cross-track transect.*

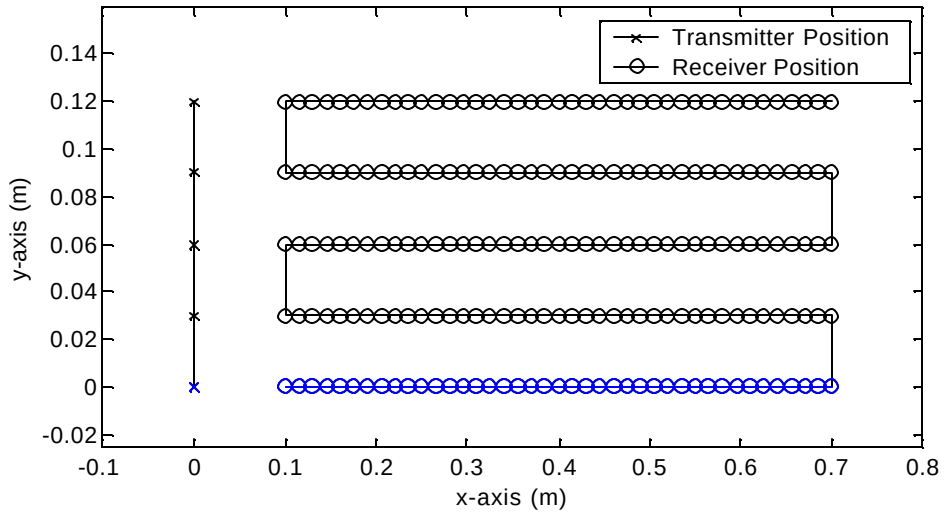


*Figure 5-6: Example of a measurement set looking down onto the sandbox. The highlighted section is from a single cross-track transect.*

## 5.2 PROPERTIES OF SAND

The sand in the sandbox is quartz based, but contains many impurities including some larger rocks (0.5" to 1.5" diameter). There appeared to be very little moisture content in the sand as it has been drying for over a year (this was only observed and not measured quantitatively). Several methods were used to find the dielectric of the sand, including measurements of a metal target at a known position, measuring the S-parameters of a sand-filled slotline and backing out the properties of the sand, and employing the mixing formula for powdered rock. The slotline and mixing formulas provided low estimates of the dielectric around 2.5. Multiple measurements of buried targets gave a dielectric on the order of $3 \pm 0.1$. The latter value was used since it was based on actual measurements using the same setup that would later be used for the measurements. The extinction through the sand was low enough that the unknowns in the measurements masked the losses due to extinction.

A number of background measurements of the sand were made in which no targets were buried (these measurements are referred to as scattering measurements in the following sections). This was done to determine the scattering characteristics of

the sand and to identify the strength of the coherent reflection from the sand surface and the radar system. Measurements were taken in the same configuration that would be used to measure targets. The part of the signal that was position dependent (i.e. scattering from the sand) could be separated from internal transients in the measurement system by incoherently and coherently averaging the signals and looking at the difference between these two. Coherent averaging gives the coherent reflections in the system, which do not depend on where the antennas are placed. Incoherent averaging gives the expected total power, which includes both coherent and incoherent components. The difference between these two gives the incoherent part of the signal, which is the scattering energy from the sand. One limitation to this approach comes from the slight variations in the sand surface that were present, coupled with the transients of the horn antenna. Another limitation is that the bar which holds the transmit antenna is bent and the elevation of the transmit antenna changes relative to the receiver antennas by as much as 1.5 cm[12]. Because the bar for holding the transmit antenna is bent and the sand surface is not perfectly flat, variations in the surface reflection will occur since the measurements were taken over a large region in which the surface topology and effective height of the sand varied. It is difficult to differentiate between the variations in the signal responses caused by the transient response of the surface reflection and those due to scattering.

Figure 5-7 shows the expected total energy (incoherent averaged), coherent energy, and their difference (scattered energy). This is from a set of 8 independent measurements (each measurement is taken 30 cm apart in the along-track direction). In this particular example, the transmitter and receiver are 40 cm apart in the cross-track direction. The main-lobe of the direct-path and surface reflections is very coherent across measurements, but the signal in the range bins where the target will reside (around range bins 50-60) has approximately equal energy in its coherent and incoherent components. Because of this, the benefits from subtracting away the coherent part (which would ideally remove the direct-path and surface reflection

[12] This offset was measured and is accounted for in the SAR processing by varying the z-position of the transmit antenna.

energy) will not be as beneficial as hoped for. If the surface variations in the calibration data are enough different from those from the target measurements, the result can actually be made worse.

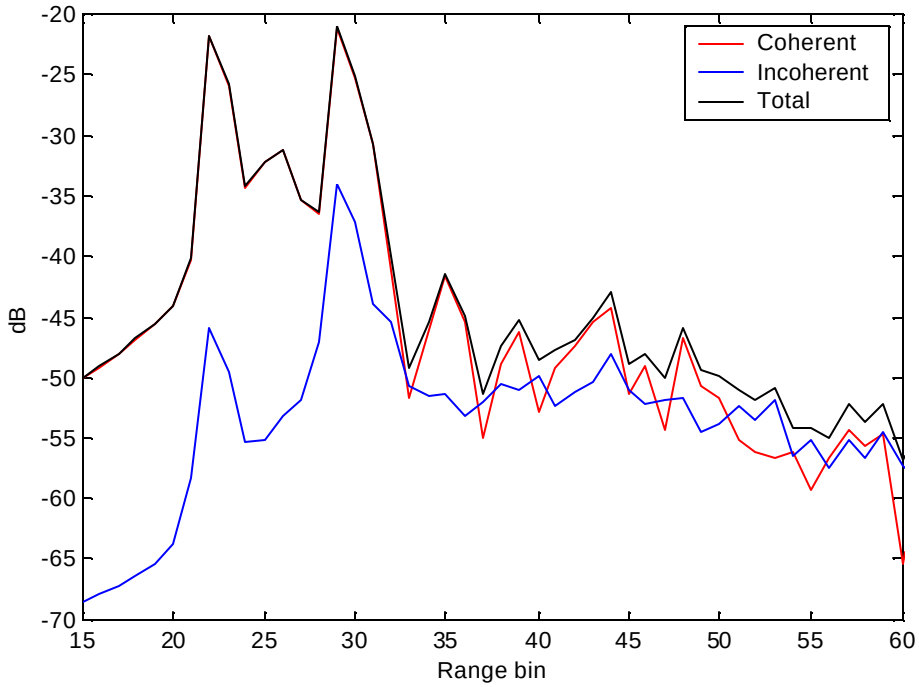


*Figure 5-7: Comparison of scattered energy to coherent energy for a single set of sand scattering measurements (8 independent measurements).*

Figure 5-8 gives the results when two different data sets were combined. Both data sets were taken in the same way except that the second data set is from a different area of the sandbox. One can see that the coherent part is actually significantly weaker in many range bins. The main lobe of the surface reflection also has a strong incoherent component. To combat this problem, several more scattering data sets could be taken and then, instead of subtracting away the energy from an average of the data sets that would tend towards zero energy since they will not line up properly as shown in Figure 5-8, we can use the maximum likelihood filter to project the target measurements into a space orthogonal to these scattering measurements. One could also take the singular value decomposition of the scattering measurements and then choose the largest singular values and project the

target measurements into a space orthogonal only to the parts of the scattering measurements that represent the largest singular values [29]. The second option may be useful if the space spanned by all the scattering measurements includes too much of the target's space. Concerning the MMSE filter, the SNR is very high so the MMSE effectively simplifies to the maximum likelihood filter and the small gain from using the MMSE would most likely not warrant its use.

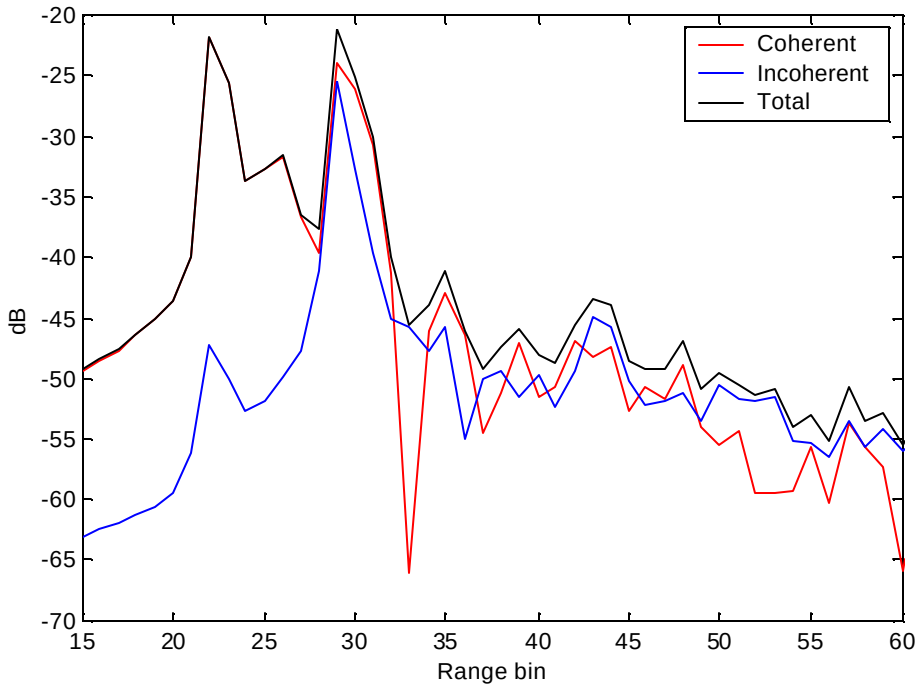


*Figure 5-8: Comparison of scattered energy to coherent energy for both sets of sand scattering measurements (16 independent measurements).*

A measure of the scattering also gives an indication of what the "interference-floor" will be. The targets must be of comparable strength or stronger if matched filtering is applied. Because there is significant side-lobe energy from the surface reflection, the targets should be buried deep enough into the sand to avoid the strongest components of this energy since the primary purpose of these measurements is to test the spatial processing of bistatic data and not the temporal processing.

## 5.3 HORN ANTENNA MEASUREMENT

The antennas used to take the measurements were TEM horn antennas. The dimensions of the horn antennas are given in Figure 5-9. To measure the antennas, the E-plane and H-plane complex radiation patterns were measured. The complex radiation pattern contains both magnitude *and phase* information as a function of angle and frequency. An arbitrary reference point was assigned to the horn antenna as shown in Figure 5-9. The reference point is flush with the horn antenna opening and is in the center of the opening. All measurements will be made with reference to this point.

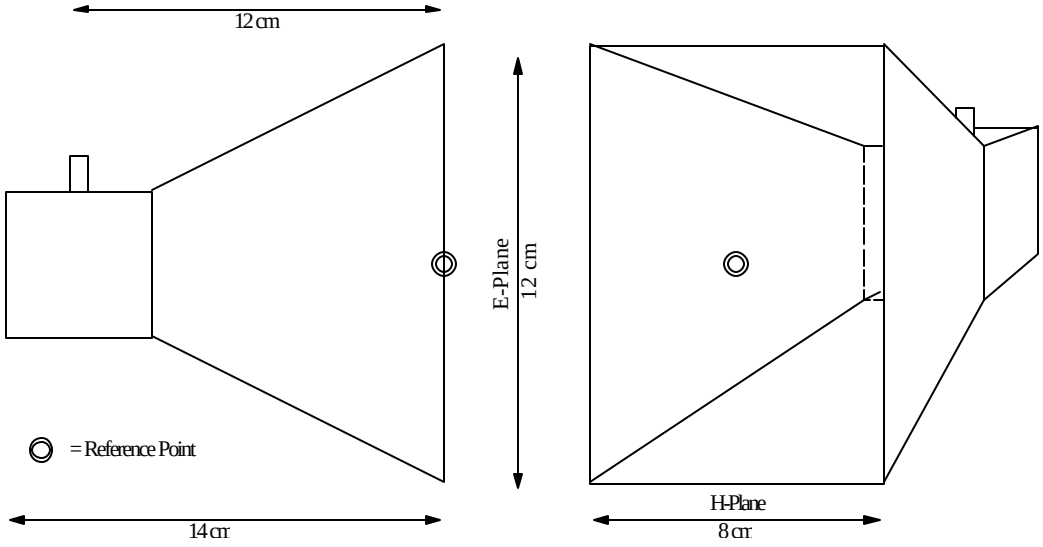


*Figure 5-9: TEM horn antenna dimensions with reference point marked.*

Figure 5-10 shows the measurement setup. Note that the reference point is located at the center of the rotating point. This is done so that the range between the reference points of the antennas does not change for different angular measurements. The e-plane pattern was measured from -90 to +90 degrees in 5-degree increments (total of 37 measurements). The horn antennas were rotated by ninety degrees and the h-plane pattern was then measured for the same angles. The network analyzer was set to measure the horn antenna's response from 2 to 6 GHz. The number of frequency points chosen was set to 1601 points with the appropriate sweep time to

avoid time-domain aliasing problems. The power was set to the maximum recommended level for the network analyzer (-10 dBm for the Hewlett Packard 8722D) to maximize the SNR for a single sweep.

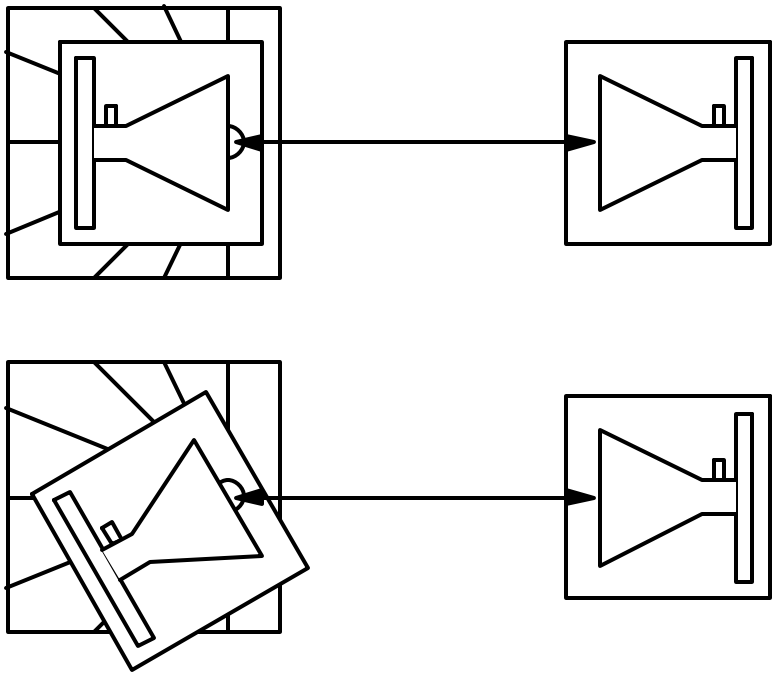

*Figure 5-10: TEM horn antenna measurement setup at two different angles with the range from reference point to reference point marked with a double arrow. Note that the range is the same no matter what angle is chosen.*

The network analyzer was calibrated to the inputs of the horn antenna and three datasets with 100 averages per dataset were taken. The reason for the large number of averages was due to the low maximum power provided by the network analyzer and the desire to capture the full transient response, which has –30 to –40 dB side lobes. The three datasets were used to establish an estimate of the SNR. The resultant SNR is shown in Figure 5-11. This figure shows the estimated minimum SNR and estimated mean SNR found at each range bin across each of the angles that were measured. The main response occurs at range bin 50. This plot shows that the side-lobes following the main response have a mean SNR of over 30 dB, which is sufficient for use in SAR processing and with the exception of range bin 75 and 77, the minimum SNR is over 15 dB for every measurement (nulls occur at these range

bins for certain angles and the minimum SNRs only occur when the range bin represented very small amounts of energy).

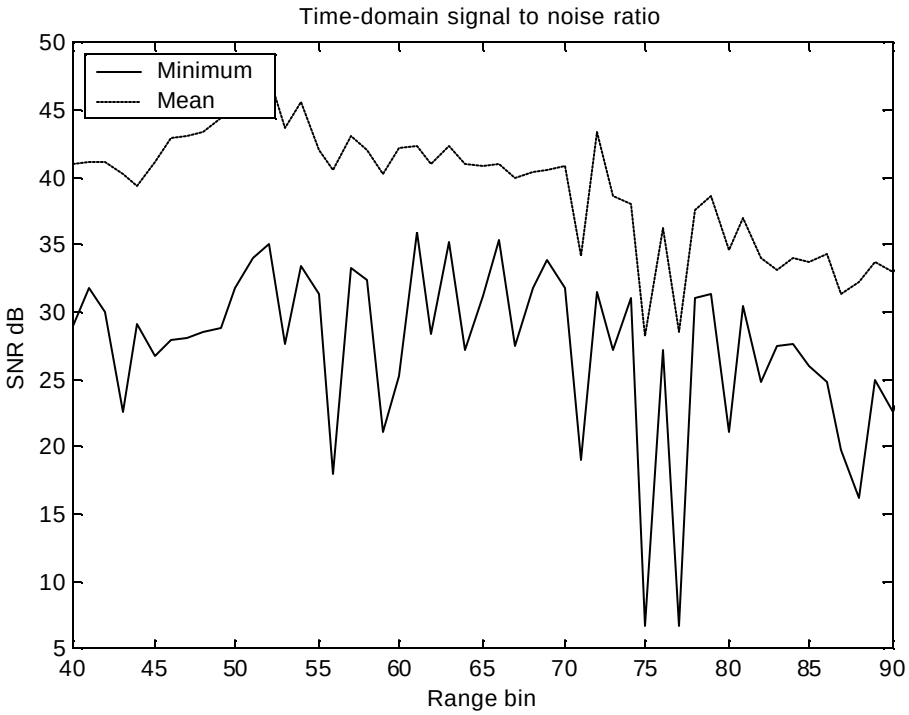


*Figure 5-11: Minimum and average SNR of the first range bins.*

The following steps describe the processing and conditioning of the antenna data to create the final complex radiation patterns that will be used in the system model.

1. Coherently average the three datasets to increase the SNR. Since the standard deviation of the result is unimportant, there is no reason for keeping the datasets separate.

2. The horn antenna data was taken on a cement surface outdoors. There is a significant ground reflection from the cement that needs to be removed. A Butterworth filter was applied in the frequency-domain to remove the ground reflection. A manual search for a good combination of filter width, type and order was made to maximize suppression of the ground reflection, to minimize impact on the direct path, and to keep rounding errors under control.

The final filter was an order $2 \cdot 10 = 20$ band-stop filter. By using a stop band filter, the percentage bandwidth and filter order could be set to best optimize the response while minimizing the rounding errors.

3. The filtering process causes fairly severe transients at the beginning and end of the frequency domain (i.e. around 2 and 6 GHz). To remove the transients, an ideal impulse was passed through the same band-stop filter and the ratio between the expected flat response and the actual response for the ideal impulse was found. These ratios at each frequency became weights that were then multiplied with the filtered horn antenna data. This significantly reduced the transients. This method is described in [30].

4. The antennas were not lined up perfectly, so that the broadside measurement was actually a few degrees off (0.2 degrees for the H-plane measurements and 3.8 degrees for the E-plane measurements). The data was oversampled from $-20$ degrees to +20 degrees of the expected broadside angle using spline interpolation. The angle of maximum power at each frequency was determined. The mean over the frequencies was then taken at each angle and the angle with the maximum mean over all frequencies was chosen as the actual broadside. The data was then resampled at the desired angles using spline interpolation.

5. The expected delay was calculated based on the measured reference point to reference point length. This expected delay was removed from each of the measurements (by phase shifting the frequency domain data).

6. The gain of the antenna was found by solving Friss transmission formula for $G_t$ using the symmetry of the link. Friss transmission formula is:

$$P_r = P_t \frac{G_t}{4\pi R^2} h_{\mathrm{Re}\,ff} A_r \tag{5.8}$$

where each of the terms are defined as in the radar equation (2.5). $R$ is the distance from reference point to reference point. Since $h_{\mathrm{Re}\,ff} A_r = \frac{l^2 G_r}{4p}$ and $G_r = G_t$ we have

$$\frac{P_r}{P_t} = \frac{l^2 G_t^2}{(4pR)^2} \tag{5.9}$$

The $S_{21}$ parameter of the link was measured and $|S_{21}|^2 = \frac{P_r}{P_t}$ so solving for $G_t$ we have:

$$G_t = \frac{4pR|S_{21}|}{l} \text{ or } G_t^{0.5} = \sqrt{\frac{4pR|S_{21}|}{l}} \tag{5.10}$$

Since we are interested in the magnitude response of the system we will use the second equation in (5.10).

7. The e-plane and h-plane patterns were forced to be symmetrical with respect to angle. The horn antennas should be very close to symmetrical. Because of this, any discrepancy was assumed to be an error, and the average between the data taken at $q$ and $-q$ degrees from broadside were coherently averaged and the result was used for $\pm q$ .

8. To force the e-plane and h-plane measurements to coincide at broadside, the two broadside measurements were coherently averaged. For the e-plane, the ratio between the coherently averaged result and the original broadside measurement was multiplied with all the measurements. The same was done for the h-plane. At broadside, this has the effect of changing the actual measured result to the coherently averaged result so that both the e-plane and h-plane at broadside match as desired.

9. The average phase delay at broadside was determined. Since the horn antennas are symmetrical, each should have contributed to the phase delay the

same amount. Note that this average phase delay does not include the delay from reference point to reference point since this was already removed.

10. For the e-plane data, the delay found for the e-plane broadside measurement was removed and half the average phase delay at broadside was added. For the broadside measurement, this should have the effect of halving the average phase delay. For off-broadside data the result is to keep the phase difference between the measurement and the broadside measurement the same as it was originally. The reason the *phase difference* is not halved is because only one of the antennas was rotated and therefore all of the phase delay in addition to the broadside delay should have come from changing the direction of the antenna.

11. The data was then truncated in the time domain from 1601 points to 401 points. This will decrease the data processing time, without significantly affecting the results. Since the original data used 1601 data points we have avoided potential time-domain aliasing errors. The truncation is a simple boxcar from time bin –200 to +199 range bins (this was done to capture both sides of the impulse response for reasons similar to those when creating a finite impulse response filter using the window design technique).

12. The last step shaped the data into a table for fast lookup during SAR-processing. The table is a three dimensional array with frequency, elevation angle, and azimuth angle indexing. The table lookup for a particular frequency involves a two-dimensional linear interpolation where the elevation angle and azimuth angle are the inputs to the two-dimensional linear interpolation. Since the data points in the frequency domain are the same as those in the table there is no need for interpolation between frequencies.

The results from these processing steps are illustrated in Figure 5-12 through Figure 5-16. The elevation angle used in the figures is in reference to how the antennas are operated in the sandbox. The horn antennas are facing downward and therefore broadside is at an elevation angle of 180 degrees and 90 degrees points

parallel to the sand surface. Figure 5-12 and Figure 5-13 give the complex radiation pattern at 4 GHz. Figure 5-14 and Figure 5-15 give the complex frequency response for broadside. The delay plots in Figure 5-13 and Figure 5-15 are just a phase shift converted to a relative group delay and then converted to an equivalent free-space length. This was done to better illustrate the effect of the phase shifts. Finally, Figure 5-16 gives the transient response at broadside (essentially just the Hanning windowed IFFT of the results displayed in Figure 5-14 and Figure 5-15).

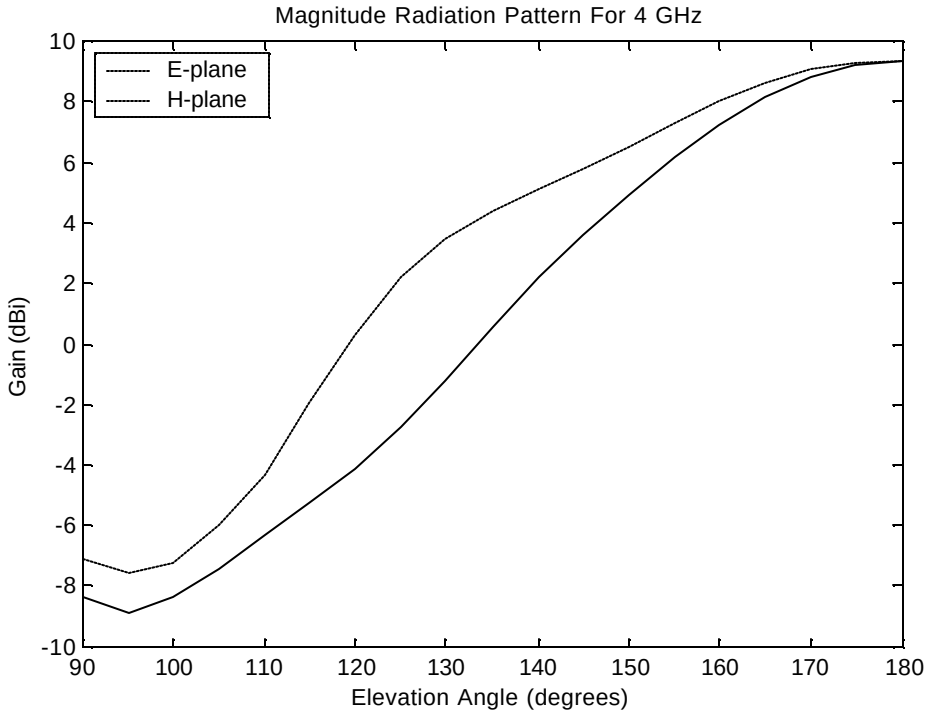


*Figure 5-12: E-plane and H-plane magnitude beam patterns at 4 GHz. Elevation angle is measured with the z-axis decreasing toward nadir.*

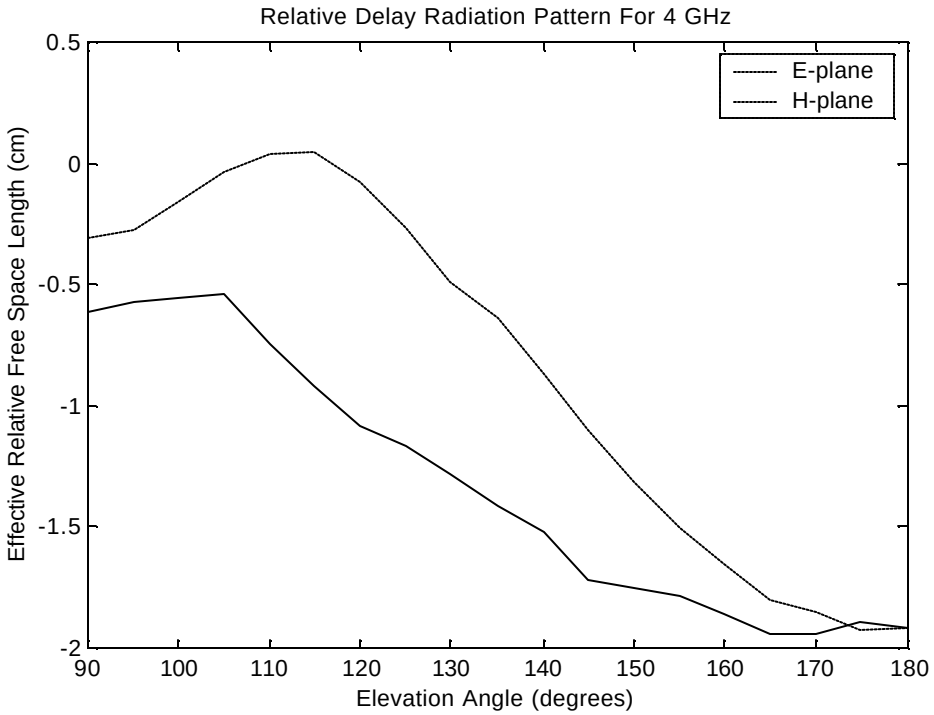


*Figure 5-13: E-plane and H-plane delay patterns at 4 GHz. Elevation angle is measured with the z-axis decreasing toward nadir.*

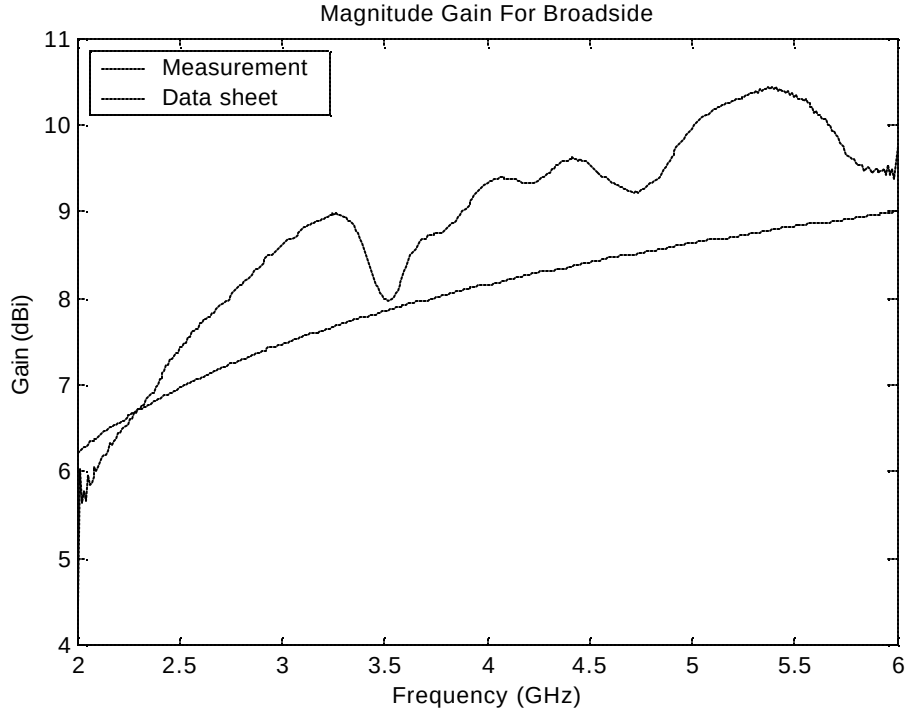


*Figure 5-14: Broadside gain (elevation angle equals 180 degrees).*

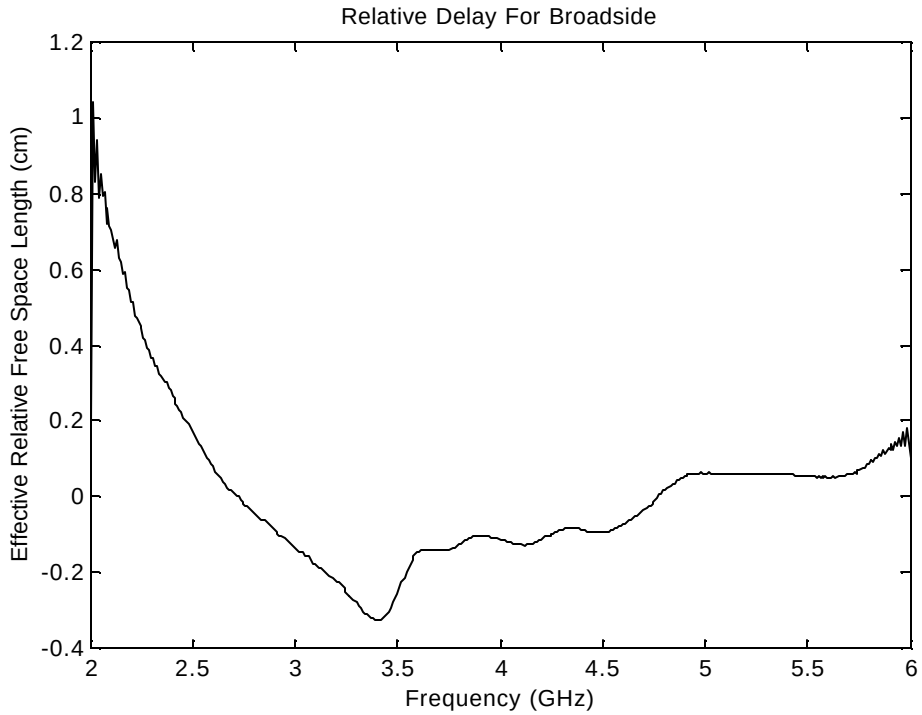


*Figure 5-15: Broadside delay (elevation angle equals 180 degrees).*

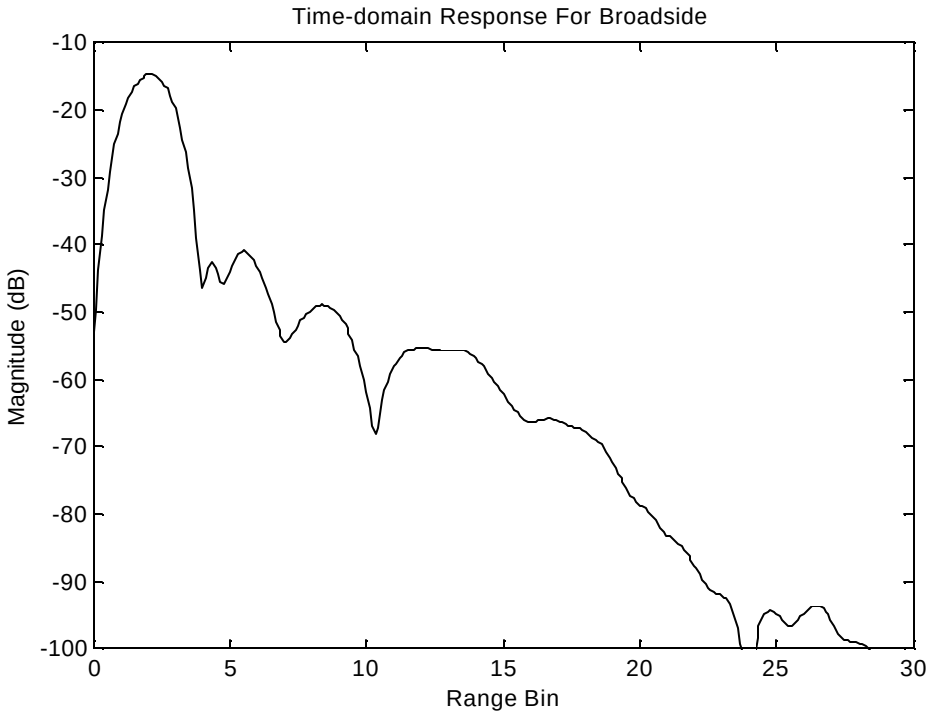


*Figure 5-16: Broadside transient response with hanning window applied (elevation angle equals 180 degrees).*

The transients from the direct path signal were measured by performing a sky-shot. Data was taken over a large region to get a sufficiently large set of independent measurements. The incoherent, coherent, and total energy is plotted in Figure 5-17 for a separation of 40 cm. The results have been time–gated to remove the ceiling reflection at range bin 115 (time-gating is done with a zero phase Butterworth filter by using Matlab's filtfilt command).

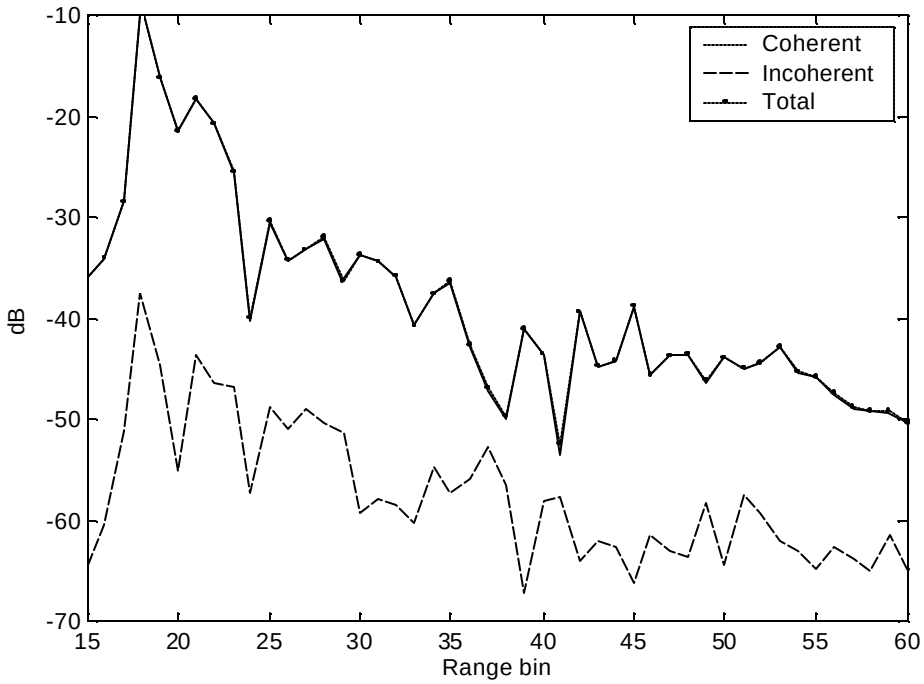


*Figure 5-17: Comparison of scattered energy to coherent energy.*

The coherent component of the signal is very strong as expected. This is because the scene contains no position-dependent scatterers (ideally). Since the sky measurements have a high degree of coherence, the sky measurements were subtracted from the data before processing in the final measurement.

Another consideration concerning the horn antenna was the location of the far-zone. Figure 5-18 plots the far zone over the system bandwidth as given by equation (5.11) [25].

$$R_{far-zone} \geq \frac{2d_a^2}{l} = \frac{2}{l}\underbrace{\max}_{x_a, y_a}\left\{x_a^2 + y_a^2\right\} = \frac{2f\left(0.12^2 + 0.08^2\right)}{c} \tag{5.11}$$

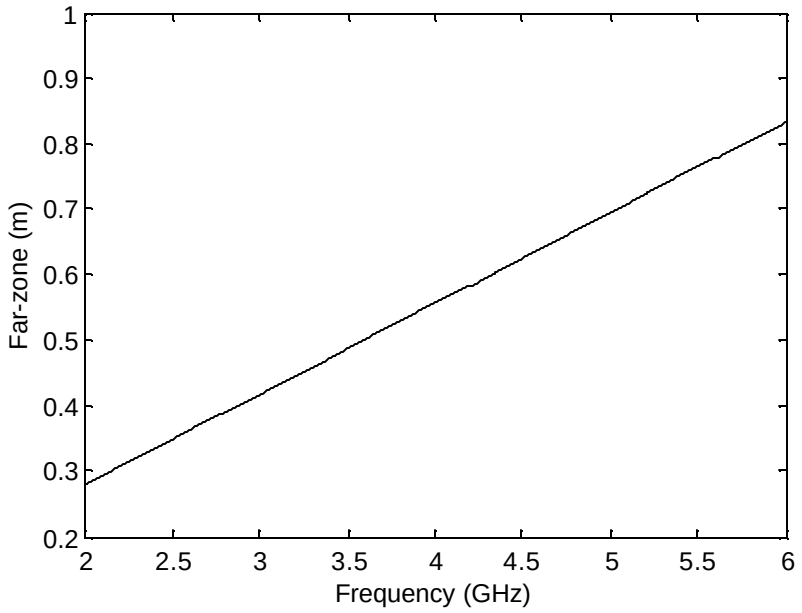


*Figure 5-18: Far-zone calculation for TEM-horn antennas.*

Figure 5-18 suggests that the targets be at least 83 cm from the antennas to satisfy the far-zone requirements at all frequencies. Also, to avoid direct coupling between the antennas and the sand surface, the horn antennas should be placed as far from the surface as possible. The impedance match of the TEM horn antennas have been optimized for an air-interface with an intrinsic impedance of $h_{air} = \sqrt{\frac{m_0}{e_0}} \approx 377\ \Omega$. Measurements in the GPR lab showed that placing the horn antenna too close to the sand caused significant ringing and changes in the antenna's input impedance.

As explained in section 5.2 above, the long transient response of the horn antenna suggests burying the targets well beneath the sand surface. Another reason for doing this is that the SAR aperture can be made larger if the range to the targets increases. If the targets are placed to close to the antennas (near-zone effects not

withstanding), the horn antenna's own radiation pattern is so narrow that no improvement can be made by using SAR processing.

The final measurements were made with the horn antenna placed 40 cm above the surface, which was as high as they could be placed, and the targets were buried approximately 50 cm in the sand, which satisfies the far-zone requirement, allows for a large SAR gain, and lies outside the strongest portions of the surface reflection.

To test the accuracy of the phase measurements, measurements were taken in the sandbox with a metal sheet resting on the ground. The metal sheet should allow the determination of the specular point very precisely, with no energy coming from other targets. The predicted response for antenna separations between 10 and 70 cm were found to be within a twentieth of a range bin. With 4 GHz of bandwidth, this is equivalent to 0.5 cm path length accuracy.

## 5.4 AMPLIFIER MEASUREMENT

As mentioned in section 5.1.1 above, the amplifier and the cable connecting to the horn antenna were not included in the calibration. The S-parameters for the amp and cable were measured separately (see Figure 5-3 above and Figure 5-19 through Figure 5-22).

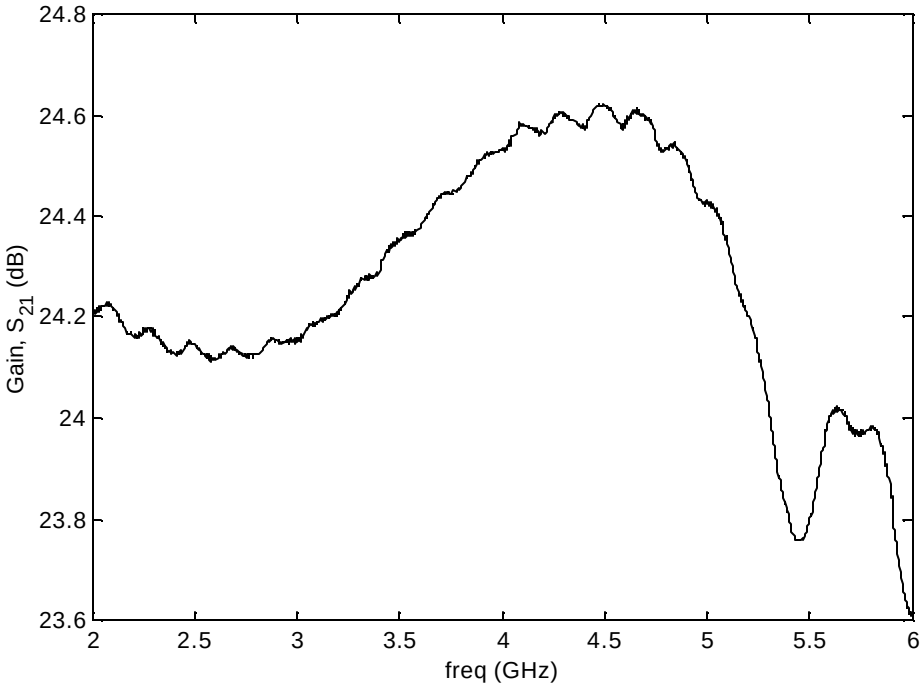


*Figure 5-19: Gain ($S_{21}$) of the amplifier and cable assembly.*

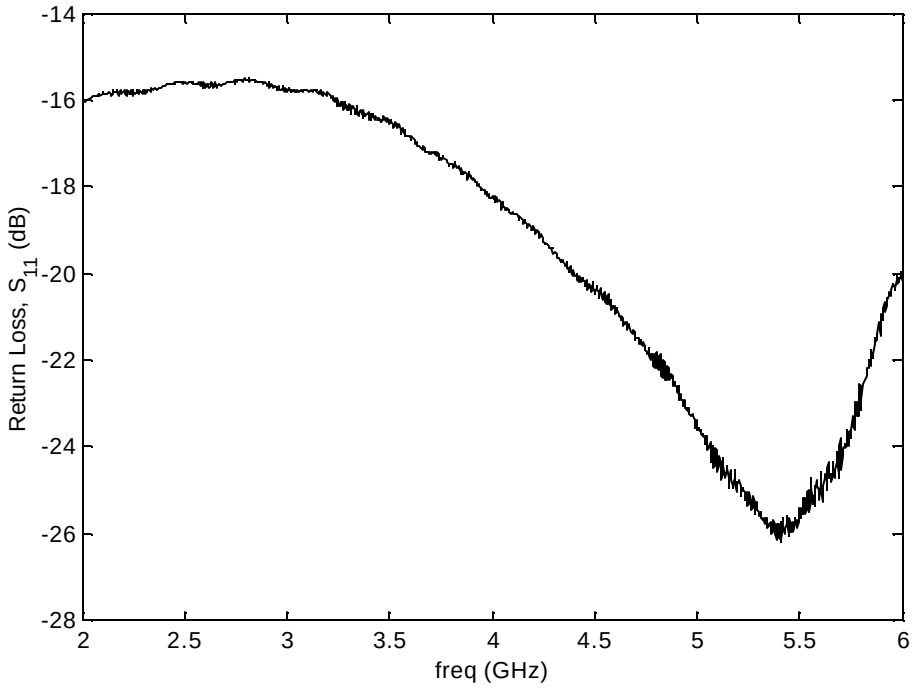


*Figure 5-20: Return loss from port 1 ($S_{11}$) of the amplifier and cable assembly.*

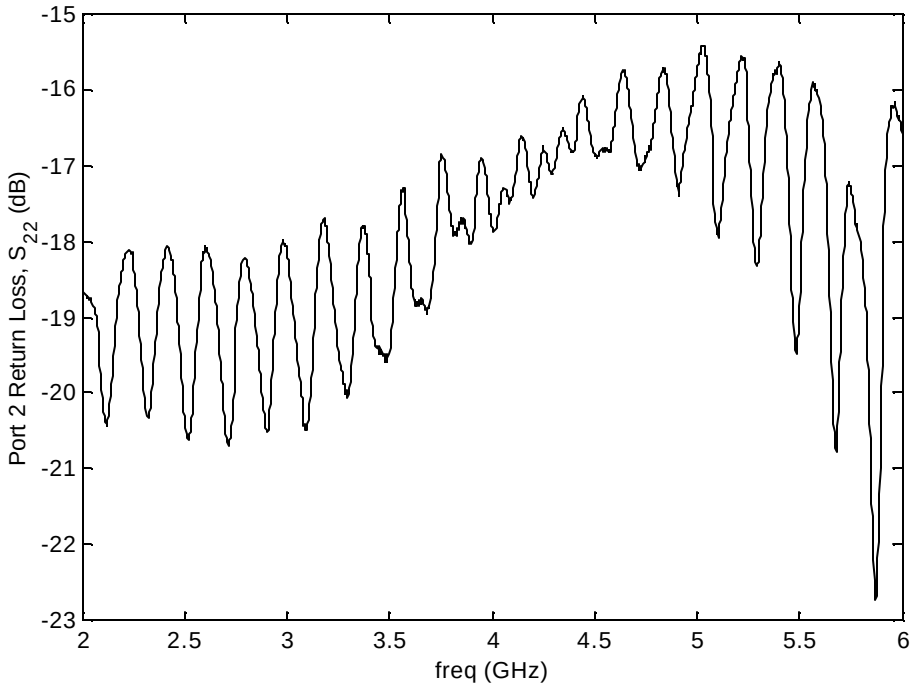


*Figure 5-21: Return loss from port 2 ($S_{22}$) of the amplifier and cable assembly.*

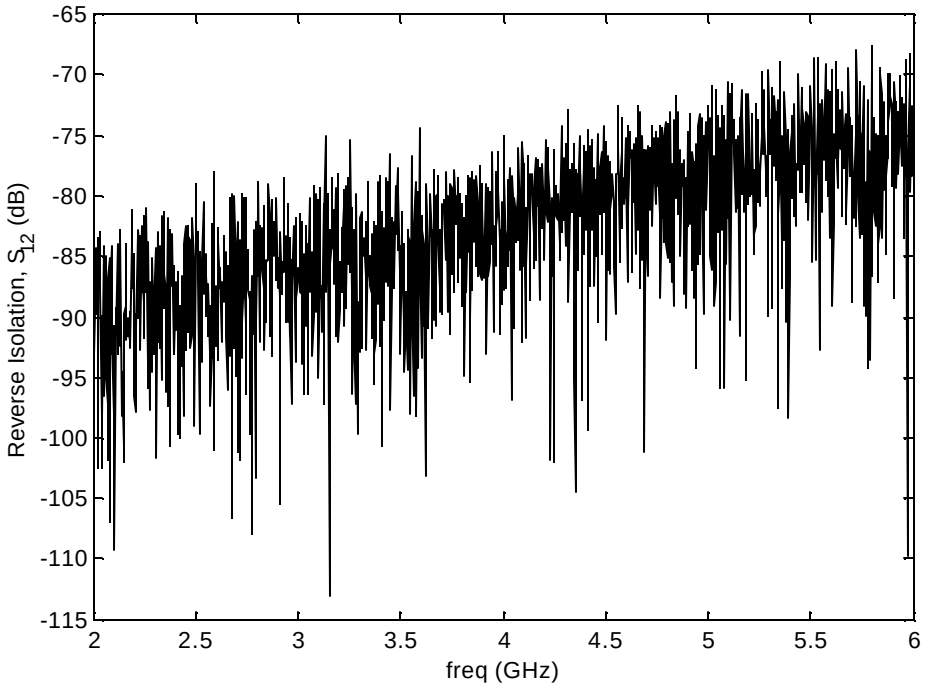


*Figure 5-22: Reverse isolation ($S_{12}$) of the amplifier and cable assembly.*

To include the effect of the amp and cable in the system model, the $S_{21}$ parameter was multiplied with the transmit antenna pattern (similar to multiplying the transfer function of these two devices). This does not completely account for the amp and cable. Reflections between the horn antenna input and the amplifier-cable assembly output are not considered (other reflections will not be significant because of the reverse isolation of the amplifier is around 80 dB). To verify that the reflections between the amplifier and horn antennas are small, the complete system was modeled using the S-parameter data from the amplifier/cable and the S-parameter data taken from the broadside horn antenna measurements. Only $S_{11}$ and $S_{21}$ data were available for the antenna link. However, since the test antenna link was reciprocal, the S-parameter network can be written as $\begin{bmatrix} S_{11} & S_{12} \\ S_{21} & S_{22} \end{bmatrix} = \begin{bmatrix} S_{11} & S_{21} \\ S_{21} & S_{11} \end{bmatrix}$. The S-parameters from the amplifier/cable and horn antenna were converted to transmission parameters; the two transmission matrices were multiplied and then converted back to S-parameters. In Figure 5-23, the final $S_{21}$ parameter is compared to the $S_{21}$ parameter found by just multiplying the two S-parameters as explained above.

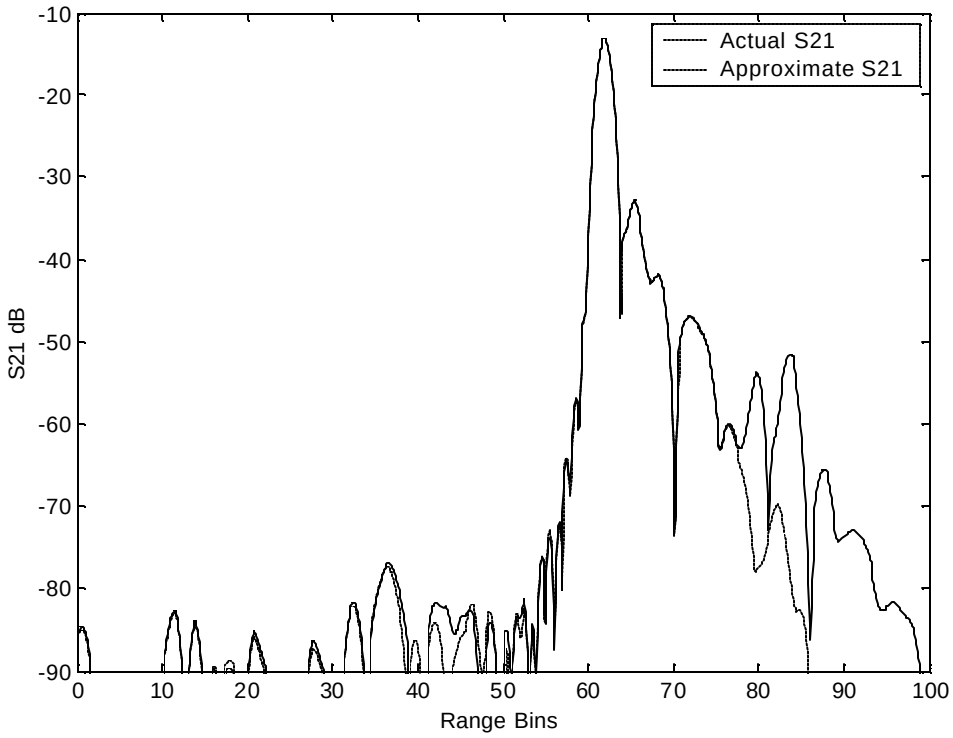


*Figure 5-23: Comparison of actual $S_{21}$ parameter with approximated $S_{21}$ parameter with Hanning window applied.*

A reflection is present (range bin 80), but is 38.5 dB lower than the original. Since this is weaker than the target signal energy we have chosen to ignore it. If better suppression of the reflection was needed, then an attenuator pad could be placed between the amplifier and the horn antenna. Note that the return loss of the attenuator would need to be over 20 dB plus the attenuator loss to see any improvement; otherwise the reflections off the attenuator will create the same problem as before, only with lower SNR and the same (or worse) unwanted transients.

## 5.5 SIMULATIONS AND MEASUREMENTS

Three different scenes were simulated and measured. Both the simulated and measured results are SAR processed. The three different scenes considered are a

metal covered poster tube, an air-filled poster tube, and a scene with ten spherical targets (four Styrofoam spheres and six metal covered spheres). The tubes were used so that the SAR processing could be done in just the cross-track direction to expedite the testing process. Since the cross-track processing is the part of the algorithm that deals with the bistatic movement (receiver moving while transmitter remains stationary), a situation in which only the cross-track direction needed to be considered rather than both the along-track and cross-track was desired. The tubes were aligned so that the target looked like a flat plane in the along-track profile and a sphere in the cross-track profile. This is shown in Figure 5-24.

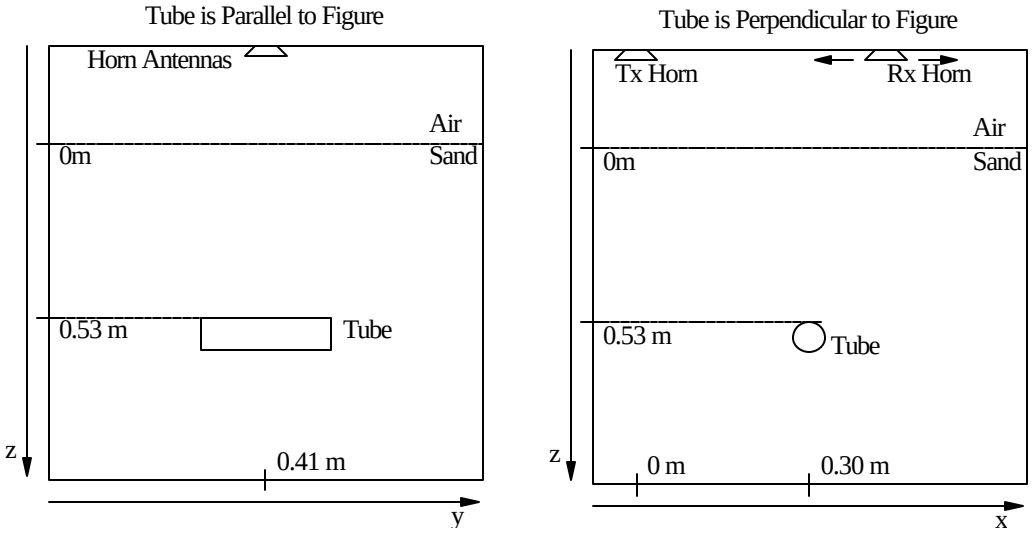


*Figure 5-24: Alignment and positioning of tube for both the metal covered tube and the air-filled tube measurements.*

In the along-track direction the tube appears as a flat surface and hence appears specular with the scattered energy largest when the antennas are aligned with the tube in the along-track direction (y = 0.41 m). For the cross-track case, it was desired to test the SAR processing so the ideal target would be an isotropic scatterer in this direction. A metal sphere very closely approximates an ideal isotropic scatterer. A tube, aligned perpendicular to the cross-track/depth plane, also provides this behavior as long as the measurements are restricted to the cross-track/depth plane.

The final measurement with ten targets was to test the whole processing algorithm. Because of this, spherical targets were used which are truly isotropic so that along-track and cross-track processing could be performed.

### 5.5.1 METAL COVERED TUBE

The target to be measured was a metal covered tube. The tube is 2.5 in (6.35 cm) in diameter, 12.5 in (31.75 cm) long. It was buried 53 cm in the sand (z = -53 cm) measured from the sand surface to the top of the tube, at a cross-track location of x = 30 cm and an along-track location of y = 20 cm. Both the cross-track and along-track locations are relative to the center of the tube. In the simulation, the scene was approximated by a collection of point targets as shown in Figure 5-25. The tube is simulated by a semicircle because the bottom of the tube is not illuminated since all the energy is reflected off the top of the tube.

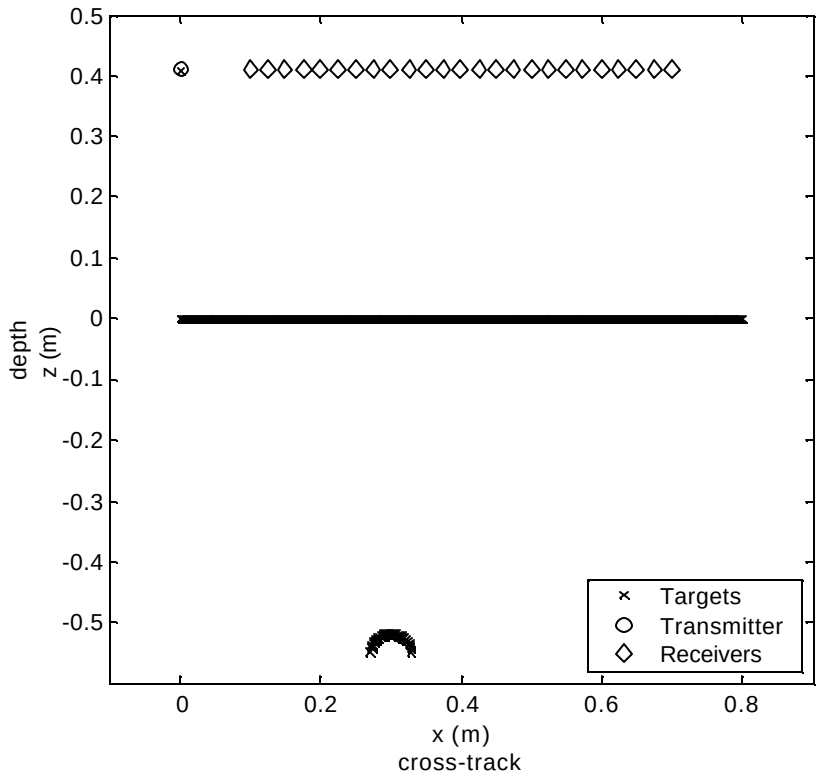


*Figure 5-25: Location of point targets for metal tube simulation.*

The point targets were closely spaced to imitate a contour rather than discrete point scatterers. The target weights were real and set so that the power levels of the simulated figure matched the power levels of the measured data. Currently the system model does not include information about the type of target and therefore a reflectivity or bistatic cross-section cannot be determined and must be assigned. The simulated response and raw measurements are shown in Figure 5-26 and Figure 5-27 respectively. The SAR-processed results are shown in Figure 5-28 and Figure 5-29 using the simulated and measured data respectively. The SAR-processed results have been thresholded so that signal levels beneath those indicated on the color bar are set to the minimum value. A set of scatter measurements (i.e. no target as described in section 5.2 above) were taken at similar positions as for this measurement and these were used to subtract away the surface response in the measured dataset. This is why the surface response is so weak in Figure 5-29.

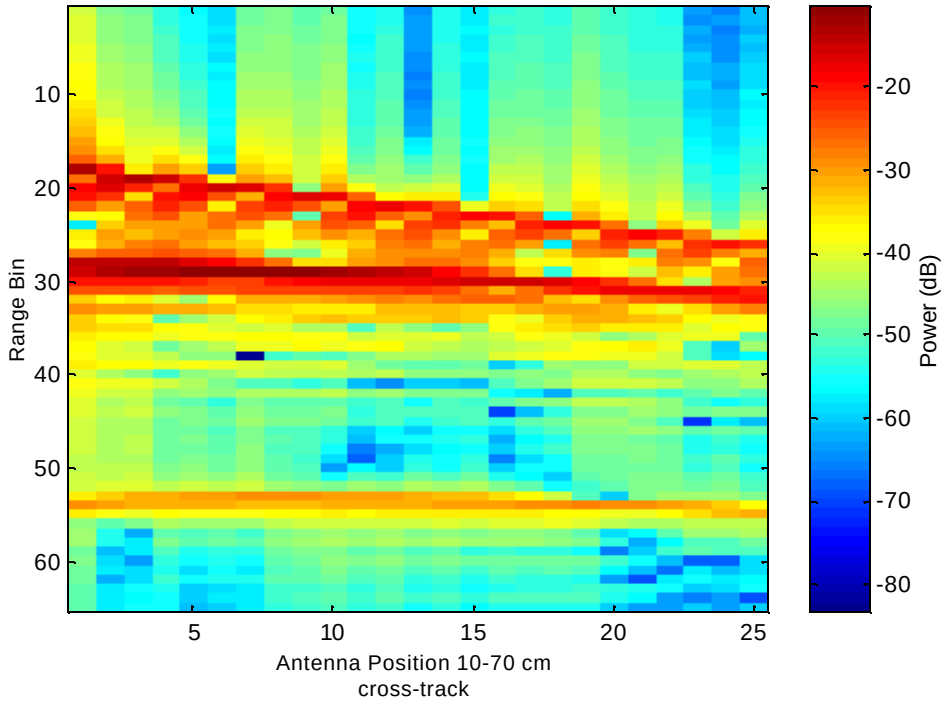


*Figure 5-26: Simulated data for metal-covered tube along the y = 0.41 m transect. The target response is in range bins 53-55.*

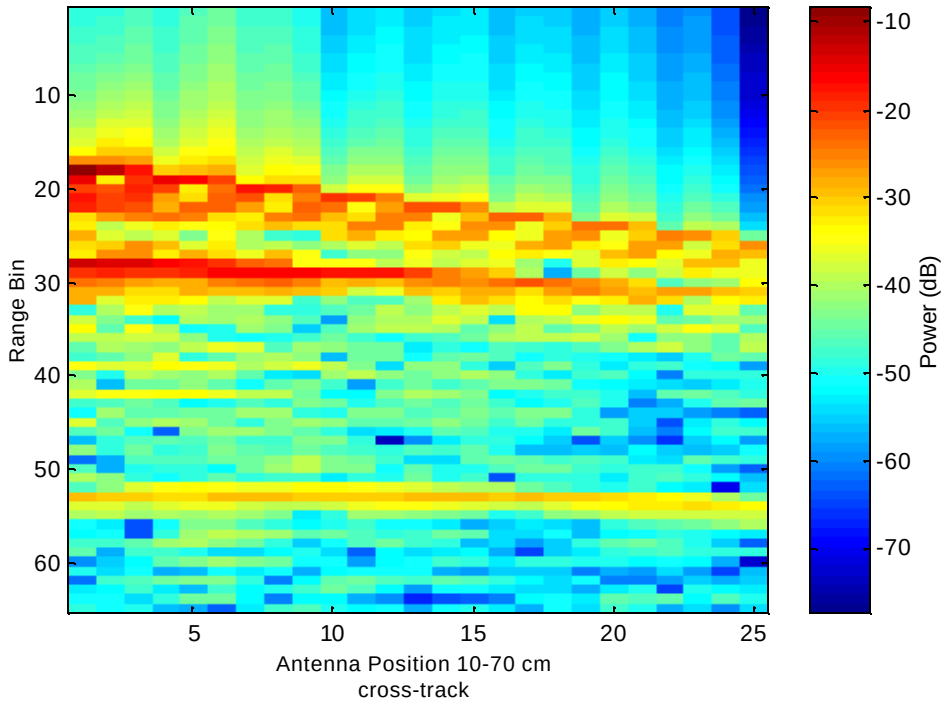


*Figure 5-27: Raw measurements for metal-covered tube along the y = 0.41 m transect. The target response is in range bins 53-55.*

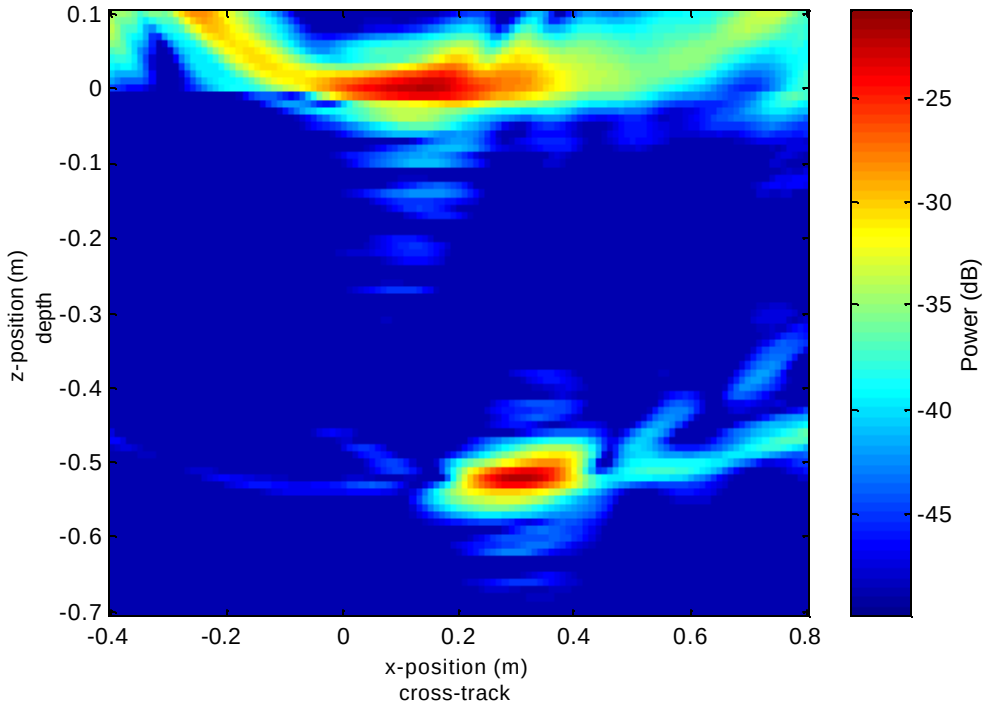


*Figure 5-28: SAR processed results of simulated data for the metal covered tube.*

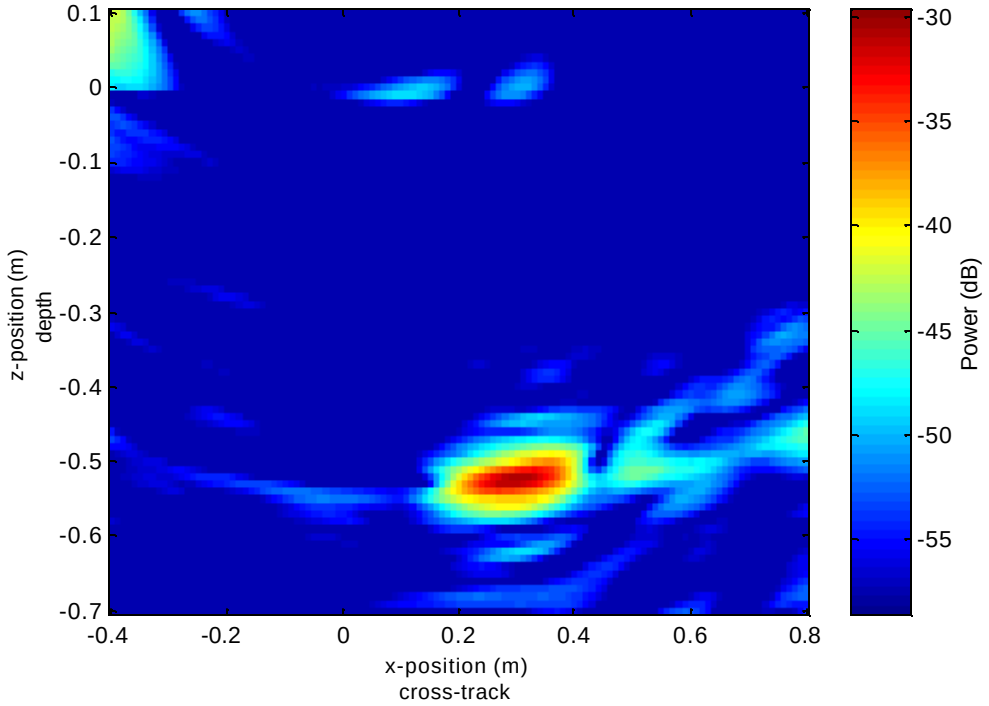


*Figure 5-29: SAR processed results of measured data with the surface response subtracted away for the metal covered tube.*

The SAR-processed results for the measured data have a target signal to side-lobe level of 16 dB. This high signal energy is expected as the metal interface provides a very strong reflection that can clearly be seen in the raw data, which itself has a signal to side lobe ratio of 10 dB. The position of the target, determined by finding the point with the maximum response is x = 0.295 m and z = 0.50 m.

### 5.5.2 AIR-FILLED TUBE

In this section, the target to be measured is an air-filled tube. The tube is 2.5 in (6.35 cm) in diameter, 12.5 in (31.75 cm) long. It was buried 53 cm in the sand (z = -53 cm) measured from the sand surface to the top of the tube, at a cross-track location of x = 30 cm and an along-track location of y = 41 cm. Both the cross-track and along-track locations are relative to the center of the tube. In the simulation, the scene was approximated by a collection of point targets as shown in Figure 5-30. The

air-filled tube is simulated by a full circle since only part of the wave is reflected at the top interface, allowing the bottom of the tube to be illuminated.

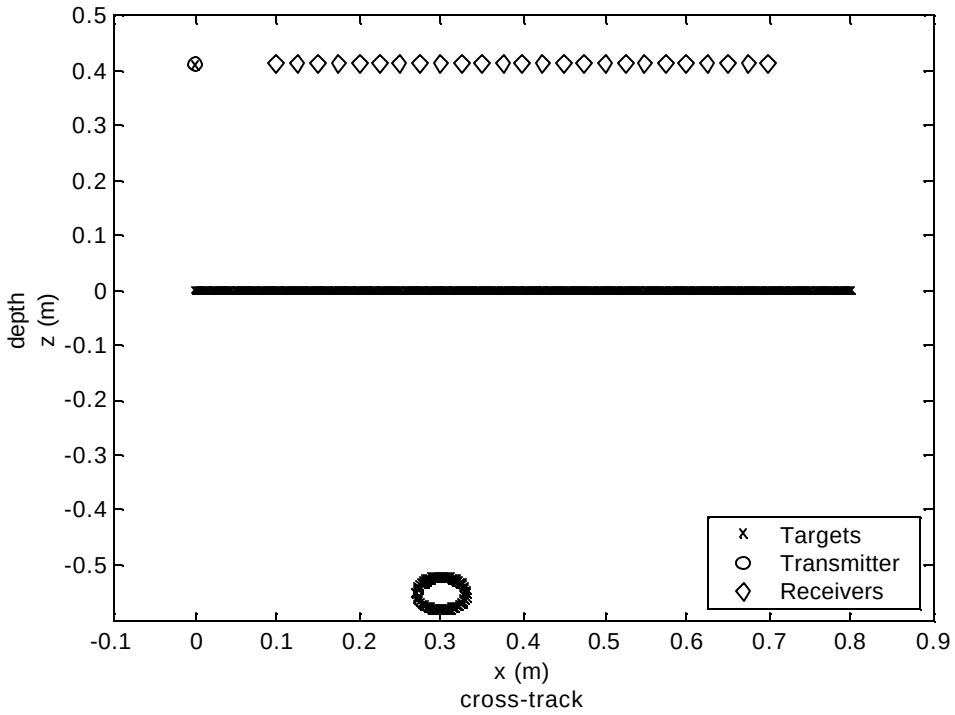


*Figure 5-30: Location of point targets for air-filled tube simulation.*

The point targets were closely spaced to imitate a contour rather than discrete point scatterers. The simulated response and raw measurements are shown in Figure 5-31 and Figure 5-32 respectively. The SAR-processed results are shown in Figure 5-33 and Figure 5-34 using the simulated and measured data respectively. The SAR-processed results have been thresholded so that signal levels beneath those indicated on the color bar are set to the minimum value. A set of scatter measurements (i.e. no target as described in section 5.2 above) were taken at similar positions as for this measurement and these were used to subtract away the surface response in the measured dataset. This is why the surface response is so weak in Figure 5-34.

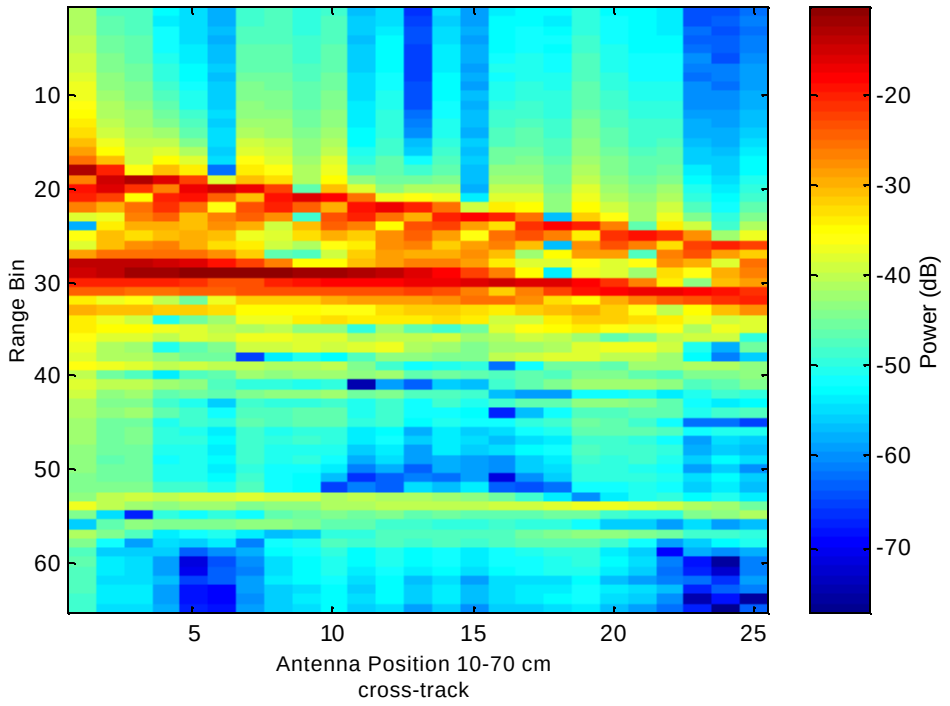


*Figure 5-31: Simulated data for the air-filled tube along the y = 0.41 m transect. The target response is in range bins 53-55.*

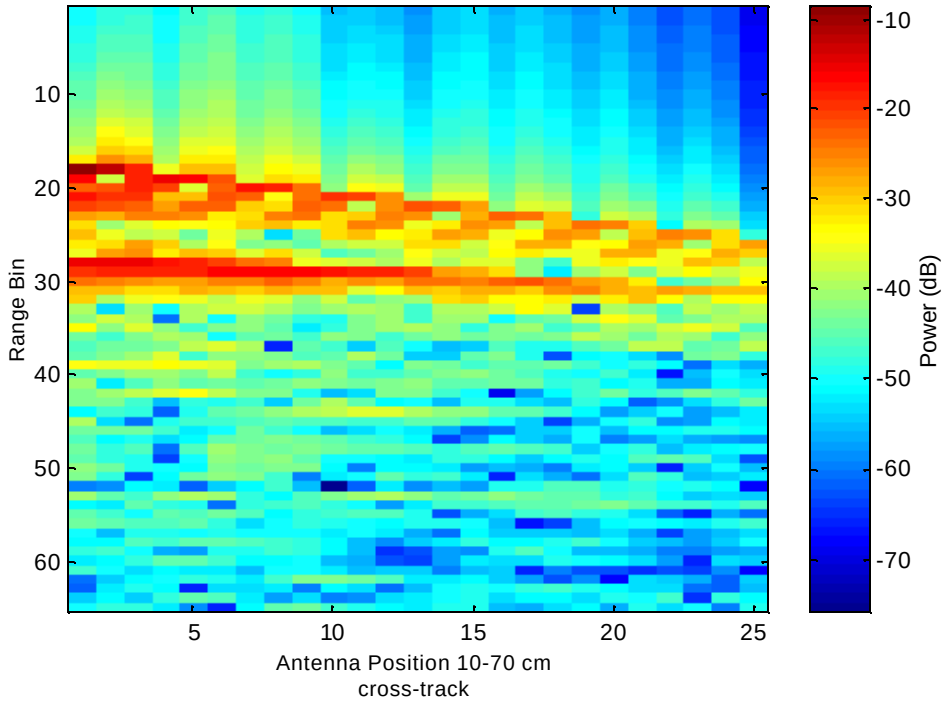


*Figure 5-32: Raw measurements for the air-filled tube along the y = 0.41 m transect. The target response is in range bins 53-55.*

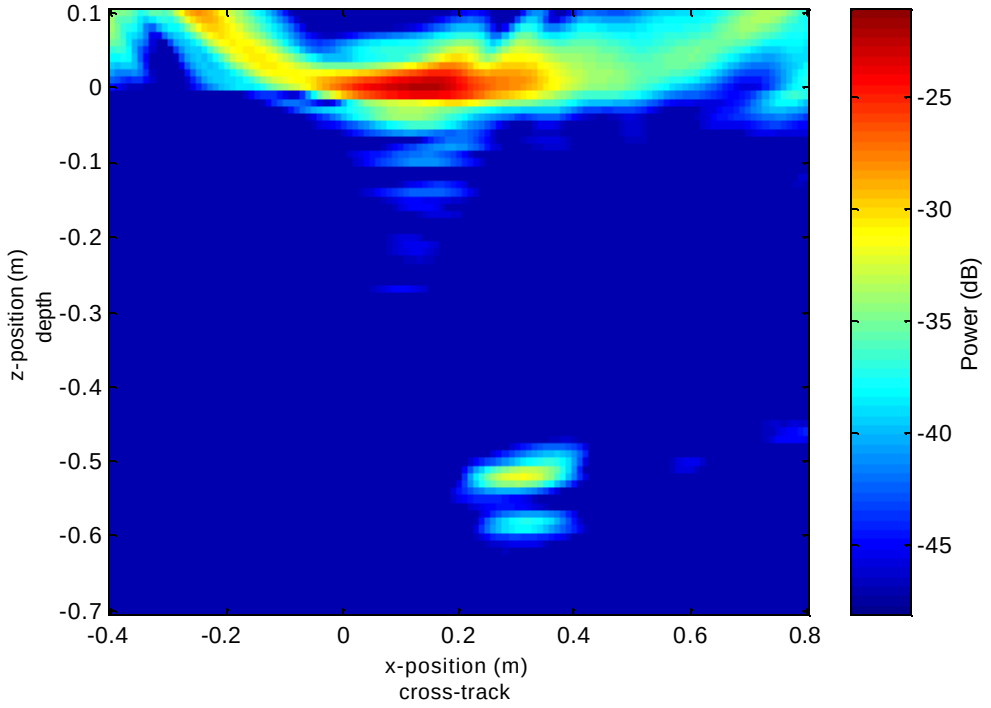


*Figure 5-33: SAR processed results of simulated data for the air-filled tube.*

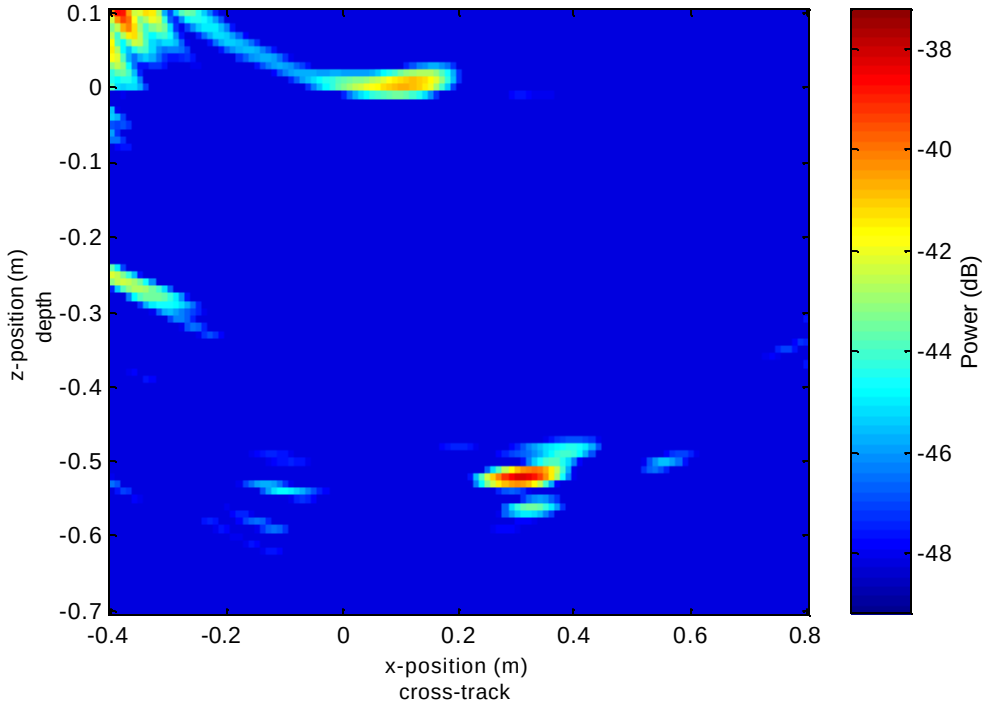


*Figure 5-34: SAR processed results of the measured data with the surface subtracted away for the air-filled tube.*

The SAR-processed results for the measured data have a target signal to side-lobe level of 7 dB. This is expected to be lower than the metal covered tube because the sand-air dielectric interface will cause much smaller reflections than the sand-metal interface will. This can be seen in the raw data, which has a signal to side lobe ratio of 3 dB. The position of the target was found to be x = 0.305 m and z = 0.52 m. Because the tube is hollow, both the front and back of the tube create reflections, hence resembling two closely spaced targets.

### 5.5.3 BED OF TEN TARGETS (METAL AND AIR-FILLED)

The final measurement consisted of ten targets as described in Table 5-1. The targets were all spheres with varying diameters as indicated in the table. The metal spheres were Styrofoam balls with aluminum foil wrapped tightly over the top two thirds of the sphere. The air filled spheres were either Styrofoam or paper machete. The actual target positions indicated in the table are $x$ and $y$. All targets were buried 50 cm in the sand. The target positions given by $x$ and $y$ are only approximations, but are probably within 0.05 m of the actual position. The target positions determined from the SAR processed image are $\hat{x}$ and $\hat{y}$. The peak signal level obtained from SAR-processing has also been included for each target.

*Table 5-1: Ten targets buried in sandbox (wavelength in sand at 4 GHz is 4.3 cm).*

| Target | Diameter | Metal/Air | $x$ | $y$ | $\hat{x}$ | $\hat{y}$ | Signal Power |
|---|---|---|---|---|---|---|---|
| 1 | 12.5 cm | Metal | 0.34 m | 0.22 m | 0.36 m | 0.22 m | -35 dB |
| 2 | 10 cm | Metal | -0.07 m | 0.64 m | -0.12 m | 0.64 m | -38 dB |
| 3 | 12.5 cm | Metal | 0.64 m | 0.64 m | 0.64 m | 0.66 m | -35 dB |
| 4 | 10 cm | Metal | 0.07 m | 1.11 m | 0.08 m | 1.12 m | -42 dB |
| 5 | 10 cm | Metal | 0.50 m | 1.10 m | 0.51 m | 1.12 m | -40 dB |
| 6 | 10 cm | Metal | 0.09 m | 1.65 m | 0.06 m | 1.66 m | -42 dB |
| 7 | 11.5 cm | Air-filled | 0.52 m | 1.67 m | 0.54 m | 1.68 m | -53 dB |
| 8 | 15 cm | Air-filled | -0.04 m | 2.15 m | -0.10 m | 2.14 m | -49 dB |
| 9 | 11.5 cm | Air-filled | 0.64 m | 2.15 m | 0.64 m | 2.16 m | -52 dB |
| 10 | 15 cm | Air-filled | 0.34 m | 2.57 m | 0.34 m | 2.58 m | -49 dB |

The targets positions have been plotted in Figure 5-35 for illustration and comparison to the SAR processed result given in Figure 5-39.

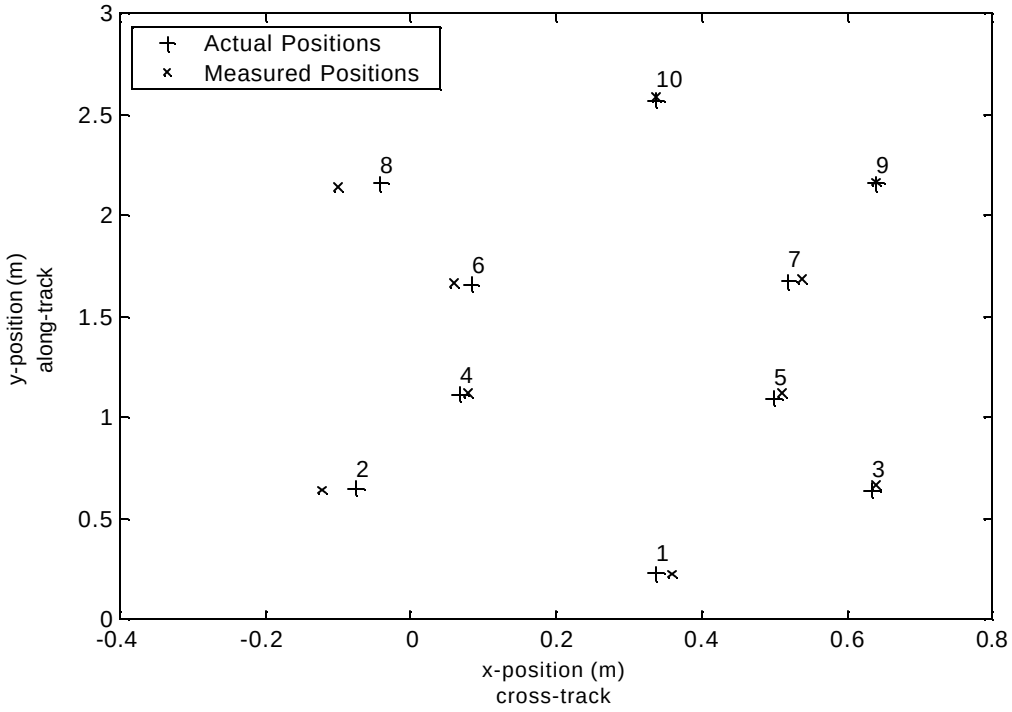


*Figure 5-35: Position of the targets buried in the sand.*

In this final measurement, the simulations were used to suggest a minimum separation of targets that could be resolved using SAR-processing. Figure 5-36 through Figure 5-38 shows the SAR-processed results of two spherical targets with diameters of 15 centimeters placed 0.2 m, 0.3 m, and 0.4 m apart. Note that at 0.2 m, the two targets have merged. With a spacing of 0.3 m and 0.4 m, the two target main lobes have separated and can easily be distinguished. This guideline was followed when choosing the target positions. Targets 4 and 5 and targets 6 and 7 are separated by 0.43 m and are easily resolved after SAR-processing.

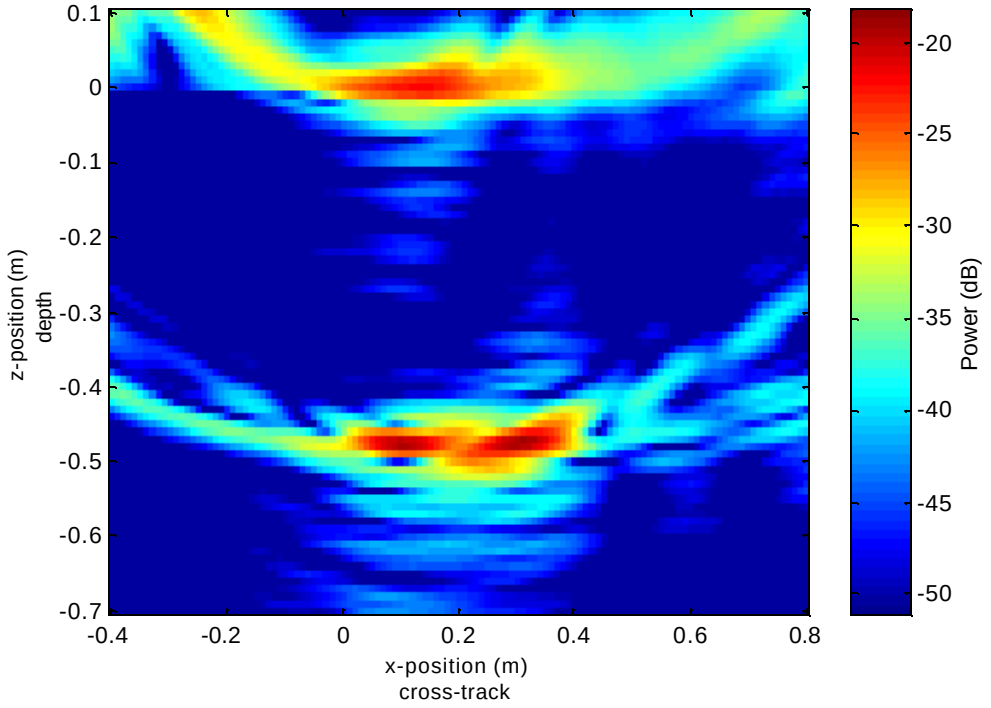


*Figure 5-36: SAR processed image of two simulated targets that are 0.2 m apart.*

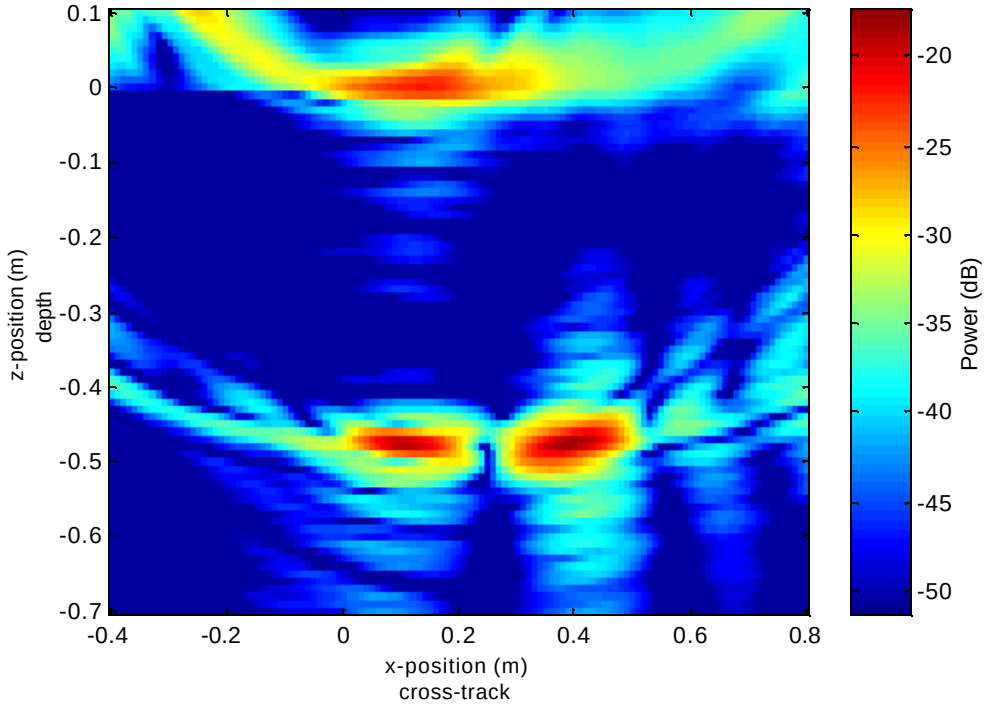


*Figure 5-37: SAR processed image of two simulated targets that are 0.3 m apart.*

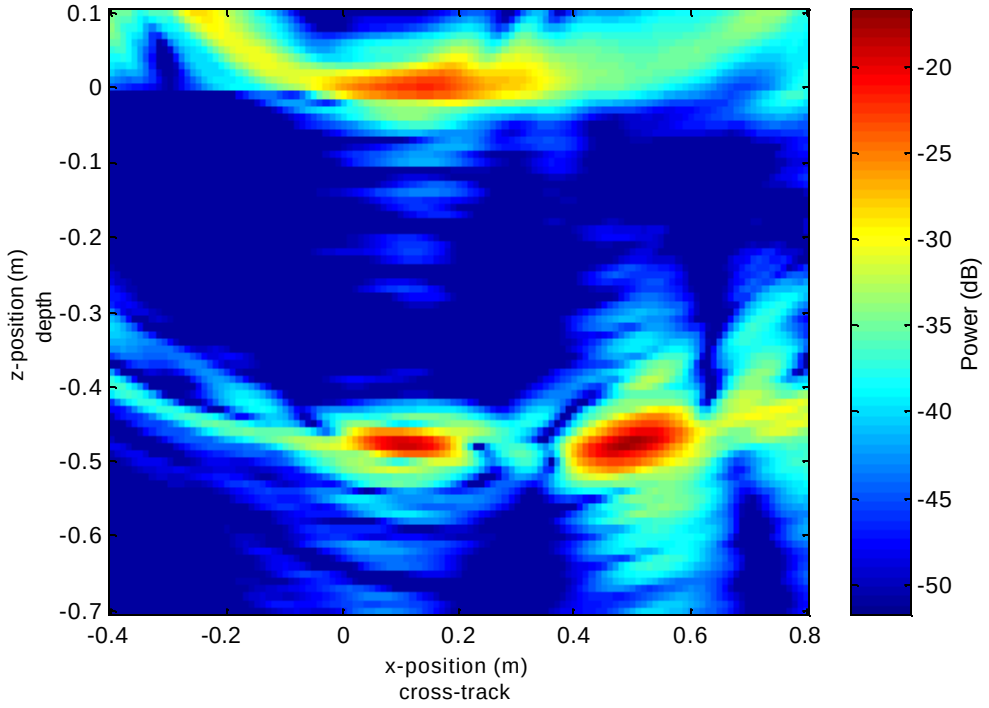


*Figure 5-38: SAR processed image of two simulated targets that are 0.4 m apart.*

The final result after SAR processing the measurements is shown in Figure 5-39. The SAR processing for this set of measurements was along the x-y plane rather than the x-z plane. This is more indicative of the type of processing that will be done in the final radar system where the x-y plane that is full of targets represents bedrock with different reflectivities. Here each target can be seen, but the smaller hollow targets are clearly just above the clutter/interference floor and are actually less bright than the side-lobes of the metal scatterers. The strongest side lobe is 4 dB above the weakest air-filled target, 7 dB below the weakest metal target, and 14 dB below the strongest metal target (maximum side-lobe energy was –49 dB). All targets were buried so that the top of the target was approximately 50 cm beneath the sand surface, but it was found that the peak energy fell at 48 cm beneath the sand surface and this was the depth used to create Figure 5-39. Since scattering measurements over this large of an aperture suffered from cancellation due to undulations in the antenna height and sand surface, only the sky shot was subtracted from the measurements.

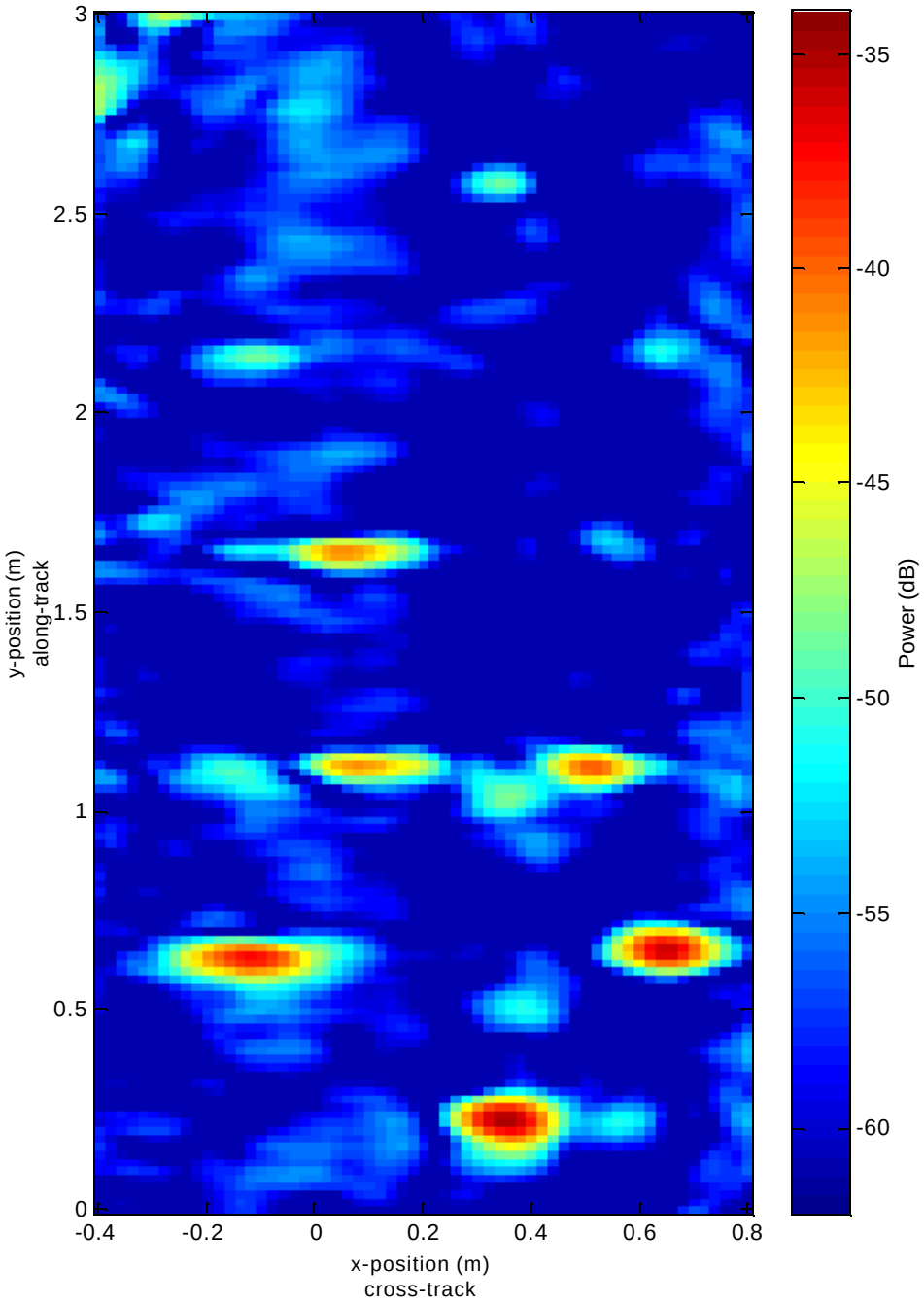


*Figure 5-39: SAR processed image of ten spherical targets.*

The results show that the along-track resolution is considerably better than that of the cross-track resolution. This is to be expected since both the receiver and transmitter move in the along-track direction, so the resolving capability will be at least double that of the cross-track resolving capability since only the receiver moves. Also, the targets are always broadside to the along-track synthetic aperture. In the cross-track direction, the array extends from 0.1 m to 0.75 m so only the targets right around 0.4 m are actually broadside to the synthetic aperture. The targets from –0.2 m to 0.2 m are off-broadside and the angular resolution is worse as can be seen in Figure 5-39. This result was proven for plane-waves in chapter 2.

The matched filter was successful at focusing the energy and identifying target locations. It also provided consistent estimates of the reflectivity from similar size and type targets (see Table 5-1). A more advanced filter would be able to provide better side-lobe performance. However, a better system model would probably be needed to really capitalize on a more advanced filter (since the ability to predict where side-lobes will occur is necessary for the filter to suppress them).

# CHAPTER 6: CONCLUSIONS AND FUTURE WORK

## 6.1 CONCLUSIONS

The remote sensing of ice sheets provides a better understanding of glaciology that can be used to predict future sea level rise. The particular information sought after in this work is the basal conditions of the ice sheet, which are expressed to the radar in terms of scattering characteristics. The proposed solution involves using multimode radar over a wide range of frequencies to efficiently determine scattering characteristics over a large area. A measurement model of this radar system and SAR processing algorithm based on the measurement model are described in chapter two and are used to produce the results throughout the remainder of the thesis.

A sensor geometry that minimized measurement time was determined as a function of frequency, maximum backscatter angle, and ice thickness. The optimal position was a weak function of frequency, although the size of the aperture required to resolve a target with beam forming is directly proportional to frequency (since it is the electrical length and not the physical length that determines resolution). The optimal position was very sensitive to the maximum backscatter angle, but in general the transmitter may be placed further out than the optimal position without significant increase in measurement time. Finally the optimal position tended to scale directly with ice thickness. This is not a problem since the ice thickness changes slowly from one location to the next.

Another method for improving traverse time using an along-track array towed behind the transmitter vehicle was considered. The use of an along-track array reduces the number of cross-track transects which in turn speeds up the measurement time.

In chapter four, a number of errors involved in SAR processing were analyzed using simulations. The matched filter is a fairly quick and scalable

algorithm, but it does not consider interference and its ability to estimate the reflectivity of a target that is adjacent to other targets is limited. The results for the maximum likelihood filter in a zero thermal noise environment are shown. This filter perfectly determines reflectivity because it projects each expected target response into a space orthogonal to all other targets and uses this to isolate the contribution from a single target. The accuracy of this approach is directly related to the signal to noise and interference ratio and the accuracy with which the model predicts target responses.

The radar will be using differential GPS to record position information. Differential GPS has position errors on the order of a fraction of a wavelength. Currently the exact nature of these errors is not known, but several scenarios are considered based on available information. It was found that one tenth of a wavelength accuracy was sufficient for achieving about 7-10 dB of dynamic range when a SAR aperture size given by results in chapter 3 was used. This dynamic range could be made slightly larger by increasing the SAR aperture size, but this leads to an increased measurement time.

The sensitivity of the SAR processor to dielectric errors was considered. It was found that the image stayed focused even with fairly significant errors, but the target positioning accuracy was directly affected (as was expected). The usefulness of the results are somewhat limited because the dielectric of ice is very well known and it is accurate knowledge of the transition from surface snow to solid ice that is less well known and may vary between regions. These results only considered a homogeneous ice sheet and the error was constant throughout the ice sheet.

The bedrock beneath the ice sheets exhibits a quasi-specular nature because it is electrically smooth. It was found that this quasi-specular nature effectively limits the SAR aperture that can be used to resolve a particular target when traditional SAR techniques are applied.

The sandbox laboratory was used to test a scaled model of the system. Several calibration measurements were taken to supply the system model with the

parameters necessary to predict the response from targets buried in the sand. Two poster tubes were effectively resolved using the SAR processing algorithm. One tube was metal covered and presented a large dielectric contrast between the sand and the target. The other tube was air-filled and presented a much smaller contrast. The respective estimated reflectivities replicated this difference.

The final sandbox measurement involved ten spherical targets with varying diameters, some metal covered and some air-filled. The results showed that the reflectivities for similar targets were very close to the same, except for the set of four metal covered targets with diameter 12.5 cm which had reflectivities ranging from –38 dB to –42 dB. The SAR processor was also able to accurately resolve each of the targets to within a few centimeters.

## 6.2 FUTURE WORK

The SAR processor and much of the results given in this thesis rely on an imperfect system model. Therefore, to improve the results in general, the system model needs to more accurately describe the expected response. The firn layer, basal ice and bedrock scattering properties need to be properly modeled. The firn layer can be represented in the model as discrete layered media and analyzed using propagation matrices. The electrical characteristics of the discrete layers can be found from the numerous cores taken from the Greenland and Antarctica ice sheets. The conversion from core data and application of propagation matrices has already been done and is presented in [27], but needs to be incorporated into the complete system model. The basal ice and bedrock scattering characteristics can be determined from borehole measurements and from radar measurements made on the ice sheet. The model should take into account inclusions in the basal ice, various types of water layers and cavities, and till characteristics.

The improved system model will also provide additional support in the data inversion process that maps measured data into geophysical parameters. Techniques for creating this mapping need to be investigated. Also, more advanced filters should

be implemented that determine basal reflectivity, such as iterative filters that minimize the mean squared error (e.g. Kalman filter). The iterative nature is important in that it simultaneously estimates the parameters of the underlying random processes and filters the data based on the estimates.

Finally, a number of practical considerations need to be addressed so that the sensor geometries and antenna array configurations can be determined. The results from chapter three can be used to adaptively modify the sensor geometry based the frequency band and *in situ* measurements of bedrock scattering and ice thickness.

The statistical nature of the position errors needs to be estimated. If the nature of the errors is independent of the region, then this can be done locally, otherwise, the field experiment in Greenland needs to address this issue. Knowledge of these errors will greatly help in predicting the performance of the SAR processor and which frequencies may produce optimal results.

We need to compare multiple ice cores made in the firn to find a range of potential dielectric profiles and see how the variance between these profiles affects the SAR processing (i.e. if we assume one profile for the firn, how are the results affected if the actual firn does not match this profile).

# SYMBOLS

### Mathematical Operations

$^H$ The Hermitian (or complex) transpose.

$\bar{\cdot}$ The complex conjugate of a scalar.

$\|\cdot\|_2$ The 2-norm (i.e. $\|v\|_2^2 = v^H v$).

$\langle \cdot, \cdot \rangle$ The Euclidean inner product of two vectors (i.e. $\langle v, w \rangle = v^H w$)

### Greek Characters

$a$ The cone of forward scattered energy ($\pm b$ from the specular ray).

$b$ The off-specular or forward scatter angle (equal to $2r$ in the monostatic case).

$b_x$ Angular resolution in the cross-track plane.

$d$ The angle between the broadside of a linear array and the direction of arrival.

$d_1$ An instance of $d$. In some cases, it refers specifically to the incident angle corresponding to the reflection from the end of the swath closest to the transmitter.

$d_2$ An instance of $d$. In some cases, it refers specifically to the incident angle corresponding to the reflection from the end of the swath furthest from the transmitter.

$e_r$ Relative permeability.

$e_{air}$ The real part of the relative permeability of air (assumed to be unity).

$e_{medium}$ The real part of the relative permeability of the medium in question.

$e_{sand}$ The real part of the relative permeability of sand from our GPR lab sandbox.

$f$ The scattering angle from the bedrock (not necessarily equal to the incident angle because we are considering diffuse or incoherent scattering and not just coherent scattering). This angle is measured from the normal direction of the boundary just as the incident and reflected angle are.

$g$ Arbitrary phase of a signal.

$h_{\mathrm{Re}\,ff}$ Receive antenna efficiency.

$h_{Teff}$ Transmit antenna efficiency.

$l$ The wavelength in the medium of interest.

$l_{\min}$ The minimum wavelength as determined by SAR processing requirements.

$m_x$ The n-by-1 vector of the means of the observations.

$m_{x_i}$ The $i^{th}$ element of $m_x$.

$q$ The incident angle onto the bedrock, which is equal to the reflected angle for the coherent/specular scattering.

$q_C$ The critical angle of a dielectric half-space.

$q_i$ The incident angle a dielectric half-space.

$q_t$ The transmitted angle through a dielectric half space.

$r$ The back-scatter angle measured with respect to the surface normal.

$s$ Standard deviation of position error.

$s_{bs}$ Transmit antenna efficiency.

$s_r$ Range resolution.

$s_x$ Cross-track resolution.

$\Sigma_n$ The m-by-m noise cross-correlation matrix.

$t$ Time delay between the responses from difference targets.

$w$ Angular frequency.

$\Psi_m$ Relative phase delay between the reference antenna element of the linear array and the m$^{th}$ element.

$\hat{a}$ Unit vector (e.g. $\hat{a}_{y'}$ or $\hat{a}_z$).

**Alphanumeric Characters**

$A$ Arbitrary amplitude of a signal.

$\vec{A}$ Antenna array position vector ( $A_x$, $A_y$, and $A_z$ are the components).

$A_R$ Effective area of receive antenna.

$A_{y'}$ Displacement along the y-axis from the antenna to the refraction point.

$B$ Total bandwidth of transmitter signal.

$B_{IF}$ Intermediate frequency (IF) bandwidth.

$B_d$ Bedrock surface subtended by a beam (as in beam-steering).

$B'_d$ Bedrock surface subtended by a beam (as in beam-steering).

$c$ Speed of light in a vacuum.

$d$ Spacing of the elements in a linear array.

$d_a$ Maximum dimension of an antenna for use in far-zone calculations.

D Depth of the bedrock (i.e. thickness of ice sheet).

$D_T$ Directivity of transmit antenna.

$d_{\max}$ Longest (in terms of delay) path length in a system.

$dt$ Sample spacing in the time-domain.

$dx$ Spatial sample spacing along the x-axis.

$dy$ Spatial sample spacing along the y-axis.

$f$ The m-by-1 filter vector (also frequency).

$f_c$ Center frequency.

$f_i$ The $i^{th}$ component of $f$.

$f_{\max}$ Maximum frequency as determined by SAR processing requirements.

$G$ The m-by-n matrix of expected target responses.

$G_R$ Gain of the receive antenna.

$G_T$ Gain of the transmit antenna.

$g_i$ The $i^{th}$ m-by-1 column of $G$.

$H_T$ Transmitter response.

$H_R$ Receiver response.

$k$ The wavenumber of a medium ($k_x$, $k_y$, and $k_z$ are the components).

L Equivalent free-space path length of the longest delay through the radar system and target scenery.

M Number of elements in a linear equally spaced array.

$n$ The m-by-1 vector of complex measurement noise.

$n_{ice}$ Index of refraction of solid ice (approximately 1.78).

$n_1$ Index of refraction of upper medium in a dielectric half-space.

$n_2$ Index of refraction of lower medium in a dielectric half-space.

$N_t$ The number of samples in the time-domain.

$N_x$ The number of samples in the space-domain along the x-axis.

$N_y$ The number of samples in the space-domain along the y-axis.

$P_R$ Received power.

$P_T$ Transmitted power.

$R$ Size of the receive cross-track synthetic aperture (also the minimum receive aperture that meets the desired cross-track resolution and swath width). Also the spacing from reference point to reference point for the Friss transmission formula.

$R_1$ Size of the SAR aperture required to resolve just the near point of the swath (near meaning the nearest point to the transmitter).

$R_1'$ Distance from the center of the swath to the point furthest away such that the receiver can still detect energy from the edge of the swath on the transmitter side.

$R_2$ Size of the SAR aperture required to resolve just the far point of the swath (far meaning the furthest point from the transmitter).

$R_2'$ Distance from the center of the swath to the point furthest away such that the receiver can still detect energy from the edge of the swath on the receiver side.

$R_M$ Minimum distance that the receiver must move to detect returns from both edges of the illuminated swath.

$R_M'$ Minimum distance that the receiver must move to detect returns from both edges of the illuminated swath.

$R_{Max}$ Maximum distance that the receiver can travel while still seeing returns from at least one point on the illuminated swath.

$R_R$ Target to receiver path length.

$R_{R1}$ Target to receiver path length (in medium 1).

$R_{R2}$ Target to receiver path length (in medium 2).

$R_T$ Transmitter to target path length.

$R_{T1}$ Transmitter to target path length (in medium 1).

$R_{T2}$ Transmitter to target path length (in medium 2).

$R_X$ Maximum distance that the receiver must move to detect returns from both edges of the illuminated swath.

Rx Receiver.

$\vec{S}$ Target position vector ($S_x$, $S_y$, and $S_z$ are the components).

$s$ The vector of n-by-1 complex target weights.

$\hat{s}$ The estimated vector of n-by-1 complex target weights.

$s_i$ The $i^{th}$ component of $s$.

$\hat{s}_i$ The $i^{th}$ component of $\hat{s}$.

$s_m(t)$ Signal received by the $m^{th}$ antenna element.

$S_1$ Position of a target placed at the edge of the swath closest to the transmitter.

$S_2$ Position of a target placed at the edge of the swath furthest from the transmitter.

$S_k$ The $k^{th}$ element of $\overline{S}$.

$S_{y'}$ Displacement along the y-axis from the refraction point to the target.

$t$ Time.

T Position of the transmitter relative to the midpoint of the swath.

$T_R$ Sweep time of network analyzer.

Tx Transmitter.

$v$ Velocity of electromagnetic waves in the medium of interest.

$x$ The vector of m-by-1 complex measurements.

x Cartesian coordinate.

$x_a$ Maximum dimension of an antenna aperture along the x-axis.

y Cartesian coordinate.

$y_a$ Maximum dimension of an antenna aperture along the y-axis.

z Cartesian coordinate.

# REFERENCES


[1] Douglas, Bruce C., Michael S. Kearney, and Stephen P. Leatherman, *Sea Level Rise: History and Consequences*, International Geophysics Series Vol. 75, Academic Press, San Diego, 2001.

[2] Douglas, Bruce C., and W. Richard Peltier, "The puzzle of global sea-level rise," Physics Today, pp. 35-40, March 2002.

[3] IPCC, *Climate Change 2001: The Scientific Basis*, IPCC, Geneva, Switzerland, 2001.

[4] Waggoner, Paul E., *Climate Changes and U.S. Water Resources*, John Wiley and Sons, New York, 1990.

[5] Rignot, Eric and Robert H. Thomas, "Mass Balance of Polar Ice Sheets," *Science*, vol 297, pp. 1502-1506, 30 August 2002.

[6] Terence J. Hughes, *Ice Sheets*, Oxford University Press, New York, 1998.

[7] Nesje, Atle and Svein Olaf Dahl, *Glaciers and Environmental Change*, pp 48, Oxford University Press, New York, 2000.

[8] NASA Ocean and Ice Branch, http://neptune.gsfc.nasa.gov/moceansice.html, Chester J. Koblinsky, March 2003.

[9] NASA Earth Science Enterprise, http://www.earth.nasa.gov/visio ns/researchstrat/Research_Strategy.htm, "Understanding earth system change NASA's Earth science enterprise research strategy for 2000-2010", NASA Earth Systems Science Research Strategy, October 2001.

[10] Van der Veen, Cornelis J., *Fundamentals of Glacier Dynamics*, A. A. Balkema, Rotterdam, Netherlands, 1999.

[11] Krabill, William B., Waleed Abdalati, Earl Frederick, Serdar Manizade, Chreston Martin, John G. Sonntag, Robert N. Swift, Robert H. Thomas, W. Wright, J. Yungel, "Greenland ice sheet: high elevation balance and peripheral thinning," *Science*, vol 289, no 5478**,** pp. 428-430**,** 21 July 2000**.**

[12] Kanagaratnam, Pannir, Silvaprasad Gogineni, Niels Gundestrup, and Lars Larsen, "High-resolution radar mapping of internal layers at the North Greenland Ice Core Project", Journal of Geophysical Research, vol 106, no. D24, pp. 33799-33811, Dec 27, 2001.

[13] Gogineni, Silvaprasad, Dilip Tammana, David Braaten, Carl Leuschen, Torry Akins, Justin Legarsky, Pannir Kanagaratnam, Jim Stiles, Chris T. Allen, and Kenneth C. Jezek, "Coherent radar ice thickness measurement over the Greenland ice sheet", Journal of Geophysical Research, vol 106, no. D24, pp. 33761-33772, Dec 27, 2001.

[14] Bamber, Jonathan L., Russell L. Layberry and Silvaprasad Gogineni, "A new ice thickness and bed data set for the Greenland ice sheet, 1. Measurement, data reduction, and errors", Journal of Geophysical Research, vol 106, no. D24, pp. 33773-33780, Dec 27, 2001.

[15] Arendt, Anthony A., Keith A. Echelmeyer, William D. Harrison, Craig S. Lingle, and Virginia B. Valentine, "Rapid wastage of Alaska glaciers and their contribution to rising sea level," *Science*, vol 297, pp. 382-386**,** 19 July 2002**.**

[16] National Geographic, Antarctica Map-Insert, February 2002.

[17] Gogineni, Silvaprasad, "A mobile sensor web for polar ice sheet measurements," NSF Proposal, October 2001.

[18] Englehardt, Hermann and Barclay Kamb, "Basal hydraulic system of a West Antarctica ice stream: constraints from borehole observations," *Journal of Glaciology*, vol 43, no 144, pp 207-229, 1998.

[19] Allen, Chris T., M. Gandhi, Silvaprasad Gogineni, and Kenneth C. Jezek, "Feasibility study for mapping the polar ice bottom topography using interferometric synthetic-aperture radar techniques," RSL Technical Report 11680-1, 1997.

[20] Gogineni, Silvaprasad, Teong S. Chuah, Chris T. Allen, Kenneth C. Jezek, Richard K. Moore, "An improved coherent radar depth sounder," *Journal of Glaciology*, vol 44, no 148, pp 659-669, 1998.

[21] Fisher, E., G.A. McMechan, M.R. Gorman, A. Paul R. Cooper, C.L.V. Aiken, M.E. Ander, and M.A. Zumberge, "Determination of bedrock topology beneath the Greenland ice sheet by three-dimensional imaging of radar sounding data," *Journal of Geophysical Research*, vol 94, no B3, pp 2874-2882, Mar 10, 1989.

[22] Jacobel, Robert W., and S.M. Hodges, "Radar internal layers from the Greenland summit," *Geophysics Research Letters*, vol 22, no 5, pp 587-590, 1995.

[23] Musil, George J., and Chris M.S. Doake, "Imaging subglacial topography by a synthetic aperture radar technique," *Annals of Glaciology*, vol. 9, pp 170-175, 1987.

[24] Walford, M.E.R., and M.F.L. Harper, "The detailed study of glacier beds using radio-echo techniques," *Geophysical Journal of the Royal Astronomical Society*, vol 67, no 3, pp 487-514, 1981.

[25] Ulaby, Fawwaz T., Richard K. Moore, and Adrian K. Fung, *Microwave remote sensing: active and passive*, Volume II, Artech House, Norwood, MA, 1986.

[26] Leuschen, Carl, *Ground-Penetrating Radar Imaging Algorithms*, M.S. Thesis, University of Kansas, 1997.

[27] Pingenot, James D., "Ice EM Model", IEEE Undergraduate Student Paper Contest, IEEE Region Five, Jan 2003.

[28] Marz, Justin, Personal Communication, March 17, 2003.

[29] Goodman, Nathan, *SAR and MTI processing of sparse satellite clusters*, Ph.D. Dissertation, University of Kansas, 2002.

[30] Higgins, Richard J., *Digital Signal Processing in VLSI*, Prentice Hall, Englewood Cliffs, New Jersey, 1990.

[31] Johnson, Don H., Dan E. Dudgeon, *Array Signal Processing: Concepts and Techniques*, Prentice Hall, Englewood Cliffs, New Jersey, 1993.

[32] Brandwood, D. H., "A Complex Gradient Operator and its Application in Adaptive Array Theory," Proceedings IEE, Special Issue on Adaptive Arrays, vol. 130, Part F, pp. 11-17, February 1983.

[33] Van Trees, Harry L., *Optimum Array Processing: Part IV of Detection, Estimation, and Modulation Theory*, John Wiley and Sons Inc, New York, 2002.

[34] Munem, M. A., D. J. Foulis, *Calculus with Analytic Geometry Second Edition*, Worth Publishers Inc, New York, New York, 1984.

# APPENDIX A: MAXIMUM LIKELIHOOD FILTER

The maximum likelihood filter chooses the $s$ that maximizes the likelihood function based on the observations [31]. The likelihood function is given in (A.1). By using only the conditioned probability of $x|s_k$, it does not presume knowledge about the distribution of the unknown variable, $s_k$. The analysis is the same for each component in the vector $s$ so only the analysis for one component is shown. We start by observing $x$ and then choose the $s_k$ that causes the $\Pr\{x|s_k\}$ to be maximized.

$$L(s_k) = f_{x|s_k}(x|s_k) \tag{A.1}$$

To do this, we take the derivative of the likelihood function with respect to $s_k$ and set the result to zero to find the stationary points of the function. To verify that the stationary point that we find is a maximum, we take the second derivative with respect to $s_k$ and check to see if the result is negative.

The likelihood function for additive Gaussian noise is the probability density function (pdf) of the multivariate Gaussian variable $x|s_k$.

$$f_{x|s_k}(x|s) = \left(2p\left|\Sigma_{x|s_k}\right|\right)^{-n/2} \exp\left(-\frac{1}{2}\left(x - m_{x|s_k}\right)^H \Sigma_{x|s_k}^{-1}\left(x - m_{x|s_k}\right)\right) \tag{A.2}$$

Here H is the Hermitian or complex conjugate transpose. Because the pdf is nonnegative and nonzero for all values and the logarithmic function is strictly increasing, we can take the logarithm of the likelihood function without affecting its stationary points. Since the Gaussian pdf is an exponential form, it is easier to maximize the log likelihood function, $L_{\ln}(s_k)$, than the likelihood function itself.

$$L_{\ln}(s_k) = \ln(L(s_k)) = -\frac{n}{2}\ln\left(2p\left|\Sigma_{x|s_k}\right|\right) + \left(-\frac{1}{2}\left(x - m_{x|s_k}\right)^H \Sigma_{x|s_k}^{-1}\left(\overline{X} - m_{x|s_k}\right)\right) \tag{A.3}$$

Before taking the derivative we need to determine which values depend on $s$. The covariance matrix $\Sigma_{x|s_k}$ is equal to the noise covariance matrix $\Sigma_n$ because $s$ and $G$ are not random.

$$\Sigma_{x|s_k}(i,j) = E\left\{\left(s_k G_i + n_i - E\left(s_k G_i + n_i\right)\right)^H \left(s_k G_j + n_j - E\left(s_k G_j + n_j\right)\right)\right\} \tag{A.4}$$

$$\Sigma_{x|s_k}(i,j) = E\left\{\left(s_k G_i + n_i - s_k G_i - m_{n_i}\right)^H \left(s_k G_j + n_j - s_k G_i - m_{n_i}\right)\right\} \tag{A.5}$$

$$\Sigma_{x|s_k}(i,j) = E\left\{\left(n_i - m_{ni}\right)^H \left(n_j - m_{n_i}\right)\right\} = \Sigma_n(i,j) \tag{A.6}$$

The mean $m_{x|s_k}$ is equal to

$$m_{x|s_k} = E\{(Gs+n)\} = Gs + m_n \tag{A.7}$$

(A.3) then becomes

$$L_{\ln}(s_k) = -\frac{n}{2}\ln\left(2p\left|\Sigma_n\right|\right) + \left(-\frac{1}{2}(x - Gs - m_n)^H \Sigma_n^{-1}(x - Gs - m_n)\right) \tag{A.8}$$

$L(s_k)$ is a real-valued function of two variables – the real and imaginary parts of $s_k$ which we will denote $s_{kI}$ and $s_{kQ}$. Therefore, a more precise way of representing the likelihood function is to write $L(s_{kI}, s_{kQ})$. Any stationary point of this function will require that the derivatives with respect to the real and imaginary parts be zero. One brute-force technique is to take the derivative with respect to the real part and then the imaginary part of $s_k$ and set each to zero. This is tedious because every complex number in the equation must be broken into its real and imaginary parts.

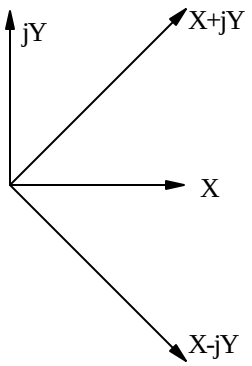


*Figure A-1: A complex variable and its conjugate are linearly independent combinations of the real and imaginary parts of the variable.*

A quicker method involves taking the derivative with respect to $s_k$ only. The following procedure for taking the derivative of a real-valued function $L(s_{kI}, s_{kQ})$ with respect to the complex scalar $s_k$, when $s_k^*$ is also present in the function, is discussed in [32, 33]. Since $s_k$ and $s_k^*$ are independent in the linear algebra sense, we can write $s_{kI}$ and $s_{kQ}$ in terms of $s_k$ and $s_k^*$ as (see Figure A-1 for illustration):

$$s_{kI} = g(s_k, s_k^*) = \frac{1}{2}(s_k + s_k^*) \tag{A.9}$$

and

$$s_{kQ} = g'(s_k, s_k^*) = \frac{1}{2}(s_k - s_k^*) \tag{A.10}$$

This means that each of the arguments to $L(s_{kI}, s_{kQ})$ can be written using the functions $g$ and $g'$:

$$L(s_{kI}, s_{kQ}) = L(g(s_k, s_k^*), g'(s_k, s_k^*)) \tag{A.11}$$

Using the chain rule for functions of two variables, we can determine the derivative with respect to $s_k$ as

$$\frac{\partial L\left(s_{kI}, s_{kQ}\right)}{s_k} = \frac{\partial L\left(g\left(s_k, s_k^*\right), g'\left(s_k, s_k^*\right)\right)}{\partial s_{kI}} \frac{\partial s_{kI}}{\partial s_k} + \frac{\partial L\left(g\left(s_k, s_k^*\right), g'\left(s_k, s_k^*\right)\right)}{\partial s_{kQ}} \frac{\partial s_{kQ}}{\partial s_k} \tag{A.12}$$

The partial derivatives with respect to $s_k$ are:

$$\frac{\partial s_{kI}}{\partial s_k} = \frac{\partial g\left(s_k, s_k^*\right)}{\partial s_k} = \frac{1}{2} \tag{A.13}$$

and

$$\frac{\partial s_{kQ}}{\partial s_k} = \frac{\partial g\left(s_k, s_k^*\right)}{\partial s_k} = \frac{-j}{2} \tag{A.14}$$

Plugging these into equation (A.12), we get

$$\frac{\partial L\left(s_{kI}, s_{kQ}\right)}{s_k} = \frac{\partial L\left(g\left(s_k, s_k^*\right), g'\left(s_k, s_k^*\right)\right)}{\partial s_{kI}} \frac{1}{2} + \frac{\partial L\left(g\left(s_k, s_k^*\right), g'\left(s_k, s_k^*\right)\right)}{\partial s_{kQ}} \frac{-j}{2} \tag{A.15}$$

$$\frac{\partial L\left(s_{kI}, s_{kQ}\right)}{\partial s_k} = \frac{1}{2}\left(\frac{\partial L\left(s_{kI}, s_{kQ}\right)}{\partial s_{kI}} - j\frac{\partial L\left(s_{kI}, s_{kQ}\right)}{\partial s_{kQ}}\right) \tag{A.16}$$

When taken with respect to the conjugate of $s_k^*$, the result following similar steps is:

$$\frac{\partial L\left(s_k, s_k^*\right)}{\partial s_k^*} = \frac{1}{2}\left(\frac{\partial L\left(s_{kI}, s_{kQ}\right)}{\partial s_{kI}} + j\frac{\partial L\left(s_{kI}, s_{kQ}\right)}{\partial s_{kQ}}\right) \tag{A.17}$$

A complex-valued function of $s_k$ and $s_k^*$ requires that the derivatives with respect to $s_k$ and $s_k^*$ be zero to form a stationary point. However, since the likelihood function is in Hermitian quadratic form, its output is a scalar that is equal to its complex conjugate and hence real. Therefore the function is a real-valued function that takes a complex number as its input. Because the function is real-valued, its derivative with respect to a real quantity ($s_{kI}$ and $s_{kQ}$) must also be real-valued. This can be seen by noting the derivatives in (A.18) and (A.19) are only functions of the real-valued quantities. The numerator must be real since the

likelihood function is real-valued. The denominator, $\Delta s_{kI}$, is also real and therefore the derivative must be real.

$$\frac{\partial L(s_{kI}, s_{kQ})}{\partial s_{kI}} = \lim_{\Delta s_{kI} \to 0} \frac{L(s_{kI} + \Delta s_{kI}, s_{kQ}) - L(s_{kI}, s_{kQ})}{\Delta s_{kI}} \tag{A.18}$$

$$\frac{\partial L(s_{kI}, s_{kQ})}{\partial s_{kQ}} = \lim_{\Delta s_{kQ} \to 0} \frac{L(s_{kI}, s_{kQ} + \Delta s_{kQ}) - L(s_{kI}, s_{kQ})}{\Delta s_{kQ}} \tag{A.19}$$

Observe that if equation (A.16) is zero, then the real and imaginary parts of the equation must be zero. Since the real and imaginary parts of (A.16) are $\frac{\partial L(s_{kI}, s_{kQ})}{\partial s_{kI}}$ and $\frac{\partial L(s_{kI}, s_{kQ})}{\partial s_{kQ}}$ respectively, they are therefore both zero which satisfies the constraint that the function is stationary with respect to both $s_{kI}$ and $s_{kQ}$. The implication of this is that taking the derivative with respect to $s_k$ *or* $s_k^*$ and setting the result to zero will provide the stationary point that is needed when the function is real-valued. Since both $s_k$ and $s_k^*$ work, we should choose the one that is easiest to work with. This is $s_k^*$ for the function that is dealt with here because we will be left with $s_k$ (and not have to take the conjugate at the end).

To show that the critical points are a maximum or minimum (depending on the optimization) we need to take the second partial derivatives. The following theorem can be used to determine the critical points [34]:

> *Let* $(a,b)$ *be an interior point of the domain of a function* $f$ *, and suppose that the first and second partial derivatives of* $f$ *exist and are continuous on some circular disk with* $(a,b)$ *as its center and contained in the domain of* $f$ *. Assume that* $(a,b)$ *is a critical point of f, so that* $f_1(a,b) = f_2(a,b) = 0$. *Let*
>
> $$\Delta = \begin{vmatrix} f_{11}(a,b) & f_{12}(a,b) \\ f_{12}(a,b) & f_{22}(a,b) \end{vmatrix} = f_{11}(a,b) f_{22}(a,b) - [f_{12}(a,b)]^2$$

*Then*

(i) If $\Delta > 0$ and $f_{11}(a,b) < 0$, then $f$ has a relative maximum at $(a,b)$

(ii) If $\Delta > 0$ and $f_{11}(a,b) > 0$, then $f$ has a relative maximum at $(a,b)$

(iii) If $\Delta < 0$, then $f$ has a saddle point at $(a,b)$

(iv) If $\Delta = 0$, then the test is inconclusive, and other methods must be used.

To use the theorem we will need to find the second partial derivatives with respect to the real and imaginary components. Once again, for the equation that needs to be optimized, we can find these partial derivatives by taking the derivatives with respect to the complex variables using the chain rule as given in (A.12). The second partial derivative with respect to $s_k^*$ is:

$$\frac{\partial^2 L(s_{kI}, s_{kQ})}{\partial s_k^{*2}} = \frac{1}{2}\left\{\begin{array}{l} \dfrac{\partial}{\partial s_{kI}}\left[\dfrac{1}{2}\left(\dfrac{\partial L(s_{kI}, s_{kQ})}{\partial s_{kI}} + j\dfrac{\partial L(s_{kI}, s_{kQ})}{\partial s_{kQ}}\right)\right] \\ \quad + j\dfrac{\partial}{\partial s_{kQ}}\left[\dfrac{1}{2}\left(\dfrac{\partial L(s_{kI}, s_{kQ})}{\partial s_{kI}} + j\dfrac{\partial L(s_{kI}, s_{kQ})}{\partial s_{kQ}}\right)\right] \end{array}\right\} \tag{A.20}$$

$$\frac{\partial^2 L(S_{kI}, S_{kQ})}{\partial S_k^{*2}} = \frac{1}{4}\left[\frac{\partial^2 L(S_{kI}, S_{kQ})}{\partial S_{kI}^2} + j2\frac{\partial^2 L(S_{kI}, S_{kQ})}{\partial S_{kI}\partial S_{kQ}} - \frac{\partial^2 L(S_{kI}, S_{kQ})}{\partial S_{kQ}^2}\right] \tag{A.21}$$

$$\frac{\partial^2 L(S_{kI}, S_{kQ})}{\partial S_k^{*2}} = \frac{1}{4}\left[\frac{\partial^2 L(S_{kI}, S_{kQ})}{\partial S_{kI}^2} - \frac{\partial^2 L(S_{kI}, S_{kQ})}{\partial S_{kQ}^2}\right] + \frac{j}{2}\frac{\partial^2 L(S_{kI}, S_{kQ})}{\partial S_{kI}\partial S_{kQ}} \tag{A.22}$$

The equation considered here has $\dfrac{\partial^2 L(S_{kI}, S_{kQ})}{\partial S_k^{*2}} = 0$, which leads to the following two conditions:

$$\frac{\partial^2 L(S_{kI}, S_{kQ})}{\partial S_{kI}^2} = \frac{\partial^2 L(S_{kI}, S_{kQ})}{\partial S_{kQ}^2} \tag{A.23}$$

$$\frac{\partial^2 L(S_{kI}, S_{kQ})}{\partial S_{kI}\partial S_{kQ}} = 0 \tag{A.24}$$

Now taking the second partial derivative with respect to $S_k$:

$$\frac{\partial^2 L(S_{kI}, S_{kQ})}{\partial S_k \partial S_k^*} = \frac{1}{2}\left\{\begin{array}{l} \dfrac{\partial}{\partial S_{kI}}\left[\dfrac{1}{2}\left(\dfrac{\partial L(S_{kI}, S_{kQ})}{\partial S_{kI}} + j\dfrac{\partial L(S_{kI}, S_{kQ})}{\partial S_{kQ}}\right)\right] \\ \quad - j\dfrac{\partial}{\partial S_{kQ}}\left[\dfrac{1}{2}\left(\dfrac{\partial L(S_{kI}, S_{kQ})}{\partial S_{kI}} + j\dfrac{\partial L(S_{kI}, S_{kQ})}{\partial S_{kQ}}\right)\right] \end{array}\right\} \tag{A.25}$$

$$\frac{\partial^2 L(S_{kI}, S_{kQ})}{\partial S_k \partial S_k^*} = \frac{1}{4}\left[\frac{\partial^2 L(S_{kI}, S_{kQ})}{\partial S_{kI}^2} + \frac{\partial^2 L(S_{kI}, S_{kQ})}{\partial S_{kQ}^2}\right] \tag{A.26}$$

Using the result from (A.23) we have:

$$\frac{\partial^2 L(S_{kI}, S_{kQ})}{\partial S_k \partial S_k^*} = \frac{1}{2}\left[\frac{\partial^2 L(S_{kI}, S_{kQ})}{\partial S_{kI}^2}\right] \tag{A.27}$$

Therefore, the second partial derivative with respect to $S_k$ and $S_k^*$ is equal to the second partial derivative with respect to $S_{kI}$ which is the final value needed to apply theorem one. Calculating $\Delta$:

$$\Delta = \begin{vmatrix} \dfrac{\partial^2 L(S_{kI}, S_{kQ})}{\partial S_{kI}^2} & \dfrac{\partial^2 L(S_{kI}, S_{kQ})}{\partial S_{kI}\partial S_{kQ}} \\ \dfrac{\partial^2 L(S_{kI}, S_{kQ})}{\partial S_{kI}\partial S_{kQ}} & \dfrac{\partial^2 L(S_{kI}, S_{kQ})}{\partial S_{kQ}^2} \end{vmatrix} = \left[\frac{\partial^2 L(S_{kI}, S_{kQ})}{\partial S_{kI}^2}\right]^2 \tag{A.28}$$

This quantity must always be positive which means that the critical point is either a maximum or a minimum. To determine which of these two the critical point is, we find $\frac{\partial^2 L(S_{kI}, S_{kQ})}{\partial S_k \partial S_k^*} = \frac{1}{2}\left[\frac{\partial^2 L(S_{kI}, S_{kQ})}{\partial S_{kI}^2}\right]$. If $\frac{\partial^2 L(S_{kI}, S_{kQ})}{\partial S_k \partial S_k^*}$ is negative, then the critical point is a maximum. Otherwise it is a minimum.

Taking the derivative of (A.8) with respect to $S_k^*$ and setting the result to zero gives

$$0 = \frac{1}{2} G_k{}^H \Sigma_n^{-1} (x - Gs - m_n) = \overline{\overline{G_k}}^H \Sigma_{\overline{N}}^{-1} \overline{X} - \overline{\overline{G_k}}^H \Sigma_{\overline{N}}^{-1} \overline{\overline{G}}\,\overline{S} - \overline{\overline{G_k}}^H \Sigma_{\overline{N}}^{-1} m_{\overline{N}} \tag{A.29}$$

where $G_k$ is an n-by-m zero matrix except for the k$^{th}$ row which is equal to the k$^{th}$ row of $G$. (A.29) holds for $k \in 1..m$; combining these equations we then solve for $s$. Since this is the $s$ that maximizes the log likelihood function, it is our estimate, which we call $\hat{s}$.

$$\left(G_k{}^H \Sigma_n^{-1} G\right) s = G_k{}^H \Sigma_n^{-1} (x - m_n) \;\forall\; k \in 1..m \tag{A.30}$$

$$\hat{s} = \left(G^H \Sigma_n^{-1} G\right)^{-1} G^H \Sigma_n^{-1} (x - m_n) \tag{A.31}$$

To verify that this is a maximum, we need to take the second derivative of (A.8) with respect to $s_k$ as shown in (A.32). The matrix $G$ is constant so it can be brought inside the expectation operator.

$$\frac{\partial^2}{\partial s_k^* \partial s_k} L_{\ln}(s_k) = -\frac{1}{2} G^H \Sigma_n^{-1} G = -\frac{1}{2} G^H E\{nn^H\} G = -\frac{1}{2} E\{G^H nn^H G\} \tag{A.32}$$

Observe that $G^H nn^H G = G^H n \left(G^H n\right)^H$, therefore the result is the square of the 2-norm of $G^H n$ which forces the quantity to be greater than or equal to zero. Since the noise variance is non-zero and $G$ should have at least one non-zero value, the quantity must be strictly greater than zero. The negative sign in (A.32) means that the second derivative is negative and therefore the first derivative describes a maximum.

If the multivariate noise has zero mean and is composed of independent identically distributed variables (i.i.d.), then $\Sigma_n$ is a diagonal matrix and can be written as $\Sigma_n = s_n^2 \mathrm{I}$ and its inverse is $\Sigma_n^{-1} = \left(s_n^2\right)^{-1} \mathrm{I}$. $s_n^2$ is the variance from a single random noise variable. Using this simplification, we can rewrite (A.31) as

$$\hat{s} = \left(G^H s_n^2 \mathrm{I} G\right)^{-1} G^H s_n^2 \mathrm{I} x = \left(G^H G\right)^{-1} G^H x = G^{\sim 1} x = G^{\sim 1} (Gs + n) \tag{A.33}$$

where $G^{\sim 1} = \left(G^H G\right)^{-1} G^H$ is the pseudo-inverse and guarantees that the filter coefficients for the target $s_k$ are orthogonal[13] to each of the other target's reference functions since $G^{\sim 1} G = \left(G^H G\right)^{-1} G^H G$ is an m-by-m identity matrix – off-diagonal elements are zero which implies that the filter coefficients for each target are orthogonal to all other targets. Note that this result does not depend on our knowledge of the noise variance.

When considering a single target, $s$ becomes a scalar and $G$ becomes an n-by-1 vector.

$$\hat{s} = \left(G^H s_n^2 \mathrm{I} G\right)^{-1} G^H s_n^2 \mathrm{I} x = \left(G^H G\right)^{-1} G^H x = \frac{G^H x}{\|G\|_2^2} = \frac{G^H (Gs + n)}{\|G\|_2^2} \tag{A.34}$$

where $\|\cdot\|_2$ is the 2-norm. This is the traditional matched filter result since $G^H$ is the complex conjugate of the reference function for $s$. The maximum likelihood filter equals the matched filter when only one target is assumed to be present. The signal to noise ratio of the single target estimate is

$$SNR = \frac{E\left\{\left|\frac{G^H}{|G|^2} sG\right|^2\right\}}{E\left\{\left|\frac{G^H}{|G|^2} n\right|^2\right\}} = \frac{E\left\{\left|G^H sG\right|^2\right\}}{E\left\{\left|G^H n\right|^2\right\}} = \frac{|s|^2 \|G\|_2^4}{E\left\{\left(G^H n\right)^H G^H n\right\}} = \frac{|s|^2 \|G\|_2^4}{E\left\{n^H G G^H n\right\}} \tag{A.35}$$

$n^H G$ represents $n_1^* G_1 + n_2^* G_2 + \cdots + n_n^* G_n$ and $G^H n$ represents $G_1^* n_1 + G_2^* n_2 + \cdots + G_n^* n_n$. Since the cross terms will be zero (noise samples have zero mean and are independent), the expectation $E\left\{n^H G G^H n\right\}$ will be $n_1^* G_1 G_1^* n_1 + n_2^* G_2 G_2^* n_2 + \cdots + n_n^* G_n G_n^* n_n$ or $|G_1|^2 |n_1|^2 + |G_2|^2 |n_2|^2 + \cdots + |G_n|^2 |n_n|^2$. We

[13] Orthogonal with respect to the inner product defined as $\langle u, v \rangle = u^H v$

also know that the noise samples are identically distributed and therefore the expected value of the denominator finally becomes $s_n^2 \|G\|_2^2$. Substituting this back into (A.35):

$$SNR = \frac{|s|^2 \|G\|_2^4}{s_n^2 \|G\|_2^2} = \frac{|s|^2 \|G\|_2^2}{s_n^2} \tag{A.36}$$

The signal to noise ratio of a single observation is given by:

$$SNR = \frac{E\{|sG|^2\}}{E\{|n|^2\}} = \frac{|s|^2 |G|^2}{s_n^2} \tag{A.37}$$

Therefore the signal to noise ratio increases as the magnitude of the reference function $G$ increases.